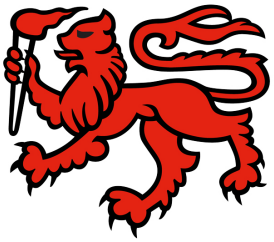

UNIVERSITY*of*
TASMANIA

School of Natural Sciences

Observational Probes of Helium Ignition in Low–Mass Stars

Ellen M. Manning
Bachelor of Science with Honours

March 2019

Supervisor: Assoc. Prof. Andrew A. Cole
Co-Supervisor: Prof. Simon P. Ellingsen

Submitted in partial fulfilment of the requirements for the
Degree of Doctor of Philosophy in Astrophysics
University of Tasmania

Declaration

This thesis contains no material which has been accepted for the award of any other degree or diploma in any tertiary institution, and to the best of my knowledge and belief, contains no material previously published or written by another person, except where due reference is made in the text.

Signed: _____

Date: **17/03/2019**

Authority of Access

Signed: _____

Date: **17/03/2019**

Statement of Co–Authorship

The following people contributed to the publication of work undertaken as part of this thesis:

Candidate	Ellen Manning	University of Tasmania, School of Natural Sciences
Co–Author (Supervisor)	Andrew Cole	University of Tasmania, School of Natural Sciences

Chapter 2: *From K giants to G dwarfs: stellar lifetime effects on metallicity distributions derived from red giants*
Manning, E. M., & Cole, A. A. 2017, MNRAS, 471, 4194
Candidate (70%), Co–Author (30%)
Candidate was the primary author, while Co–Author conceived the study and produced the underlying model. Candidate performed analysis and took the lead in writing the manuscript. Feedback and some text were provided by Co–Author.

We the undersigned agree with the above stated "proportion of work undertaken" for the above published peer–reviewed manuscripts contributing to this thesis:

Signed: Candidate _____

Co–Author _____

Acknowledgements

"Science without religion is lame, religion without science is blind."
Albert Einstein

First and foremost, I am exceptionally grateful to my supervisor Andrew for the seemingly endless amounts of time and effort he has dedicated to helping me over the years. His extensive assistance in every aspect of my candidature was invaluable and greatly appreciated. I am also very grateful for the seemingly endless emotional (and sometimes financial) support from my friends and family over the past few years. Of special mention is obviously Ed, who has proved magnificent in easing the emotional burdens that come along with conducting research off–campus, and Aviva who was always around to provide much needed tea, and the occasional motivational nudge to get off Facebook. I will be forever indebted to both of you.

Thank you to Brendan for providing me with the initial (but invaluable) code for part of my analysis. Your contribution saved me weeks (possibly months) of angst. I would also like to thank the team at the University of Tasmania's High Performance Computer Cluster (maintained by the Tasmanian Partnership for Advanced Computing) for allowing me to utilise this invaluable resource. John Miezitis was always quick to answer the *many* questions I fired at him over the months. I am also extremely grateful to Jesse for helping with a seemingly tiny, but invaluable, step towards the very end.

More generally, the conversations with my department colleagues over Friday Morning Tea were an excellent aid to overcoming the latest "researcher's block". It was a resource I did not appreciate enough at the time. Thanks also to my selfless proof–readers (in alphabetical order) Andrew, Aviva, Brendan, Ed, and Gaby, who tortured themselves with my early thesis drafts.
Cheers!

I would like to dedicate this work to my Lord and Saviour, Jesus Christ.

Abstract

The later evolutionary stages of Solar–type stars are governed by nuclear reactions that successively convert helium into carbon and carbon into oxygen. The relative numbers of highly evolved, low–mass stars as a function of luminosity and temperature can be analysed as a way to gauge the conditions under which these elements are synthesised and the energy released in their reactions. The most extreme event in the life cycle of low–mass stars is the explosive ignition of helium under electron degenerate conditions. This "helium–flash" involves the complete rearrangement of the stellar structure in a turbulent and non–equilibrium process. Although the theoretical reasoning for the occurrence of this violent event is comprehensive, observational evidence is virtually non–existent because the effects on the surface properties are subtle, and it occurs on a significantly shorter timescale than surrounding stellar evolutionary stages. Due to this, the precise details of the helium–flash (HeF) remain unclear.

The physical conditions and processes occurring in low–mass stars during these advanced stages of their evolution are explored as part of this project. The initial aim is to test the predictions of red giant stellar evolution models by looking at the expected "death rate" of red giant branch (RGB) stars at the onset of core helium–burning by accounting for the lifetime and initial mass function calculations. Simulated population densities of red giants are created from PARSEC isochrones (Padova and Trieste Stellar Evolution Code) to calculate simple correction factors for over– and under–represented populations, depending on age and metallicity. These results have an immediate application of correcting spectroscopic samples, since the age– and metallicity–dependences of RGB lifetimes require careful modelling.

Comparing the simulated number of stars populating the RGB and horizontal branch (HB) allows for the calculation of approximate evolutionary rates through the HeF phase for different stellar ages and metallicities. These data are combined with evolution tracks generated by MESA (Modules for Experiments in Stellar

Astrophysics) to improve estimates. The clear trend in evolutionary rates is that longer times are associated with higher metallicities, and with the exception of younger stars, evolution rates do not vary significantly with age. These results are in agreement with previous studies where applicable, however this project covers a wider range of ages and metallicities than previously explored in this area. The calculated locations of the HeF in colour–magnitude coordinates derived here, could aid future observational searches for this elusive population of stars.

The second stage of this project investigates whether post–HeF stars, before they settle on the HB, can be identified in current stellar variability surveys, testing the predictions from the first stage. Data from the Optical Gravitational Lensing Experiment (OGLE) are used here, since it is the most complete catalogue of variable stars currently available. Using Lomb–Scargle period analysis, 182 variables in the Small Magellanic Cloud (SMC) are identified with changing periods (from a sample size of 2,383), including 20 of which are likely to be post–HeF candidates based on their negative rate of change in periodicity and their location in relation to the HB. The two methods for determining change in periodicity used here are tested against previous detections in similar star types, with excellent agreement. These candidates warrant follow–up observations in order to determine the cause of their changes in periodicity, and possibly give the first observational insight into a star's evolution immediately following a helium–flash.

Contents

List of Figures

List of Tables

Chapter 1

Introduction

The basic theory of stellar structure and evolution is a mature field, and our understanding of main sequence (MS) stars is highly developed. Conversely, red giants have historically been more difficult to understand both because of their more complicated structure, and their relatively rapid lifetimes. Nowadays, red giants are observationally important because they are the brightest tracers of Population II stars and are highly overrepresented in magnitude–limited surveys.

Select red giants are the focus of this research due to a particularly violent and rapid event which occurs towards the end of their red giant branch (RGB) evolution, namely the core helium–flash (HeF[1]). This HeF was discovered by Schwarzschild & Härm (1962) in calculated core models of Population II red giants, who described the event as "a sliding down of the star along the red giant branch". Their study built on the foundational work of Mestel (1952) who described explosive ignition under electron degenerate conditions, and Hoyle & Schwarzschild (1955) who showed that red giants will ignite helium in this way.

Despite these theoretical discoveries being made decades ago, the existence of the HeF is yet to be observationally proven. The aim of this research is to examine the implications of models based on current understanding of RGB evolution (pre–core–flash), and apply these results to identify possible post–core–flash candidates in current observational surveys. To do this, a thorough review of red giant evolution is required.

[1]Here, HeF refers to core helium–flashes only, rather than flashes occurring in the helium–shell during the asymptotic giant branch stage (AGB).

1.1 Red Giant Evolution

While the elemental abundance ratios in a star have a small impact on some stellar evolutionary stages (see Section 1.3.1), the mass is by far the most important factor governing the star's life. Stellar size, luminosity, temperature, which fusion reactions will occur, the evolution rates in different stages, and how the star will eventually die, are all dictated by its mass (see Hansen et al., 2004, for full discussion). The evolution of low–mass stars (zero–age main sequence; ZAMS mass 0.8–2 $M_{\odot}$) differs greatly from higher mass ones once they cease core hydrogen–burning and leave the main sequence (MS; Bethe & Critchfield, 1938). They slowly ascend the red giant branch (RGB), burning hydrogen in a shell surrounding the ever–growing helium core (Sandage & Schwarzschild, 1952). Unlike stars of higher mass, the helium–cores of low–mass stars become electron degenerate prior to them reaching sufficient temperature to ignite the cores at the tip of the red giant branch (TRGB; see Section 1.2 for a detailed discussion). Due to these conditions, the ignition of helium in the core is violent and releases a large amount of energy in a very short period of time. Although the ascent of the RGB can take a low–mass star roughly a billion years, their descent after helium ignition follows a similar evolution path back down, but only takes 1–2 Myr (for example Despain, 1981; Sweigart, 1994; Brown et al., 2001; Silva Aguirre et al., 2008; Paxton et al., 2011; Bildsten et al., 2012). Following this, the star begins to burn helium quiescently in its core, marking the onset of the horizontal branch stage HB which lasts approximately 70 Myr.

Core helium–burning stars are positioned on the Hertzsprung—Russell diagram (HRD) not only as a result of their chemical composition and age, but also the amount of mass lost, as this directly affects the luminosity and colour of the star. If the post–RGB mass is less than about 0.8 $M_{\odot}$, the stars occupy the horizontal branch (HB), fusing helium into carbon via the triple-α (3α) process, but if the mass exceeds 0.8 $M_{\odot}$, they form a red clump (RC) at cooler temperatures. The 3α process is a series of nuclear reactions involving three ^{4}He nuclei (α particles) fusing into ^{12}C, via the formation of ^{8}Be, at temperatures exceeding 10^{8} K (see Fowler, 1986, and Section 1.1.2, for discussions).

Red giant evolution is dictated by the timescale for core growth due to the production of helium from the surrounding hydrogen–burning shell. However, most of a red giant star's interior is in a state of turbulent convection (see Section 1.1.3 below), meaning that the stellar radius and other important properties cannot

be predicted from first principles. Since convection is notoriously difficult to model, red giant evolution is challenging to represent accurately, especially when considering all the other microscopic and macroscopic stellar processes talking place.

There are many factors to consider when mapping stellar structure and evolution: the initial conditions of the star, and complex processes that take place, along with the timescales on which they occur. The conditions in stellar interiors (very high temperatures and pressures) are vastly different to those which can be created in a laboratory. In addition, the effects of many physical processes are subtle and difficult to detect from surface observations. Therefore, modelling certain specific rapid stages in stellar evolution can be difficult and often inaccurate, due to the departures from equilibrium over the relevant timescales.

1.1.1 Stellar Timescales

There are many different processes occurring in stellar interiors, influencing the overall structure and physical properties of the star. The timescales of these processes are generally quite different, and it is this disparity that (for the most part) allows predictions of stellar structure and evolution. When a particular process is considered, other processes occurring over much larger timescales may be safely ignored in the calculations, while processes that occur more rapidly are assumed to be at equilibrium. It is when these assumptions break down that stellar models become uncertain.

Dynamical Timescale

The only thing stopping a star from either exploding due to the energy released by nuclear fusion reactions, or collapsing in on itself due to its immense mass, is the fact that the outward radiation pressure perfectly balances the gravitational force inwards. The dynamical timescale (t_{dyn}) represents the time period of a star's expansion or contraction if this balance was suddenly disrupted by a new source or sink of pressure support. It is expressed as the ratio of the stellar radius to its escape velocity (v_{esc}). The escape velocity is defined as the velocity required of an object travelling away from the surface of a certain mass to overcome the effects of gravity exerted by that mass:

$$v_{esc} = \sqrt{\frac{2GM}{R}}. \tag{1.1}$$

Thus, the dynamical timescale becomes

$$t_{dyn} = \sqrt{\frac{R^3}{2GM}}. \tag{1.2}$$

In the case of the Sun, $t_{dyn} \approx 1000$ s, while for a red giant of solar mass $t_{dyn} \approx 10^6$ s due to the increased radius.

Kelvin–Helmholtz Timescale

The Kelvin–Helmholtz (KH), or thermal timescale, is defined as the time required for a star to radiate all its thermal energy if nuclear fusion suddenly ceased. The ratio of the nuclear thermal energy of a star to its luminosity provides an estimate of how rapidly a star contracts before nuclear fusion starts (that is, the PMS lifetime). However, the thermal energy must be roughly equal to the gravitational potential energy (as explained above). Thus, the thermal timescale can be expressed in terms of the gravitational potential energy:

$$t_{KH} \approx \frac{GM^2}{RL}. \tag{1.3}$$

In the case of our Sun, this is roughly $3{\times}10^7$ years.

Since the core and envelope are thermally distinct, the values for t_{KH} are quite different between them. In the case of a low–mass star at TRGB, the KH timescale is the thermal energy of the hydrogen envelope, divided by its luminosity ($t_{KH} \approx 10^4$ yr), while for a star in the RC, it is the thermal energy of the helium core divided by its luminosity ($t_{KH} \approx 10^6$ yr). At the TRGB there is no thermal component from the core as the helium is just about to ignite, but once it has ignited, the timescale is much longer and so the component from the envelope can be ignored following this.

Microscopic Collisions Timescale

Photons created in the core from nuclear fusion are scattered (absorbed and re-emitted) off electrons, atoms, ions, and other photons on their way to the surface. The mean free path (MFP) is the average distance they travel before being scattered and is defined as

$$\lambda_\gamma = \frac{1}{n\sigma}, \tag{1.4}$$

where n is the number of particles per unit volume, and σ is the cross–section of the particle. For a fully ionised hydrogen gas, the electron number density can be written as

$$\bar{n_e} \approx \frac{\bar{\rho_\odot}}{m_H} \approx 10^{24}\text{cm}^{-3}. \tag{1.5}$$

The dominant source of opacity for the deep interior of a solar–type star is Thomson scattering (also known as electron scattering; Thomson, 1906), where the cross–section becomes

$$\sigma_T = \frac{8\pi}{3}\left(\frac{e^2}{m_e c^2}\right)^2 \approx 6{\times}10^{-25}\text{cm}^2. \tag{1.6}$$

Combining these gives the MFP of a photon travelling through the Sun to be $\lambda_\gamma \approx 1$ cm, which gives the time between collisions of photons and electrons to be

$$t_{col} = t_{e\gamma} = \frac{\lambda_\gamma}{c} \approx 10^{-10}\text{s}. \tag{1.7}$$

H^- opacity (κ_{H^-}) becomes dominant in cool stars ($3,000 \lesssim T \lesssim 6,000$ K), especially in the envelope of a red giant. H^- opacity results from free–free and bound–free transitions, and requires both atomic hydrogen and free electrons. Once the effective temperature is too high, the H^- particles lose their extra electron. Thus, H^- opacity is strongly dependent on both temperature and the presence of iron–group elements (Bressan et al., 2013). Hansen et al. (2004) gives the following proportionality in terms of metallicity (Z), density and temperature:

$$\kappa_{H^-} \propto Z\rho^{1/2}T^9. \tag{1.8}$$

Since H^- opacity is more efficient at restricting radiative transfer than other sources (where it is in effect), the corresponding cross–section is much larger than in Equation 1.6, resulting in a much smaller collisional timescale in red giants than in a Solar–type star. The shorter MFP comes from the inability of outer layers to transmit all the flux produced by the hydrogen–burning shell of an RGB star, which contributes to the inflation of their convective envelopes to red giant dimensions (Renzini, 1984; Woosley et al., 1988; Renzini et al., 1992; Ritossa,

1996). Factors such as stellar helium abundance, metallicity, and mass loss also influence envelope inflation (see Arnett et al., 1989; Sugimoto & Fujimoto, 2000, and references therein).

The conclusions above are made assuming that interior stellar regions rapidly return to local thermal equilibrium after small disturbances. Unfortunately, this cannot be exactly true because the surrounding space is colder than the star so an internal temperature gradient will always exist. However, when considering certain stellar evolutionary stages, some timescales can simply be ignored.

Nuclear Timescale

The nuclear timescale (t_{nuc}) represents the time taken for a star to exhaust its fuel at the current rate of fusion. It is dependent on the amount of fuel available for nuclear fusion, which reactions are occurring, and the star's luminosity:

$$t_{nuc} = \frac{\epsilon m c^2}{L}, \tag{1.9}$$

where ϵ is the fraction of mass converted to energy in a particular nuclear reaction, and m is the mass of the fuel available. Using mass of hydrogen in the Sun's core and its luminosity gives $t_{nuc} \approx 7{\times}10^9 yr$, which is a fair indication of the Sun's MS lifetime. In general, nuclear timescales are significantly longer than other important timescales:

$$t_{nuc} \gg t_{KH} \gg t_{dyn} \gg t_{col} \tag{1.10}$$

As mentioned above, this vast difference between timescales allows predictions of stellar evolution.

However, during certain rapid stages of stellar evolution, the nuclear timescale becomes comparable to the thermal timescale, making modelling of these stages difficult. A prime example being stars undergoing a core helium–flash (see Section 1.2). Since red giants burning hydrogen in their shells are much brighter than they were during their MS lifetime, their nuclear timescales are proportionally shorter. To compound this, the energy produced from helium fusion is significantly less than that produced by burning hydrogen (roughly 10%), meaning that when red giants ignite helium, the nuclear timescales are orders of magnitude smaller.

1.1.2 Nuclear Reactions in Low–Mass Stars

The most important process occurring in a star's interior is the nuclear fusion of two protons (the pp–chains) which starts the process of converting hydrogen to helium (Clayton, 1968). This is the dominant energy–producing process in low–mass stars on the MS. The initiating reaction is the conversion of two hydrogen ions to deuterium:

$$^{1}\mathrm{H}^{+\,1}\mathrm{H} \longrightarrow {}^{2}\mathrm{H} + \mathrm{e}^{+} + \nu_{e} \ .$$

Unfortunately, this key reaction is very unlikely since it requires the two protons to overcome the Coulomb barrier and couple together, then almost immediately one of the protons must decay to a neutron, emitting a positron and an electron neutrino. This reaction proceeds so slowly that it dictates the rate of the entire pp–chain, effectively setting the nuclear timescale.

The reactions following this in the first pp–chain (PP–I) are:

$$^{2}\mathrm{H}^{+\,1}\mathrm{H} \longrightarrow {}^{3}\mathrm{He} + \gamma$$

and

$$^{3}\mathrm{He}^{+\,3}\mathrm{He} \longrightarrow {}^{4}\mathrm{He} + {}^{1}\mathrm{H}^{+\,1}\mathrm{H} \ .$$

The second and third pp–chains (denoted PP–II and PP–III) are alternate reaction chains, progressively becoming more important with higher temperatures, compared with the first pp–chain. The latter two reaction chains involve the creation of heavier elements (beryllium, lithium and boron) which then decay into helium. For a full discussion of these, see Hansen et al. (2004).

These three chains produce energy mainly in the form of photons, however neutrinos are also emitted in some reactions.

Helium–burning stars still produce energy from hydrogen fusion, but in the shell surrounding the core, where the pp–chains are replaced by the carbon–nitrogen–oxygen (CNO) cycle as the dominant source of energy in this region. The CNO cycle is also one that converts hydrogen to helium, but unlike the pp–chains, it is a catalytic conversion and is more prominent in hotter stars with masses above that of the Sun (Hansen et al., 2004). The 3α process produces heavier elements (namely carbon and oxygen) once a low–mass star reaches a helium–burning stage.

As previously mentioned, the triple–alpha process is a series of nuclear reactions involving the fusion of three α particles to form ^{12}C. Since no stable nucleus with eight nucleons exists, the conditions required for the 3α process to occur are quite precise. Sufficiently high temperatures (10^8 K) for two α particles to overcome their mutual Coulomb barrier and fuse together to form "di–α" (^{8}Be) are needed, alongside sufficiently high densities for the final α particle to be captured within the lifetime of the unstable ^{8}Be particle (10^{-16}s) and form ^{12}C (see Fowler, 1986, for a detailed discussion). However, if the temperature is only slightly higher than that required for the 3α process to occur, the ^{12}C produced can also capture an additional α particle to form ^{16}O. In this way, the following two reactions are in competition for the helium:

$$3\,{}^4\mathrm{He} \longrightarrow {}^{12}\mathrm{C} \text{ and } {}^{12}\mathrm{C}({}^4\mathrm{He},\gamma){}^{16}\mathrm{O}\ .$$

The balance between these two reactions is very sensitive to the excitation levels within both ^{12}C and ^{16}O (Hansen et al., 2004). Of the stars that are massive enough to ignite helium, more carbon is produced in lower mass stars, while oxygen production is favoured in higher mass stars.

In addition to determining which nuclear reactions occur, the conditions present in the stellar interior also dictate larger scale processes.

1.1.3 Convection

The most ubiquitous method of energy transport within a star is radiation. Photons diffuse from hotter regions (emission) to cooler regions (absorption), driven by the star tending towards local thermal equilibrium. The efficiency of radiative transfer is directly hindered by opacity, leading the way convection to take over in certain situations. Radiative and conductive heat transfer are mostly irrelevant for the stellar evolution stages being examined here. As such, only convection will be discussed in detail.

Convection is the transport of heat energy via the motion of fluid hotter or cooler than its environment and becomes a significant consideration in red giants and other cool stars. The mixing length theory (MLT; Böhm-Vitense, 1958) approximates local convective heat transport in stars by looking at a "parcel" of fluid moving either outwards in inwards in a star that is a slightly different temperature to its surroundings, a process commonly referred to as "hot bubbles rising". These parcels are created by instabilities in the fluid, with their motion

being determined by competing gravitational and buoyancy forces. When these forces balance the parcel will simply oscillate, but if a perturbation causes the parcel to rise and an unbalanced buoyancy force is acting in the same direction, the parcel will travel outwards in the star some characteristic distance l, after which it dissolve, depositing its heat energy. This distance is known as the mixing length.

The MLT provides a first order approximation of convection which is used in most cases. More accurate convective models requires incorporating complex three–dimensional, time–dependent fluid dynamics, which is why the MLT is so commonly used (see Pasetto et al., 2014, and references therein).

Further simplifications of the MLT are often made by using the Boussinesq approximations (Boussinesq, 1903). This set of assumptions includes ignoring effects such as magnetic fields, rotation, acoustic phenomena, and shocks; assuming that the temperatures and densities vary little between the parcel and its surroundings; and assuming that the parcel is of a size of order l^3, which is much smaller than any scale lengths associated with the star.

While it is assumed that the movement of this parcel through the star is roughly adiabatic (that is, no heat is exchanged with its surroundings and none is produced internally through nuclear burning), there is always the possibility that the parcel will in fact radiatively release some of its heat into its environment along the way. However, since $t_{KH} \gg t_{dyn}$ (Section 1.1.1) convection can be assumed to be adiabatic over short timescales. This adiabatic nature of the temperature gradient is what forces RGB stars to share a common structure, with very similar minimum effective temperatures regardless of mass (Hayashi et al., 1962).

When determining the onset of convection, an important quantity to consider is the logarithmic slope of the temperature over pressure (both of which will be functions of radius):

$$\nabla \equiv \frac{d \ln T}{d \ln P}. \tag{1.11}$$

The Schwarzschild criteria (Schwarzschild, 1906) for local convection is when the decrease in the parcel's temperature as it traverses distance l is less than the decrease in the temperature of the surroundings across the same radii:

$$\nabla > \nabla_{\mathrm{ad}}. \tag{1.12}$$

This convective instability criteria can also be expressed as a decrease in entropy

moving outwards in the star (Cox & Giuli, 1968). For a detailed derivation and discussion of these quantities, see Hansen et al. (2004), and references therein.

Convective processes take over from radiative ones as the dominant method of energy transport in a few situations. Firstly, when the opacity increases to such a level that radiative cooling of that region is greatly inhibited. Since the opacity increases with decreasing temperature this case generally only occurs in cooler stars, or the outer regions of stars. Opacity dictates the radiative energy transfer ($\nabla_{\rm rad}$) by definition. Increasing opacity inhibits radiative heat transfer and so the energy builds up in a region. If there is not sufficient convection ∇ needs to increase to keep the radiative flux at a point where it balances the inward pressure due to gravity.

Ionisation zones are also expected to be highly convective because ionisation causes ∇ (through its dependency on pressure) to exceed the temperature–pressure gradient present in the adiabatic case. Again, this is often limited to the outer regions of the stars since the core is generally fully ionised. However, ionisation zones occur at small radii in cooler stars where $\nabla_{\rm ad}$ is relatively small and opacities are high (Cox & Giuli, 1968).

Another cause of convection dominating energy transport is when the energy generation rate is very sensitive to temperature (for example the CNO cycle and 3α process), causing the flux to increase rapidly as the stellar radius tends to zero. In phases where the CNO cycle dominates, convection enforces a very different structure on the star based on the thermodynamics of the stellar material and can influence the course of future evolutionary phases by homogenising the composition of the star within convective regions.

Convection plays a significant role in setting the structure of an RGB star (recall that the hydrogen envelope is largely convective; Section 1.1.1). Convection is not well modelled in one–dimension, and coupled with the relatively rapid progression through red giant evolution, there are far more uncertainties in the modelling of RGB stars than MS stars (see Section 1.3 for further discussion).

1.2 The Core Helium–Flash

The most violent event in the evolution of a low–mass star is when helium is ignited in its electron degenerate core. Because pressure does not depend on temperature when degenerate, the energy produced through the 3α reactions (Section 1.1.2) is not used for expansion but rather further heating of the region,

leading to the reactions progressing increasingly faster, causing thermonuclear runaway. This thermally unstable HeF ends the star's ascension of the RGB and occurs when the core reaches a mass of $\sim$0.48 $M_\odot$ and a temperature of 10^8 K, as first explored by Hoyle & Schwarzschild (1955); Schwarzschild & Härm (1962, see also Salaris et al., 2002; Serenelli & Weiss, 2005; Mocák et al., 2009; Paxton et al., 2011). Although violent, the HeF is believed to be a mainly non–hydrodynamic event (Deupree, 1996; Dearborn et al., 2006; Mocák et al., 2008; Paxton et al., 2011), however there has been some debate on this subject (Mocák et al., 2009, 2010). For more details, see Section 1.3.

The degenerate conditions mean that energy loss in the core occurs primarily in the form of neutrino emission (Thomas, 1967; Demarque & Mengel, 1971; Despain, 1981), since the opacity is sufficiently high to strongly inhibit radiative energy loss.

The neutrinos are produced through weak interaction processes occurring at the high temperatures and pressures towards the end of the RGB phase, and they escape the star without interacting much with their environment. Neutrino cooling is so efficient that at the time of the initial flash, an inverted temperature gradient is present in the core (Thomas, 1967; Despain, 1981). As a result, helium–ignition occurs at a mass coordinate of about halfway through the core, releasing an enormous amount of energy ($L_{HeF} \approx 10^{9.3}$ $L_\odot$, as much as some galaxies; Shen & Bildsten, 2009). At the instant of helium–ignition, the helium luminosity (L_{He}) is $\sim$10 $L_\odot$ (Mocák et al., 2008), but much of this energy is absorbed by the core to lift the degeneracy and does not make it to the surface. This high local luminosity leads the helium–ignition region to become convective, all the way out to the base of the hydrogen–burning shell. Because of this, the energy is transported quickly to the non–degenerate regions, leading to expansion of the envelope. However, when the helium–core finally does expand, it causes an adiabatic temperature drop in the overlying hydrogen–burning shell, reducing the nuclear fusion rate (Bildsten et al., 2012). This energy loss in the red giant envelope triggers a rapid KH–contraction (see Section 1.1.1) at the TRGB, which in turn causes it to heat up. This marks the beginning of its journey to the HB.

The initial ignition of helium just prior to the TRGB is the first of several successive core helium–subflashes, that remove the degeneracy over $\sim$1–2 Myr during the core–flash phase (CFP; Thomas, 1967). Fewer subflashes are required the closer the initial HeF occurred to the centre (that is, stars with higher masses and helium abundances; Sweigart & Gross, 1978). These subsequent flashes re-

lease less nuclear energy than the main HeF (Kippenhahn et al., 2012) but increase entropy in the convective regions (Thomas, 1967). The process is said to be almost independent of both total mass and metallicity (for example, Thomas, 1967; Serenelli & Weiss, 2005; Bildsten et al., 2012, see also Chapter 3 for counter analysis). This process heats the core at approximately constant pressure until the star is converted into a stable object located on the RC or HB where it continues as a stable core helium–burning star for ∼70 Myr. Because of the extremely strong temperature dependence of the 3α process (Section 1.1.2), this core helium–burning is also convective.

During the onset of helium–ignition, reactions proceed very quickly, which requires models to implement timesteps on the order of seconds to hours (see Serenelli & Weiss, 2005; Mocák et al., 2008; Paxton et al., 2011). Evolution of a star from the TRGB through the CFP occurs near instantaneously, compared to the surrounding stages (RGB and RC/HB) which last on the order of $10^7 - 10^8$ yr (see analysis in Bildsten et al., 2012). Dramatic structural changes happen very quickly, while subtle changes last much longer.

The timescale of the CFP is dictated by the thermal diffusion of photons acting inwards towards the core centre between subflashes (Thomas, 1967; Serenelli & Weiss, 2005). During this time the outer envelope is very similar to stars on the RC, even though convective helium–burning only occurs for ∼10% of the CFP (Bildsten et al., 2012). The ∼2 Myr and ∼70 Myr durations of the CFP and RC respectively, imply that 1 in 35 stars near the RC will be undergoing or be between core helium–flashes.

Although the theoretical reasoning for the occurrence of the HeF is comprehensive, the precise details are unclear, as the event has never been observed. This is because of a number of reasons; the effects on the surface properties are subtle, the event occurs on much shorter timescales than that of the surrounding evolutionary stages, and the evolutionary path on the HRD overlaps with other stages such as the RGB, asymptotic giant branch (AGB), HB and RC. This is partly due to the hydrogen–shell burning occurring in all of these stages, hence presenting similar surface effects. Thus, accurate stellar evolution models are vital to capture conditions occurring within the stars over this phase (see Section 1.3).

1.2.1 Previous Work

Thus far, only one star has been identified as a possible CFP candidate: LS IV-14°116 (Miller Bertolami et al., 2011). However, Randall et al. (2015) argue that the atmospheric parameters derived from their observations, in particular the high surface gravity detected, is sufficient evidence that the star is in fact post–CFP, burning helium quiescently in the core. Rather, the authors suggest that LS IV-14°116 is part of the Galactic halo population. To make matters more interesting, a very recent study by Battich et al. (2018) has explained several attributes of the star using stellar models covering the CFP (discussed in detail below). Thus, the classification of this star remains controversial.

Despite this very limited sample, there have been no observational studies specifically searching for HeF candidates. As such, this project will represent a new approach to solving the uncertainties surrounding the evolutionary phases immediately before and after the HeF.

Variable Stars

Intrinsically varying stars can give us insight into interior structure and processes that otherwise might be unobservable. Pulsations are driven by some source of instability within the star, with the most common source being ionisation and recombination, which alternates between absorbing radiation and re–emitting it. This ionisation and recombination can be driven by a number of things (for example, gravity, pressure, magnetic fields), causing stars to oscillate in the fundamental mode, the first–overtone, both of these modes, and in the second–overtone. However, only the fundamental mode of oscillations has been expressed by a simple period–mean density relation:

$$P \propto \langle \rho \rangle^{-\frac{1}{2}}, \tag{1.13}$$

where P is the period, and $\langle \rho \rangle$ is the average stellar density. This relation and the proportionality constant were originally derived by Ritter (1879). From this, it can be surmised that the period will depend on the radius and luminosity of the star, both of which are changing rapidly during the CFP, compared with other variables in a similar location in the instability strip.

Driving and damping pulsations depends on the mechanical perturbations (travelling pressure waves), and how effectively heat is radiated away. Thus, period variability occurs on two different timescales - the period–mean density

relation (Equation 1.13), and the KH timescale (Equation 1.1.1). This pulsation period roughly corresponds to the dynamical timescale because the oscillations are caused by mechanical means rather than electromagnetic, which is many orders of magnitude shorter than thermal (KH) or nuclear timescales (for definitions, see Section 1.1.1). Due to these shorter timescales, we can assume that changes in chemical composition due to nuclear reactions are negligible.

Pulsating stars are often classified in terms of their excitation mechanisms. Partial ionisation of either hydrogen or helium drive pulsation through energy generation (ϵ–mechanism) or the transfer of energy (κ– and γ–mechanisms). The temperature and density profiles of the stellar interior dictate the relative importance of these mechanisms.

For pulsations to be excited by κ– or γ–mechanisms, a local region of the star must gain energy under compression and release it during expansion. This occurs when the stability coefficient is negative (also denoted by κ Rosseland, 1949; Cox, 1955). In regions of non–degenerate, fully ionised gas, Kramers' opacity law (named after H. Kramers, in 1923; Gray, 2005) can be observed:

$$\kappa_K \propto \rho T^{-3.5}. \tag{1.14}$$

Thus, with increasing density, the opacity tends to decrease as a result of increasing temperature. However, partial ionisation of hydrogen and helium cause a local reversal in the opacity relationship, now increasing with temperature. The increase in opacity under compression results in the energy being stored in the region, and released under expansion. This ability of stellar regions to gain heat under compression is called the γ–mechanism (see Cox, 1963; Cox et al., 1966). Thus, the κ– or γ–mechanisms act together, with increases in temperature increasing opacity and thus amplifying the κ–mechanism. Collectively, these are called the heat mechanism and drive pulsations in variable stars on the classical instability strip (Figure 1.1).

The so–called instability strip marks a region of the HRD where stellar pulsations are driven by helium ionisation. The second–helium ionisation drives Cepheids (Classical and Type II) and RR Lyrae stars (Smith, 2013), while the first helium–ionisation is responsible for driving pulsations in Mira–class variables. RR Lyrae and Type II Cepheids represent post–RGB, low–mass stars and as such form the basis for the analysis in Chapter 4.

Pressure increases in nuclear fusion regions causes local temperatures to in-

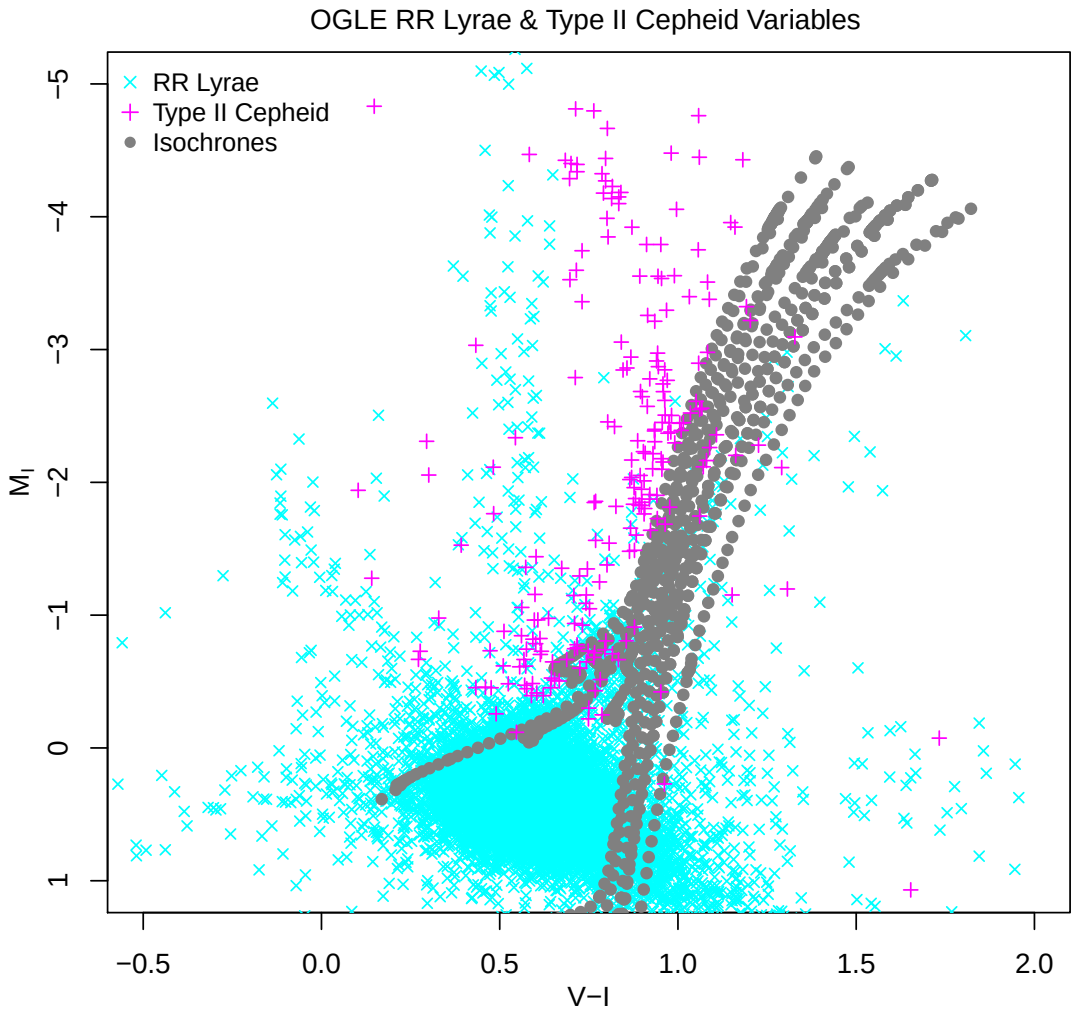

Figure 1.1: RR Lyrae (cyan) and Type II Cepheid (magenta) variables in the Small and Large Magellanic Clouds from the OGLE online catalogue (see Chapter 4). For reference, PARSEC isochrones (in grey) of simulated intermediate–age to old, low–metallicity stellar populations (see Chapter 2) are plotted alongside, showing the RGB, HB, and AGB phases. The observed magnitudes were converted to absolute magnitudes based on the distance modulus of 18.95 ± 0.07 (Graczyk et al., 2014) for the SMC, and a distance modulus of 18.49 for the LMC (Hoyt et al., 2018).

crease. This in turn leads to increases in the rate of energy generation in these regions, while the opposite occurs during expansion. Consequently, energy is lost and gained locally during expansion and compression. If the magnitude of these temperature and density oscillations are sufficiently large, the nuclear energy generation rate (ϵ) will fluctuate over time. This defines the ϵ–mechanism. In low–mass stars, generally temperature variations are on the order of 1 K in regions of $10^7 - 10^8$ K. Thus, for the most part, the ϵ–mechanism is more applicable in high–mass stars. However, Miller Bertolami et al. (2013) and Battich et al. (2018) have associated pre–extreme HB stars undergoing subflashes with pulsations excited by the ϵ–mechanism. This is discussed further below.

While there has been plenty of theoretical work and simulations based around the HeF, there have been no observational studies aiming to identify possible candidates. It was first noted by Catelan in 2005 that while evolving from the TRGB to the HB or RC, the star may cross the instability strip (Catelan, 2009). Thus, a star undergoing a HeF could possibly be identified as a variable star with large changes in its period. The idea was later theoretically expanded on by Silva Aguirre et al. (2008, 2010, detailed below). RR Lyrae and Type II Cepheids are old, low–mass stars that present a way to observationally probe this rare population because their periods and light curve shapes are highly sensitive to the internal structure of the star. Due to the large amounts of high–sensitivity photometric data freely available, an analysis of these variable stars forms part of this project (Chapter 4).

Silva Aguirre et al. (2008) presented the first theoretical effort to characterise stars in the late CFP as RR Lyrae variables with rapidly changing periods. Period change rates of $|\dot{\mathrm{P}}| \geq$ 0.1-0.15 d/Myr are considered relatively high (see Smith, 1995, for a review), but Lee (1991) identifies these cases as stars nearing the end of their HB phase. Silva Aguirre et al. (2008) used a grid of evolutionary tracks derived from Garching Stellar Evolution Code (GARSTEC Weiss & Schlattl, 2008), to simulate old, low–mass stars from the globular cluster M3 (NGC 5272). GARSTEC is capable of following a star's evolution through the CFP (see Weiss & Schlattl, 2008, and references therein). Silva Aguirre et al. (2008) calculated for every 60 HB stars in the simulation, one is undergoing its CFP. Of those identified as CFP stars, 22% are RR Lyrae stars with $\dot{\mathrm{P}}\approx$-0.3 d/Myr. The authors determined that these post–HeF RR Lyrae stars can be identified by relatively long periods and period changes mainly within $[-1, 0]$ d/Myr, with about 24% having an increasing period. These results can be used as selection criteria for

identifying possible HeF candidates in observational data.

There is already some evidence to suggest that using observations of variable stars is an effective way to identify short, violent stellar evolutionary stages. From photometric light curve observations, Uttenthaler et al. (2016) concluded that RU Vulpeculae (a semi–regular/Mira variable) is undergoing a helium–shell flash on the AGB, similar to the helium–core flash.

AGB stars burn hydrogen and helium in shells around the inert carbon/oxygen core. Unlike on the RGB, the helium–shell flashes in an AGB star do not occur in the electron degenerate carbon–oxygen core. Rather, the cause of this helium–shell flash, or thermal pulse (TP), is the quasi–periodic interruption of the hydrogen–burning shell by the ignition of helium–shell, which is a strongly temperature–dependent process (Schwarzschild & Härm, 1965).

The only source of fusion energy in an EAGB star comes from its thin hydrogen–shell burning. This is so inefficient that the helium–shell is not initially hot enough to trigger nuclear burning. Once the helium–shell reaches critical density and temperature, it ignites and marks the onset of the TP–AGB phase (Salaris & Cassisi, 2005). This is characterised by loops along the AGB on the HRD (for example, Schwarzschild & Härm, 1970; Gingold & Faulkner, 1974).

Uttenthaler et al. (2016) calculated changes in the period and amplitude of RU Vulpeculae, and concluded that the previous theory of it being an AGB star undergoing a helium–shell flash, was correct. The authors used the evolutionary model by Vassiliadis & Wood (1993) to closely match the observed pre–TP stage (quiescent hydrogen–burning) and subsequent decline in brightness of RU Vulpeculae, by inputting calculated values for its mass and metallicity. Due to the similarities between thermal pulses and helium–core flashes, this result is supportive of using similar methods to identify CFP candidates.

Asteroseismology

Asteroseismology has also previously been used to map the interiors of red giant non–radially pulsating stars (see Hekker, 2010, for a concise review). The frequency of the pulsations are studied, and from this the internal structure and conditions can be predicted. A brief review of previous studies into asteroseisomolgy of red giants is included here for reference, but original research into this area is beyond the scope of this project. The time–intensive nature of seismology observations means it is very unlikely to provide statistically significant sample

sizes of post–HeF stars.

The aim of asteroseismology is to accurately measure individual mode frequencies, which can then be used to test stellar models. Global oscillation parameters, such as the frequency of maximum oscillation power ($\nu_{\rm max}$) and average frequency separation between consecutive overtones of the oscillation mode ($\langle\Delta\nu\rangle$), along with $T_{\rm eff}$ can be used to derive values such as the stellar mass and radius (Hekker et al., 2011). The $\langle\Delta\nu\rangle$ values are directly related to the properties of the acoustic wave speed in the stellar interior, while the central frequency and amplitude of the oscillation envelope are related to the turbulent convection mechanisms that excite and damp the oscillations (Huber et al., 2010).

Stars with convective envelopes show solar–like oscillations sensitive to the same physical processes determining their interiors (for example, Brown & Gilliland, 1994). Hayashi et al. (1962) showed that since the interiors of red giants are almost entirely convective, they all have similar envelope structure. Thus, all red giants are presumed to oscillate non–radially (Dziembowski et al., 2001). Random oscillations with small amplitudes have been detected using both spectroscopic and photometric data in a few bright red giants of spectral types G and K (see De Ridder et al., 2009, and references therein).

Huber et al. (2010) used data from the first four months of the *Kepler* mission to study different aspects of solar-like oscillations in ∼800 red giants and reported that the $\Delta\nu$-$\nu_{\rm max}$ relation is significantly different when using red giants as opposed to MS stars. This is because the relation is principally sensitive to metallicity for MS stars and stellar masses for red giants. Since the red giants pulsate with larger amplitudes and longer periods than MS stars (Huber et al., 2010), they require less sensitive but longer (preferably continuous) sampling.

The rapid ($\lesssim 10^5$ yr; Thomas, 1967) KH contraction (see Section 1.1.1) of the red giant envelope after the initial HeF vastly improves the coupling of the p-modes (acoustics) to the g-modes (gravity waves) in the core, due to increased density and smaller pressure gradients (see Bedding et al., 2011; Mosser et al., 2011; Bildsten et al., 2012, and references therein). Coupling of vibrational systems occurs when there is energy exchanged between the different modes. Over the CFP, this coupling makes it possible to detect $l = 1$ mixed modes[2], and the star has a g-mode period spacing lower than that of helium–burning stars in the RC, but higher than the red giants at the same luminosity (see Figure 4 from

[2] l represents the number of nodal circles on the surface, formed by stationary points in the vibration cycle.

Bildsten et al., 2012, showing seismic properties of CFP stars). Plots of $\Delta\nu$ versus ΔP_g reveal the stars undergoing this CFP occupy an underpopulated region, facilitating their identification among the other observed red giants.

Space–based observations have enabled the detection of the angular degree $l = 1$ mixed modes, which have p-mode properties in the red giant envelope (where they are excited by convection and generally have $n_p \approx 10$ radial nodes), but only g-modes can penetrate the helium–core (see Hekker, 2010; Bildsten et al., 2012, and references therein). Internal buoyancy only supports the propagation of high order ($n_g > 100$) g-modes

Beck et al. (2011) identified modes around the $l = 1$ p-modes, nearly evenly spaced in period (at $\Delta P_{\rm obs}$), as characteristic of the interior core g-modes. This allowed Bedding et al. (2011) to identify first ascent RGB stars (those with degenerate helium–cores) and distinguish them from those with non–degenerate helium–cores (RC/HB stars).

The $l = 1$ mixed modes are more likely to be detected when the coupling through the outer evanescent region is strong. The coupling of $l = 2$ modes is not as strong as that for $l = 1$, as the outer turning point is closer to the core (Christensen-Dalsgaard, 2004). The results from Bildsten et al. (2012) show an additional inner evanescent zone appearing during subflashes. The $g-$mode cavity is split into two zones, each with their own distinct period spacing. If the inner cavity proves to be adequately coupled, these extra modes would cause oscillations in the observed period spacing.

As mentioned above, Battich et al. (2018) has recently modelled non–adiabatic, non–radial pulsations in $l = 1$ modes, excited by the ϵ–mechanism, in stars undergoing core helium–subflashes. The authors found these pulsations were only excited in very hot ($T_{\rm eff} \simeq$20,000 K) pre–HB stars. Extreme horizontal branch (EHB) stars are hotter than the blue–HB (which is hotter than the instability strip), and have been found in some globular clusters and the Galactic Disk (Heber, 2016; Battich et al., 2018). Battich et al. (2018) showed this population can be represented in a new instability domain in $\log T_{\rm eff} - \log g$ space, corresponding to low– to intermediate–order g–modes ($P \approx 200 - 2000$ s; see also Miller Bertolami et al., 2011). Naslim et al. (2010) had also previously argued that helium–rich, hot–subdwarf stars of spectral type B could undergoing their CFP, corresponding to this pre–EHB population. Battich et al. (2018) calculated that 2–3% of pre–EHB stars should be pulsating due to ϵ–mechanism.

Although there has been thorough theoretical prediction work done in this

area (for example Bedding et al., 2011; Mosser et al., 2011; Bildsten et al., 2012), as of yet, no HeF candidates have been identified. This work looks to identify evolutionary changes in the periods of radial pulsations, which may potentially provide an observational probe into the stellar interiors of CFP red giants. However, the inherent changes in the stellar radius of variable stars may also make relevant period changes difficult to isolate.

1.3 Modelling Red Giant Evolution

Energy generated in the central regions of a star has to make its way through the star to the surface before it can be observed. As a result, radiation, and therefore information, from the stellar interior is lost. Because of this, much of what is known about stellar processes and evolution comes from computational models. Modelling is relatively simple when the star is in local thermal equilibrium. Deviations from this equilibrium occur for a number of reasons, but the most common being when the star adjusts between core– and shell–burning, transitioning from one evolutionary stage to the next. This section aims to outline the most significant shortcomings of modern red giant stellar models, and is by no means a complete list.

While RGB features such as colours, slopes, TRGB magnitudes, and the RGB bump are quite well–represented in models, the complexity of their structures, along with the inherent turbulence of convection (which rivals radiative transport during this stage), makes their rapid evolution through the CFP quite difficult to replicate. The evolution of a star after the MS not only depends on the microscopic physics chosen for the model, but also on the mixing processes related to the efficiency of convective core overshoot, atomic diffusion and rotation. Unfortunately, there are difficulties in theoretically defining the efficiency of overshooting in stars transitioning between radiative and convective cores (see, for example Aparicio et al., 1990). The efficiency of interior mixing, in both the MS phase and in later phases, is also not well understood. The turn–off region of helium–burning stars and the RC depend strongly on the mixing efficiency after the MS.

A major part of modelling stellar evolution is to predict the correct location (temperature and slope) of the RGB. This information is used to determine stellar population ages, as well as provide a photometric estimate of their metallicity. The modelled temperature of RGB stars (for a given chemical composition) is pre-

dominantly affected by the following input physics: the treatment of inefficient convection, the atmospheric boundary conditions, the low–temperature opacities and the equation of state (EoS; for details, see Cassisi et al., 2011; Montalbán et al., 2001; VandenBerg et al., 2012). Due to the required calibration of extra mixing at the base of convective layers, the location of the RGB is directly influenced by the observed metal abundance of the Sun (see Richer et al., 2000; Bressan et al., 2013). Additionally, when models do not consider envelope overshoot, the RGB bump is predicted to be brighter than is actually observed in globular clusters (Di Cecco et al., 2010), the degree to which depends on the metallicity.

It is generally agreed that the evolution of a star in the CFP is a mainly hydrostatic event, with energy being transported from the flash site quiescently via convection, heat conduction and radiation (Deupree, 1996). However, three–dimensional simulations by Dearborn et al. (2006) suggest quasi–hydrostatic evolution during the HeF. Mocák et al. (2008) used two–dimensional axisymmetric, hydrodynamical simulations with detailed EoS and time dependent gravitational potential to cover roughly eight hours of stellar evolution through the initial HeF. The authors found no hydrodynamic events that diverged significantly from previous stellar evolution predictions. After the initial flash and resulting structure adjustment, a quasi–steady state ensued where there was only a slow increase in the temperature and nuclear energy production rate because convection crucially controlled the hydrostatic equilibrium. More recently, one–dimensional simulated evolutionary tracks by Paxton et al. (2011) also show that the event does not become dynamic, because the changes in entropy occur over much longer timescales than local t_{dyn} (see, for example Thomas, 1967; Serenelli & Weiss, 2005; Mocák et al., 2008).

Subsequent studies by Mocák et al. (2009, 2010) using one–, two– and three–dimensional simulations, suggest that the CFP may indeed be hydrodynamic or at least quasi–hydrodynamic. The simulations show convective overshoot occurring at both the inner and outer borders, which results in the convection zone growing on a dynamical timescale. Their findings suggest that the extent of the inner convection zone (powered by the helium–burning during the flash), predicted by the canonical stellar evolution theory, is not correct. The authors also propose that following the initial HeF, no helium–core subflashes will occur (contrary to other current models), as convection will lift the electron degeneracy in less than one month. However, since most other sources agree that the HeF is a

quasi–hydrostatic event, this is the assumption made here.

Due to the lack of observations of the HeF and the CFP as a whole, the only data available is produced from stellar evolutionary models, based on the current understanding of evolutionary theory. There are still many areas that need improvement, for models to be reliable over this relatively rapid stage of evolution.

1.3.1 Metallicity and RGB Lifetimes

It is well known that the position of an RGB star on the colour–magnitude diagram (CMD) depends strongly on the metallicity of the star (for example, Da Costa & Armandroff, 1990), the RGB being much steeper at lower metallicities (see Figure 6 of Gallart et al., 2005). To complicate the matter further, there is also a slight dependence on stellar age through the mass dependence of the radius of a star on the Hayashi track (Hayashi et al., 1962; Cole et al., 2005). These relationships are shown in Figure 1.2 and explored in detail throughout Chapter 2. These degeneracies are difficult to analyse in observations of an individual RGB star or a small sample, but are still present, as an exploration of integrated light properties of large samples (often unresolved) makes clear.

To investigate this age–metallicity degeneracy, Worthey (1994) constructed integrated light models for intermediate–age and old stellar populations using evolutionary isochrones. The input parameters of the models included the metallicity range of $-2 < [\mathrm{Fe/H}] < 0.5$, and a single–burst age ranging over 1.5–17 Gyr. The author notes that while real galaxies have metal–poor stars that extend the HB, the models used assume the HB remains near the giant branch in a RC. Plots of $\log L$ vs $\log T_{\mathrm{eff}}$ show a number of interesting findings, namely that observed effects on integrated light colours and spectra due to different ages are comparable to metallicity effects at higher metallicities. Worthey (1994) shows three main results: 1) for stars older than 3 Gyr, the tip luminosity of the RGB is roughly constant; 2) isochrones shift cooler with increasing metallicity; and 3) the magnitude of the effect that stellar age has on RGB temperature is modulated by metallicity, where a higher metallicity means a lower impact. While this age–metallicity degeneracy is not readily broken analytically or through observations, simulated stellar evolution models may provide additional answers.

To complicate matters further, stellar metallicity also dictates certain evolutionary stage lifetimes. At low metallicity, the bound–free opacity present in

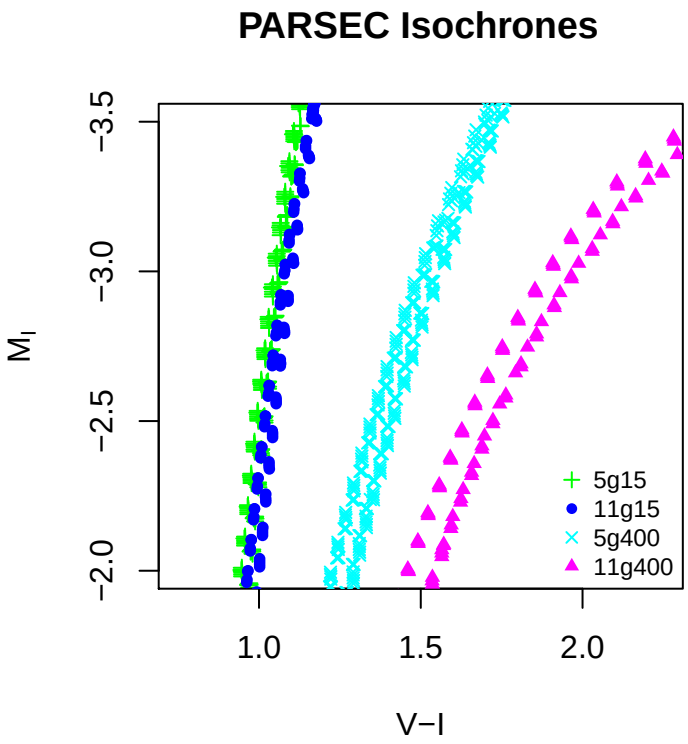

Figure 1.2: Comparison of four PARSEC isochrones, varying both age and metallicity, corresponding to four stellar population simulations (shown in Figure 2.2). Simulation 5g15 has stellar ages of 5–6 Gyr with a metallicity of Z=0.00015; simulation 11g15 is 11–12 Gyr with Z=0.00015; simulation 5g400 is 5–6 Gyr with Z=0.004, and simulation 11g400 is 11–12 Gyr with Z=0.004. See Chapter 2 for details.

low–mass MS stars is lower for a given mass, which increases its luminosity (Bowers & Deeming, 1984). In order to compensate for the lower opacity, the star is required to produce energy at faster rate to create the same pressure support as in a star with higher opacity, which results in the star having a shorter MS lifetime. However, once the star evolves into a red giant, this effect is partially countered due to the fact that the energy is now being produced via the CNO cycle in a hydrogen–shell surrounding the helium–core. A higher stellar metallicity increases the energy generation of the CNO cycle at fixed temperature and density, which would decrease the stellar lifetime, but this may be partially or completely countered by the changes in stellar structure due to the larger mean molecular weight and changed opacity (Clayton, 1968). It is because of these competing factors that simulations with accurate stellar evolutionary models are vital.

1.3.2 Mass Loss

The evolution of a low–mass star along the RGB ends with a HeF inside an electron–degenerate core. The mass of the helium–core at the TRGB determines both the luminosity at that point, and of the subsequent helium–burning phase (Bressan et al., 2013). For a given metallicity, model predictions of both the helium–core mass and the TRGB luminosity depend on the input physics of the model[3], the solar calibration, and the predictions of previous evolutionary phases. M_{HeF} is determined by the chemical composition and the assumed efficiency of core mixing processes during the hydrogen–burning phase, predominately convective overshoot and rotation (Bressan et al., 2013).

Stars experience significant mass loss while travelling along the RGB, with a total of approximately 34% of the star's initial mass lost post–MS (Kalirai et al., 2009). The temperature of the star when it reaches the HB depends greatly on the amount of mass lost (Rood, 1973; Dorman et al., 1993). However, currently this cannot be computed reliably. Reimers' law (equation below; Reimers, 1975) is most commonly used to determine mass loss rates along the RGB, but it is unable to explain empirical data (see, for example Dorman et al., 1993; Park & Lee, 1997; Piotto et al., 2007):

[3]For example, the efficiency of atomic diffusion, nuclear reactions, EoS, opacities, neutrino rates.

$$\dot{M} \propto \frac{L}{gR}, \tag{1.15}$$

where the proportionality constant is a free parameter.

Although other techniques exist that do agree with the data, they are not commonly used and they imply different age and metallicity dependencies and thus present integrated mass loss values that vary in each case (see Catelan, 2009, 2013, and references therein). The mass loss rate for RGB stars above solar metallicity is greatly dependent on metallicity (Kalirai et al., 2007; Catelan, 2009). However, Kalirai et al. (2009) showed that there was little to no dependence of mass loss rates on metallicity in stars with below solar metallicity.

In general however, evolution models encompass initial mass ranges to investigate, and so in most cases the mechanism behind any mass loss is irrelevant. All that is of importance is the stellar mass at the time of interest.

1.3.3 Convective Overshoot

Convection plays a pivotal role in cool stars, dictating their structures, but it is a complex, turbulent process that requires complex three–dimensional, time–dependent fluid dynamics to accurately model (a first–order approximation, the MLT, is described in Section 1.1.3). In addition, there are other processes associated with convection (overshoot and semiconvection) that are not well understood but could potentially play a large role in the structure and thus the evolution of such stars.

Convective–core overshoot is thought to occur when the opacity and temperature gradient are sufficiently high that convection dominates over radiative heat transfer. This is turbulent, unstable, and inefficient. Convective overshoot carries the material via convection beyond the turbulent region and into a stable outer layer. Sometimes referred to as turbulent entrainment, it is a hydrodynamic process, and occurs at both the inner and outer boundaries of the convection zone (red giant interiors are almost entirely convective; Hayashi et al., 1962). The effective temperature of a red giant is primarily controlled by its convective envelope opacity, which in turn depends heavily on the abundance of heavy elements in the star (for example, Hoyle & Schwarzschild, 1955; Bressan et al., 2013). As a function of the metallicity, the maximum ZAMS mass for a star to undergo a HeF (M_{HeF}) decreases drastically with overshoot (see Figure 1 in Bressan et al., 2015).

When carbon is produced in a helium–burning convective core, the free–free opacity increases, and with it the temperature gradient. Because of this, a discontinuity in the temperature gradient is formed at the outer radius of the convective core. Castellani et al. (1971) showed that carbon pollution causes the radiative layers to become unstable during this stage, and it is possible that the unstable region expands as the star evolves, known as local overshoot. Intuitively, the helium–core burning lifetime increases almost proportionally with core mass. When there is significant non–local overshoot, the discontinuity of the temperature gradient shifts to within the radiative stable regions, where the radiative gradient is much lower than the adiabatic one. Unlike in the case of local overshoot, pollution of layers above the convective core do not cause instability in the surrounding regions (Bressan et al., 1986).

Due to the layered structure, there can be a discontinuity in the chemical composition of the star that inhibits or promotes convection. When there is a sharp boundary between a helium–enriched and a hydrogen–rich layer, that boundary can actually induce convection even when the temperature gradient would not normally. This induced convection contributes to mixing the composition which smooths out the boundary layer, but does not transport a much (if any) flux. As such, it is radiatively stable, but is convective in terms of chemical transfer. This is known as semiconvection, and it contributes to mixing in central regions and further increases the size of the helium–exhausted core. If overshoot is large in a star, semiconvective instability does not occur.

Unlike the stellar overshoot in central regions, overshoot in the envelope has a negligible effect on stellar evolutionary properties. However, it may affect some observable properties (see Bressan et al., 2012), meaning that it may be possible to determine when the factors causing overshoot are occurring. The possibility of a significant overshoot region arising at the base of the convective envelope was first proposed by Alongi et al. (1991). This suggestion has lead to observations of the location of the RGB bump for low–mass stars (globular and old, open clusters; see Bressan et al., 2012) being accurately explained by a moderate amount of overshoot. However, a significant overshoot region does not need to be included in the solar model because the transition between the fully adiabatic envelope and the underlying radiative region is already well reproduced by models without overshoot (see Bressan et al., 2012). Nevertheless, this does not imply that convection cannot penetrate just below the fully adiabatic region in the form of radiative fingers and possibly induce significant mixing (Christensen-Dalsgaard

et al., 2011).

Overshoot (either local or not), semiconvection and breathing pulses may significantly increase the amount of helium in the core, increasing the helium–burning lifetime. However, these effects have a greater impact on the next phase of stellar evolution; the early asymptotic giant branch (EAGB). Under these conditions, the star would enter this phase with a larger helium–exhausted core and the time spent in the double shell phase would be significantly shorter. Convective mixing can alter a star irreversibly and so is a key aspect of stellar evolution, yet it is still unknown whether it is associated with significant overshoot. This extra mixing can affect surface chemistry, luminosity, temperature, which it turn determines MS termination, altering advanced evolutionary stages such as RGB, HB, RC and EAGB.

1.3.4 Diffusion

Element diffusion in stars is driven by a number of processes: gravity (pressure gradients), radiation pressure, and temperature gradients. Radiation pressure in the core of low–mass stars is negligible and so is generally ignored. Gravity tends to concentrate heavier elements in the centre, while lighter elements are pushed to the surface. However, electrons and light ions are held back by an electric force, counteracting the gravitational pull. Convection contributes to thermal diffusion, transporting cool material inwards and hot material towards the surface, while concentration gradients oppose this. Diffusion influences the element abundances and distributions, and the radiative opacity in different regions in the star, which in turn affects the neutrino fluxes and oscillation frequencies.

The most important (and currently unresolved) factor in diffusion is the rate and efficiency at which it occurs in stars with almost radiative envelopes (for a full discussion of diffusion effects, see VandenBerg et al., 2012, and references therein). Diffusive mixing is dominant in stars immediately following a core helium–flash, since convective helium–burning only occurs for 10% of this time (Bildsten et al., 2012). Thermal diffusion dictates the CFP lifetime as the helium fusion site moves inwards towards the core centre (recall Section 1.2; Thomas, 1967; Serenelli & Weiss, 2005).

There is evidence to suggest microscopic diffusion is prevented from occurring in the external layers of metal–poor stars, to a depth of at least 0.005 $M_{\odot}$ from the photosphere, and then partially prevented in the region 0.005–0.01 $M_{\odot}$ from the

photosphere (VandenBerg et al., 2012). Microscopic diffusion is already partially prevented in the external layers of higher–metallicity stars (of similar mass) by the extended external convection, due to higher opacity. When external convection disappears, the surface composition can be noticeably affected by diffusion, even for relatively high stellar masses (Turcotte et al., 1998). To account for these changes, extra mixing must be employed beyond the base of the external convection layers (for example, Richer et al., 2000). This extra mixing (of undetermined origin) limits other diffusive processes and is parametrised as a turbulent diffusion (VandenBerg et al., 2012). A calibrated coefficient, specific to the model's parameters, can be determined from observed surface abundances of old stars, and implemented if desired.

Although there has been much study towards understanding post–MS evolution, there are still many open–ended questions, as well as obvious areas for improvement in modelling certain stellar processes.

1.4 This Project

The theory behind the HeF event is well understood but observational evidence for its occurrence is virtually nonexistent because the effects on surface properties of the star are subtle, and the very rapid evolution immediately preceding and following the HeF. For these reasons, the precise details of the process, which involves the complete rearrangement of the stellar structure in a turbulent and non–equilibrium process, remain unclear. This project takes two approaches towards trying to further understand the properties of red giants in the CFP, and how to search for them. The preliminary method involves investigating metallicity bias and lifetimes of red giants (Chapter 2). From this, the evolutionary rates of stars travelling from the TRGB to zero–age horizontal branch (ZAHB) could be estimated based on stellar age and metallicity. This is detailed in Chapter 3. The second approach is to analyse changes in variable stars' periods to determine identify possible HeF candidates (Chapter 4). Finally, conclusions made from both methods are summarised in Chapter 5.

1.4.1 Metallicity Bias and Lifetimes of Red Giants

The relative numbers of highly evolved, low–mass stars as a function of colour (dependent on metallicity and temperature) and magnitude, in combination with

simulated stellar evolution tracks, can be analysed as a way to gauge the evolutionary rates of RGB stars and build on current models. The lifetime of an RGB star is strongly dependent on its mass and metallicity, with low–metallicity stars evolving through the RGB phase more slowly than high–metallicity stars, and higher mass stars evolving more quickly than low–mass stars, at a given age (demonstrated in Chapter 2). Because the mean mass of stars on the RGB decreases with time, this also translates to an age–dependence. The biases inherent in metallicity distributions of observed RGB stars are investigated in Chapter 2, where the competing effects of age and metallicity on red giants are further explained. From these results, evolution rates for the CFP for differing age and metallicity values are estimated (Chapter 3). This study of RGB lifetimes is expected to identify which stellar populations will provide the most likely combination of age and metallicity for CFP stars, and thus shape the kinds of environments in which they are likely to be found.

1.4.2 Variable Stars

Variable stars undergo changes in luminosity over time and can be a very important tool in the quest to determine the nature of stellar interiors and how they evolve. The variability may be due to internal driving forces, or external influences, including being part of an eclipsing binary system. Intrinsically variable stars can provide insight into the structure and processes occurring inside the star. In some cases variable stars change periodically, implying a periodic driving force, but in other cases their light–curves vary seemingly at random. Significant changes in the periodicity (both negative and positive) are expected to occur when a star nears the end of the HB phase and starts their ascent of the AGB. During the CFP, large negative period changes are expected in most cases. Thus, identifying such cases was the primary goal here.

The analysis in Chapter 4 looks into changes in the periodicity of intrinsically varying, low–mass stars that have evolved past the RGB. RR Lyrae and Type II Cepheids variable stars represent a way to observationally probe the rare population of stars undergoing a HeF because their periods and light curve shapes are highly sensitive to the internal structure of the star. Although stellar evolution occurs on a thermal and not a nuclear timescale after the HeF, total brightness changes might still take decades or centuries to observe. Much work using observations of variable stars has been done on investigating stellar atmospheres,

stellar modes and oscillations (for example Chen et al., 2013; Derekas et al., 2004; Kunder et al., 2011), or using the variables to determine galactic structure (for example Soszyński et al., 2009, 2010a, 2011a). However, there has been little work done beyond simulations, investigating the effects of pre– or post–HeF evolution on variable stars.

Chapter 2

Red Giant Lifetimes and Metallicity Bias

For certain rapid stellar evolutionary phases, like the CFP, calculations and simulations are currently the best way to study the internal processes. Sophisticated models are crucial to accurately simulate observations. In order to improve the next generation of chemical evolution models, more accurate input data, such as the metallicity distribution function (MDF), is required.

The buildup of chemical elements over time is a fundamental process whose details are a key part our understanding of the physics of the star–gas cycle in galaxies. To observationally measure the chemical evolution of the Milky Way (MW) in the solar neighbourhood, the classic approach has generally been to study the MDF of stars with MS lifetimes longer than the age of the Universe ($M/M_{\odot} \lesssim 0.8$), so that the sample accurately represents the relative numbers of stars of all ages. An unbiased sample that can be directly compared to the predictions of chemical evolution models can thus be obtained (van den Bergh, 1962; Tinsley, 1976). The problem with this is that the G and K dwarf stars which meet this criterion are very faint ($M_V \gtrsim +5$), and therefore hard to observe.

The most easily observed abundances in external galaxies are those of very luminous and massive stars and the gas phase, nebular abundances. Both of these provide a snapshot of the end result of billions of years of activity, introducing a high degree of model–dependence into conclusions about the the galactic chemical evolution. At older ages, red giants (spectral type K or early M) are the easiest type of star to observe for a very wide range of ages from the oldest stars in a galaxy to populations as young as ~ 1 Gyr.

In recent decades, and particularly since the advent of 8–10 m class telescopes, abundance measurements of hundreds to thousands of red giants in MW satellites, isolated Local Group dwarfs, and in M31 and its satellites have been made (for example, Suntzeff et al., 1993; Tolstoy et al., 2003, 2004; Cole et al., 2005; Kirby et al., 2011a,b; Ho et al., 2015; Ross et al., 2015; Kirby et al., 2017). A potential problem with this choice of target is that RGB stars do not meet the immortality criterion that made dwarf stars the preferred targets for nearby stellar samples, potentially complicating the interpretation of the observed metallicity distribution functions.

As discussed in Chapter 1, the position of a red giant in colour–magnitude space depends not only on the stellar metallicity (for example, Da Costa & Armandroff, 1990), but also to a lesser extent on stellar age (since the radius of a star dictates its mass on the Hayashi track Hayashi et al., 1962; Cole et al., 2005).

The number of stars available to measure depends on the past star formation rate (SFR) of the galaxy and the initial mass function (IMF). Where a metallicity distribution function of red giants is directly observed in a resolved stellar population, it is unlikely to represent the true proportion of heavy elements as a fraction of the total stellar mass of the galaxy, due to the finite lifetime of the red giants. Investigating how these factors interact within the observational selection of a spectroscopic sample from a well–defined region of the CMD, may lead to constructing an MDF closer to the true MDF. Other complications, such as the alteration of surface abundances due to heavy element diffusion or dredge–up, are beyond the scope of this research.

2.1 Red Giant Star Lifetimes

In a galaxy with a very wide range of stellar ages, the RGB can include stars with a range of masses ($\sim 0.8 - 2\mathrm{M}_{\odot}$). This is due to the lifetime of an RGB star being inversely proportional to its mass (discussed in Chapter 1). This potentially wide range of masses included in a sample must be treated with care to avoid biases caused by the shape of the IMF ($\phi(m)$) and evolutionary lifetime effects. The IMF is an empirical function that describes the distribution of initial masses for a population of stars and is often given as a probability distribution function for the mass (m) at which a star enters the MS. Hence, it is often normalised such that

$$\int_0^\infty m\phi(m)dm = 1. \tag{2.1}$$

The key properties of the IMF that must be considered when creating a model are the log–normal shape at lower-masses, the power–law behaviour at higher–masses, and the peak and width of the function. However, the IMF is often just expressed as as a simple power–law relation of the relative number or fraction of stars with initial masses between $(m, m + dm)$:

$$\phi(m)m^{-\alpha} = constant, \tag{2.2}$$

where α is usually given as ~ 2.35, first derived by Salpeter (1955). The Salpeter slope of $\alpha \approx 2.35$ is applicable when stellar mass is above ~ 0.5 $M_\odot$ (within the Milky Way), while a more gentle slope ($\alpha = 1.3$) is present for masses below this (Kroupa, 2001; Chabrier, 2003).

The IMF can be related to the SFR ($\psi(t)$) as follows:

$$N = \phi(m)\psi(t)dmdt, \tag{2.3}$$

where N is the number of stars formed during times $(t, t + dt)$, within the mass range above.

For a given $\psi(t)$, the total mass of stars integrated along an isochrone, between the limits $(m, m + \Delta m)$ is

$$M_{\rm tot} = \int_m^{m+\Delta m} m\phi(m)dm. \tag{2.4}$$

In real observations, stars are selected from some sample region in the CMD, frequently chosen to be within some well–defined colour and magnitude limits. In external galaxies, these are usually well above the MS turnoff. This selection translates to the corresponding upper and lower mass limits, which are functions of age and metallicity. An illustration of the impact of this choice is shown in Figure 2.1, which shows the mass range of post–MS stars in the isochrones published by Bressan et al. (2012, see Section 2.2) as a function of age and metallicity.

For ages $\lesssim$2.5–3 Gyr, there is a steep increase in the mass difference between the MS turnoff and the most massive star still shining with decreasing age. This directly relates to the number of stars observable at any moment in time. This could partially cancel or even outweigh the tendency of IMF–weighting to produce

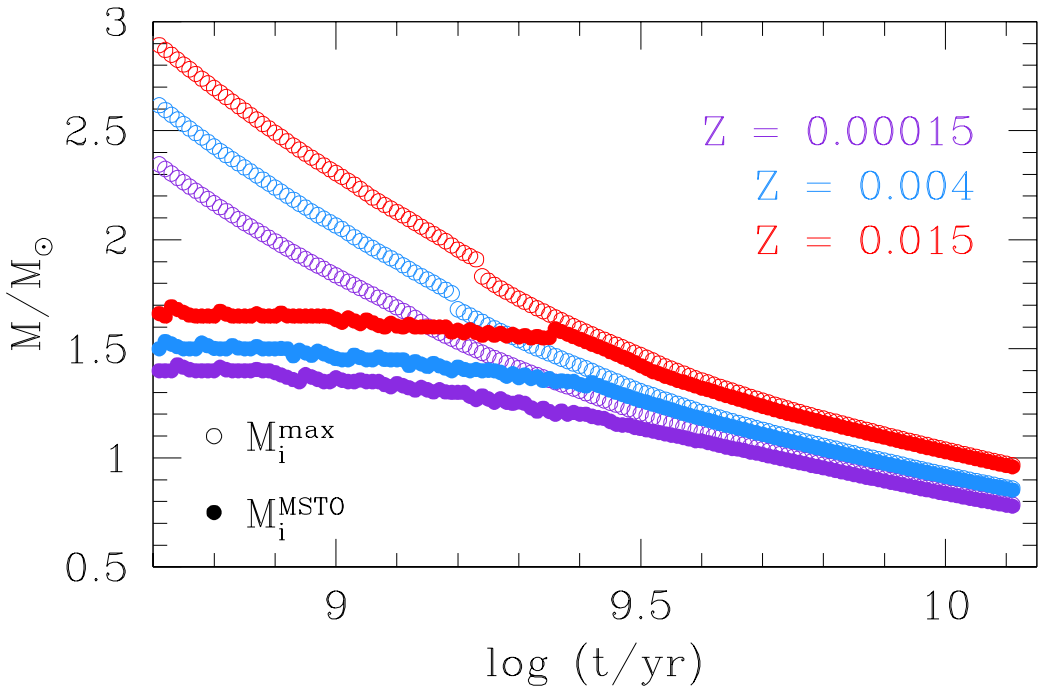

Figure 2.1: Mass range of stars in post–MS phases as a function of age and metallicity. Data are from the PARSEC isochrones (Bressan et al., 2012). Following Renzini & Buzzoni (1986), the initial mass of stars at the MS (MSTO) and the maximum initial mass of post–MS stars (M^{max}) are shown. The number of stars in an observed sample of red giants depends on both the average red giant mass and the mass range on the RGB, introducing the possibility to bias sample statistics toward younger ages.

more stars of low mass than high mass, which favours older stars in observed samples. At a given age, higher metallicity stars have a higher mass, which would tend to suppress their numbers through the IMF, but also a larger mass range, which would tend to increase their representation in a population. In this way, an unbiased selection of stars from an observed CMD can produce a MDF which is skewed compared to the true distribution of heavy element abundances in the galaxy. Thus, to avoid any such bias, simulated data is used rather than observational.

Since the colour of a star depends on its temperature and metallicity (as well as other often minor factors such as dust obscuration), CMDs can be important tools for determining these properties. However, the position of the RGB on the CMD also depends slightly on the age through a shallow dependence of the stellar radius on mass. This is usually only significant for stars much younger

than $\sim$ 10 Gyr. In addition, different combinations of age and metallicity can recreate similar distributions of stars. For a given age, metallicity determines the position of a star on the CMD because metal–rich stars are redder than metal–poor ones. Younger stars are generally more metal–rich, while older stars have much lower metallicities. Since the age of the star affects the temperature, in turn it too influences the colour and so exists an age–metallicity degeneracy in RGB stars.

The competing effects of age and metallicity on the mean mass and mass range of RGB stars are not easily disentangled analytically, but are amenable to simulation using stellar models if the IMF, and observational selection effects can be investigated and possibly compensated for. The magnitude and direction of the effects illustrated in Figure 2.1 will also depend on what fraction of the total post–MS mass range is sampled, that is, on the colour and magnitude range chosen for the observation sample.

2.2 PARSEC Isochrones

An individual star (with a set initial mass and chemical composition) can be modelled over a section of its lifetime by performing calculations at discrete timesteps. This process produces stellar evolutionary tracks. Isochrones are complimentary to evolution tracks and are much more useful for analysis of entire stellar populations. They are derived from sets of stellar evolution tracks with a range of initial masses but the same initial chemical composition, representing the ideal case that the stars formed at the same time from a homogeneous cloud.

Synthetic CMDs were simulated here using theoretical isochrones generated by the on-line resource CMD 2.7[1], version 1.2S of PARSEC: the **Pa**dova and T**r**ieste **S**tellar **E**volution **C**ode (Bressan et al., 2012; Tang et al., 2014; Chen et al., 2015). The original version of PARSEC was an updated version of the code implemented in PADOVA to compute evolutionary tracks, and previously used by the astronomical community to create stellar models using population synthesis techniques. PARSEC covers from the pre–MS phase up to when a star either joins the thermally pulsating–AGB, or when it starts igniting carbon. Evolutionary stages from this point up to the complete ejection of the envelope are presented in accompanying papers (Marigo et al., 2013, 2017; Rosenfield et al., 2016). For the

[1] `http://stev.oapd.inaf.it/cgi-bin/cmd`, 18-02-2016

metallicity range $0.0001 \leq Z/Z_{\odot} \leq 0.04$, masses $0.1 \leq M/M_{\odot} \leq 150$ simulated. The parameters chosen in PARSEC simulate the presence a large semiconvective region after the central helium mass fraction falls below roughly 60% (see Figure 1 of Bressan et al., 2015). PARSEC also uses updated input physics such as EoS, opacities, microscopic diffusion and nuclear reaction rates; and is based on a newer reference solar composition from Caffau et al. (2011).

A variety of input parameters can be altered in PARSEC. For these simulations, the default options on mass-loss and circumstellar dust were used, and a mixed log–normal plus power–law IMF was adopted from Chabrier (2001). PARSEC currently uses Reimers Law to calculate mass loss on the RGB, the use of which may lead to inaccuracies in the predicted stellar masses since mass loss values along RGB differ greatly with metallicity (see Kalirai et al., 2007; Catelan, 2009; Kalirai et al., 2009). The shortcomings of using Reimers Law were discussed previously in Chapter 1. However, since calculations of the evolutionary rates do not require use of mass values, it is not expected to significantly influence results here.

For conversion to the observer plane, the colour–magnitude system for the Hubble Space Telescope Advanced Camera for Surveys (HST ACS) filter set was used, as this is characteristic of the best–quality photometry of most Local Group dwarf galaxies. Bandpasses ACS I–band (F814W) and V–band (F555W) were used here. This is sufficiently close to standard ground–based V– and I–band measurements for this analysis. Four representative isochrones were shown in Figure 1.2, in the previous Chapter, for a typical range of absolute magnitudes to directly compare the differing effects of age and metallicity on the RGB shape.

2.2.1 Modelled Stellar Processes

PARSEC stellar isochrones model properties such as opacity, reaction rates, diffusion, and energy transport under a number of different conditions (see Bressan et al., 2012, for details). Opacity depends not only on density and temperature, but also on the chemical composition of the gas, which can be specified using the following parameters: the total metallicity (Z), hydrogen abundance, and the distributions of the heavy elements, which depend on the specific case being considered. Bressan et al. (2012) combined molecular opacities computed using the `aesopus` code[2] (see Marigo & Aringer, 2009), with the high tempera-

[2] `http://stev.oapd.inaf.it/aesopus`

ture data from the Opacity Project At Livermore[3] (OPAL, see Iglesias & Rogers, 1996, and references therein) in order to generate opacity tables with any initial chemical composition of elements from hydrogen to uranium. Using the revised code, Bressan et al. (2012) were able to predict the stellar evolution for a given complex chemical structure. This included different degrees of CNO abundances, enhancement/reduction in α–elements, and C–N, Ne–O and Mg–Al abundances. In addition, a total of 42 reaction rates were implemented in PARSEC, including α–capture reactions (which are generally the most important), as well as pp chains, the CNO cycle, the Ne–Na, and Mg–Al chains. These are the nuclear reaction rates recommended by the JINA REACLIB database (Cyburt et al., 2010).

In the PARSEC model, the energy transport in convective regions is described according to the mixing length theory (MLT) of Böhm-Vitense (1958), while the temperature gradient is assumed to be radiative in overshoot regions (Bressan et al., 2012). Overshooting from the central convective region must be taken into account for estimations of the convective boundary of the core (Bressan et al., 1981). Bressan et al. (2012) used the MFP of convective bubbles across the border of the convective region as the main factor in determining the overshoot. Since the overshoot parameter must depend on stellar mass, PARSEC uses a variable overshoot parameter.

Bressan et al. (2012) utilised the freely available `freeeos` code[4] (for example, Cassisi et al., 2003) to derive the EoS used in their models. This method minimises the effects of interpolation by computing a set of EoS tables exactly with the initial metallicity and partition of the new set of tracks.

2.2.2 Solar Calibration

Calibrating stellar evolution models with the Sun is not only a useful test of the prediction accuracy and reliability of the input physics, but solar values are also used to determine parameters that cannot be theoretically calculated; for example the MLT parameter ($\alpha_{\rm MLT}$) and the initial solar abundance of helium and metals. In the PARSEC model the current solar metallicity was taken to be $Z_{\odot}$ =0.01524. In order to calibrate their solar model, Bressan et al. (2012) computed a large number of evolutionary tracks from the PMS phase to an age of 4.8 Gyr, varying the initial composition of the Sun, the initial abundance of helium ($Z_{\rm ini}$), the

[3] `http://opalopacity.llnl.gov`

[4] `http://freeeos.sourceforge.net`

$\alpha_{\rm MLT}$, and the extent of the adiabatic overshoot at the base of the convective envelope Λ_c, but keeping the mass constant at 1 $M_\odot$. See their paper for values used.

2.3 The Simulations

Synthetic CMDs were created to calculate the number of stars produced along the RGB and subsequent stellar evolution phases over 1 Gyr (or 0.5 Gyr in the youngest case), if the SFR is a constant 1 $M_\odot$/yr. Seven different age ranges were simulated (0.5–1, 1–2, 3–4, 5–6, 7–8, 9–10 and 11–12 Gyr), each with six different metallicities; Z=0.00015, 0.0004, 0.0015, 0.004, 0.015 and 0.04 (equivalent to [M/H] = -2, -1.6, -1, -0.6, 0, +0.4, where [M/H] $\equiv \log_{10}(Z/Z_\odot)$, with $Z_\odot$ =0.01524), for a total of 42 simulations.

Figure 2.2 shows stellar population simulations of the same age–metallicity pairs as in Figure 1.2, while the full set are given in Appendix A. The simulations were named in the following convention: the lower age bin limit serves as the prefix in Gyr and the metallicity ($\times 10^{-5}$) is the suffix. For example, the simulation with metallicity Z=0.004 at an age range of 3–4 Gyr, is called 3g400. The simulated points scattering away from the isochrones are due to the presence of binaries; this most often manifests as a slight brightening relative to the isochrones, but can be more obvious when the secondary has not yet evolved past the MS stage and is therefore much bluer in colour than the primary.

These synthetic RGBs were created using isochrones interpolated to a very fine grid, spaced by 0.01 in log(age)[5]. Each mass point along each isochrone was weighted by the integral of the Chabrier (2001) IMF over the interval centred on the mass point and extending halfway to the adjacent points. Each point in the isochrones is thus translated to a probability density over a discrete interval. Within a desired age interval, the isochrones are summed to form the total predicted number of stars in each CMD bin. The weights are scaled to reproduce a constant SFR of 1 $M_\odot$/yr over the 1 Gyr span, integrated over all possible stellar masses. The log–normal plus power law IMF from Chabrier (2001) was employed here because the largest differences between this IMF and other commonly–used choices (for example, Salpeter, 1955; Kroupa et al., 1993) occur among the very low–mass stars which do not evolve to the RGB over the ages simulated here.

[5]Years are always used as the unit for age here unless specifically stated otherwise.

All of the relative RGB numbers should scale together, nearly independent of the choice of IMF.

In the simulations, each point in colour–magnitude space from the original PARSEC isochrones is assigned a weight according to the IMF. These weights are smoothed by interpolation between adjacent points to reduce granularity, and then summed and binned to discretise the CMD. Whilst high–metallicity stars will tend to fall onto the red side of the RGB, they will be further spread in colour according to their age variation. On the blue side of the RGB, there will be a mix of young and old stars at low–metallicity, plus the youngest stars of high metallicity.

The probability density distributions from the simulations are resampled to a regular grid of 6000 colour–magnitude bins for consistency across age and metallicity, with a magnitude range of $-4.5 \leq M_I \leq 1.5$ (bin width 0.05) and colour range of $0.75 \leq V\text{–}I \leq 2.25$ (bin width 0.03). The range of initial masses across each bin (ΔM_{ini}) on the RGB is on the order of $\sim 10^{-3} M_\odot$, depending on the age of the stars.

These simulations do not include any synthetic broadening to account for observational errors, (bolometric corrections were already included in the data from PARSEC CMD 2.7) which is reasonable for the commonly encountered case in which the photometric limit of the data is two or more magnitudes fainter than the HB or RC. This allows investigation into the effects of observational selection on the recovered MDF in a general way, independent of the parameters of any single project. In particular, sampling effects are explored in two limiting cases: a) for a given age, the apparent MDF that results from a uniform distribution of metallicities; b) for a single metallicity, the age distribution of observed red giants resulting from a uniform distribution in age. The first case is analogous to a star cluster or burst population that could have multiple metallicities present (for example, the ultra–faint dwarfs investigated by Brown et al., 2014), while the second corresponds to a constant SFR with a flat age–metallicity relation.

2.4 Results

Table 2.1 shows the comparison of stellar masses along the four isochrones shown in Figure 2.2. Values for the mean mass, the change in mass between bright and faint magnitude limits ($-3.5 \leq M_I \leq -2$), and the total mass integrated along each isochrone for that range were calculated. The stellar mass values change with

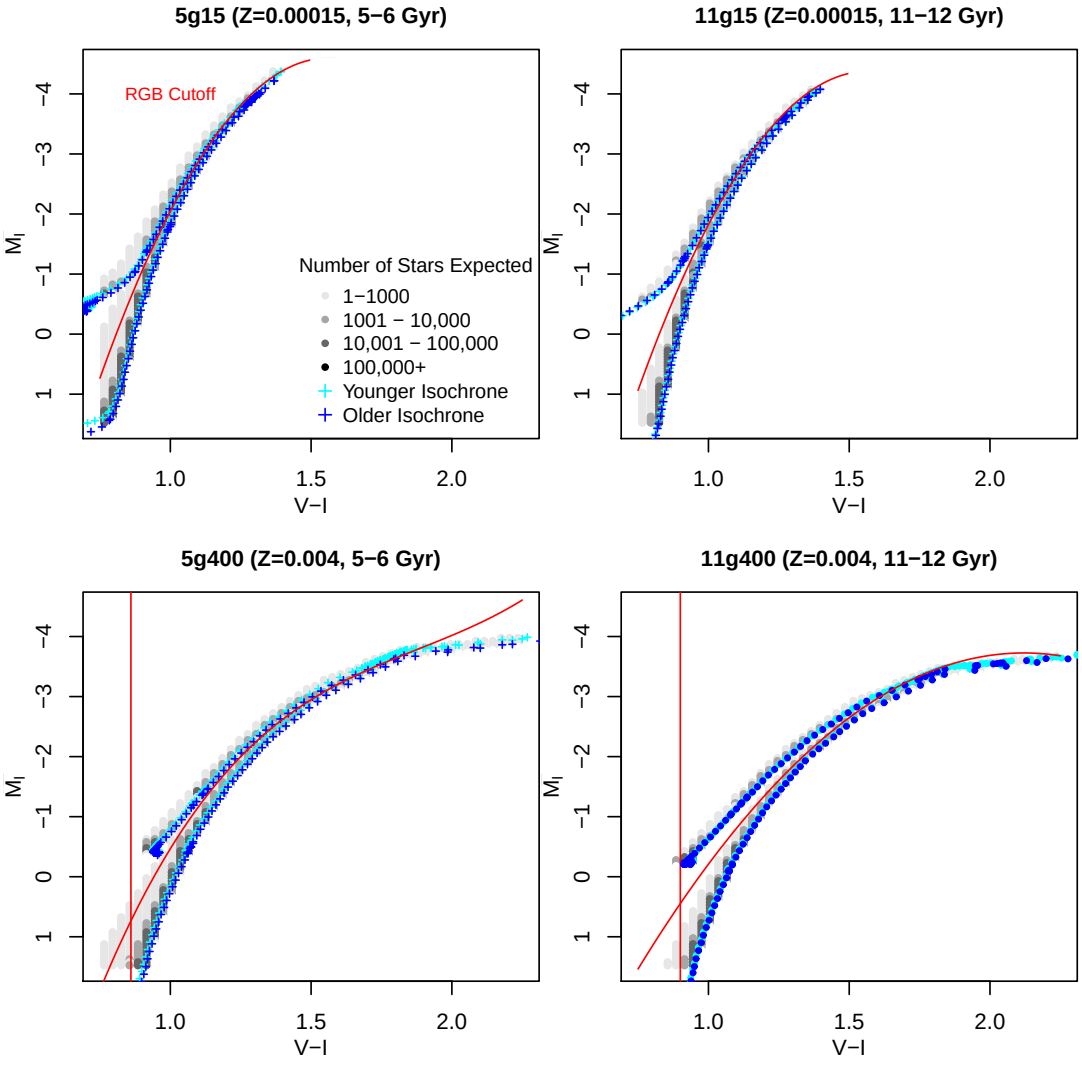

Figure 2.2: Four selected simulated CMDs, with varying age and metallicity, corresponding to four stellar population simulations (shown in Figure 1.2). The full 42 simulations are shown in Appendix A. The legend shown in the top left plot applies to all four CMDs. The red vertical line in each plot represents the individual BL and HB colour–cutoff determined for each simulation, where possible. The red parabola is the cutoff between AGB and RGB stars. The older and younger isochrones represent the upper and lower age limits of the simulation; in these cases, spanning a range of 1 Gyr (or 0.5 Gyr in the youngest case). See Section 2.3 for details.

	5g15	**11g15**	**5g400**	**11g400**
$\bar{\mathrm{M}}$	0.9826	0.7692	1.059	0.8831
$\mathbf{\Delta M}$	0.0793	0.0710	0.1095	0.1020
$\mathbf{M}_{int}$	190.6	83.07	264.8	82.13

Table 2.1: Mean stellar mass ($\bar{\mathrm{M}}$), change in stellar mass (ΔM), and the total mass integrated along the isochrone (M_{int}) is calculated for the select isochrones shown in Figure 2.2 (ages 5-6 Gyr and 11-12 Gyr, with Z=0.00015 and 0.004, corresponding to the simulations 5g15, 11g15, 5g400, 11g400 respectively). Masses are given in units of $\mathrm{M}_{\odot}$ and are derived from the colour–magnitude range $0.75 \leq V - I \leq 2.25$ and $-3.5 \leq M_I \leq -2$.

both age and metallicity, but to different degrees, demonstrating the complicated degeneracy that exists between the two. Figure 2.2 shows that metallicity has a greater effect on the shape of the isochrones than age, and at low metallicity the age effect diminishes. These masses determine the number of RGB stars within the colour–magnitude selection window for each of the 10^9 $\mathrm{M}_{\odot}$ simulations.

Bias factors were calculated for correction of metallicity distribution functions measured from RGB stars by comparing the number of stars populating the spectroscopically-sampled areas of the CMD to the total number of stars formed in each simulation. The analysis was performed separately over two magnitude ranges $-4.5 \leq M_I < -2.5$ and $-2.5 \leq M_I < 1.5$ in order to investigate trends in bright and faint stars separately. The results can be expressed as a single number for each age and metallicity, representing the maximum fraction of all stars formed that could be spectroscopically measured in the given CMD selection region.

A complex relationship exists between age, metallicity, and stellar density in the synthetic CMDs, differing greatly between the two magnitude ranges. Figure 2.3 shows four contour plots: the top images (subplots (a) and (b)) show the brighter magnitude range, while the bottom (subplots (c) and (d)) show the fainter range, cut off above the HB. Panels (b) and (d) account for only the RGB stars, while panels (a) and (c) only exclude stars based on a minimum colour, and so include PAGB, AGB, HB, BL and RC stars.

The main result is that in a mixed population of stars, a sample of stars drawn from the RGB will be biased towards younger ages, making it less likely to detect older populations. While it could be naïvely assumed that old stars are over–represented because of the IMF effect, here it is evident that in fact they are under–represented. As demonstrated above and shown in Figure 2.1,

the number of stars observed is proportional to the integral of the luminosity from one magnitude level to another. On the RGB, this directly translates to an integral of the IMF from one mass to another. At younger ages this mass interval is larger than at old ages.

At a given age, generally low–metallicity stars are more likely to be observed than high–metallicity stars, but the size of the effect is not as dramatic as the variations with age. One might assume that including fainter stars would improve the sampling by reducing the biases, however this does not seem to be the case based on the comparison between the upper and lower panels of Figure 2.3. Panel (c) of Figure2.3, shows that for fainter stars, the metallicity dependence is reversed. Another factor is the larger separation of the RGB and the AGB at higher metallicities - the AGB of the older stars in the age range overlaps with the RGB of the younger stars, making removing the older AGB stars using morphology impossible. This also increases the relative number of stars in this region of the CMD.

Singling out the RGB phase in the analysis gives very different age–metallicity distributions compared with the case when all the surrounding stellar phases (PAGB, AGB, BL, HB, and RC) are included. This is shown in panels (b) and (d) of Figure 2.3. This highlights the benefit of clean separation between stellar sequences with high–quality photometry, where the star formation history (SFH) allows it. A more detailed analysis of the relations between the age and metallicity for the synthetic populations is provided in Section 2.4.1 along with age and metallicity distributions (see Figures 2.4, 2.5).

2.4.1 Age and Metallicity Distributions

In order to thoroughly investigate the behaviour within the contour plots (Figure 2.3), both metallicity and age distributions are included here, normalised in three different ways, shown in Figures 2.4, and 2.5. The first method was simply to normalise over the total stellar population across all 42 simulations, for each magnitude range. The other methods were to normalise over either an entire metallicity or age population for each magnitude range. For example, the simulation 11g15 was normalised over the total number of stars with ages between 11 and 12 Gyr in panels (c) and (d), and normalised with respect to the total number of stars with metallicities of Z=0.00015 in panels (e) and (f).

Figures 2.4 and 2.5 respectively show the two limiting cases investigated here:

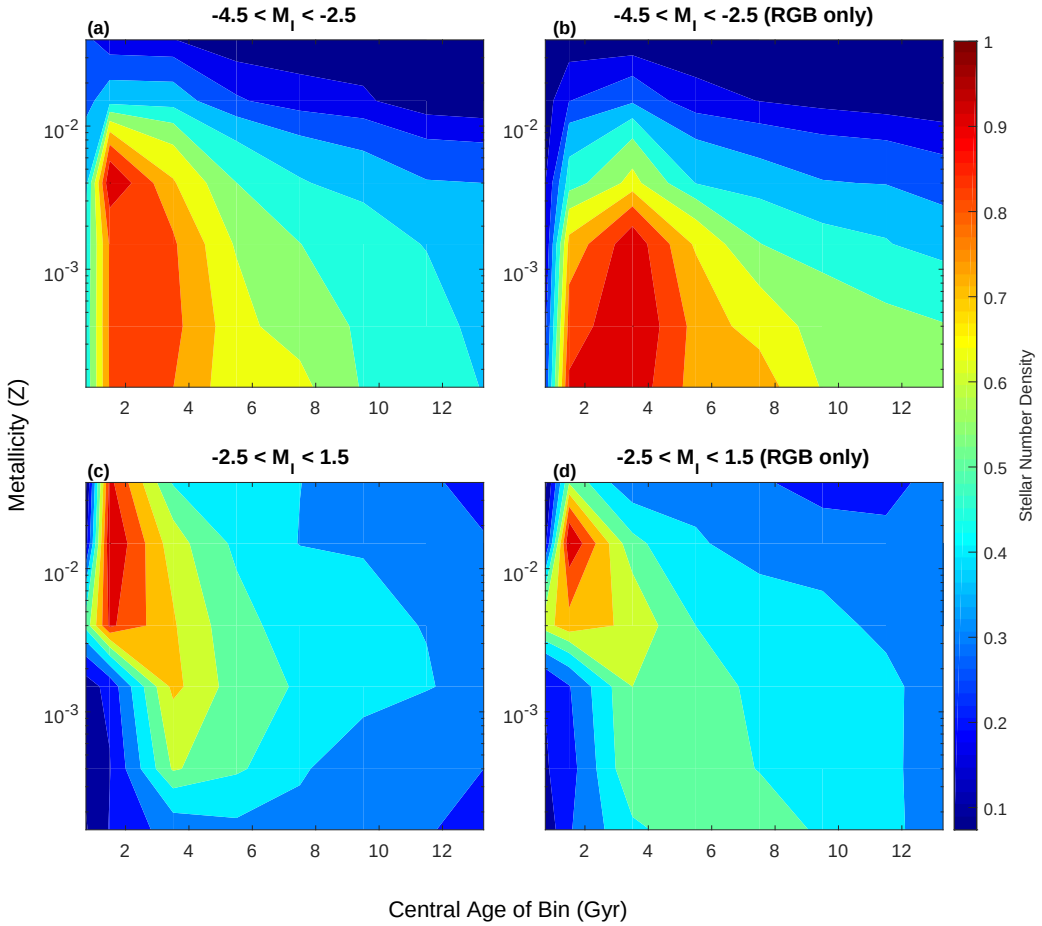

Figure 2.3: The age–metallicity distribution of the 42 simulated RGBs over two magnitude (M_I) ranges. Subplots (b) and (d) have the PAGB, AGB, BL, HB and RC stars removed from the sample (see Section 2.3 for details). The colour–scale background represents the predicted relative density of stars based on a constant SFR and flat AMR. The values have been normalised for ease of comparison. These correction factors are listed in Appendix B.

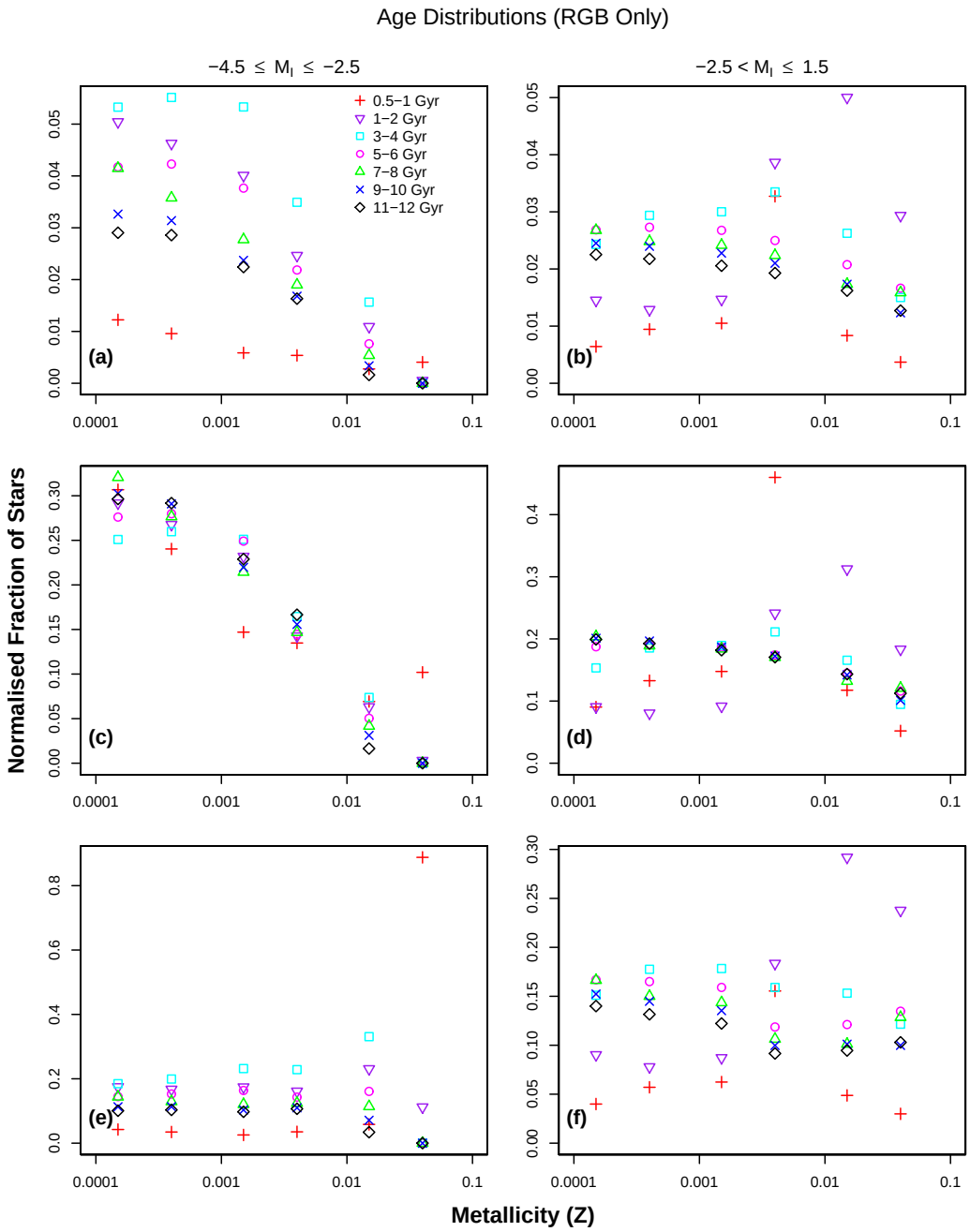

Figure 2.4: Age distributions of red giants shown for both magnitude ranges. The three rows of plots are normalised to different totals (see Section 2.4.1), with panels (a) and (b) normalised to the total population, panels (c) and (d) normalised to each age population, while panels (e) and (f) are normalised to each metallicity population. The legend shown in panel (a) applies to all six plots. These data are also presented in the contour plots in Figure 2.3 (panels (b) and (d)) and the metallicity distributions in Figure 2.5 for comparison. Note the different scales for the stellar number densities.

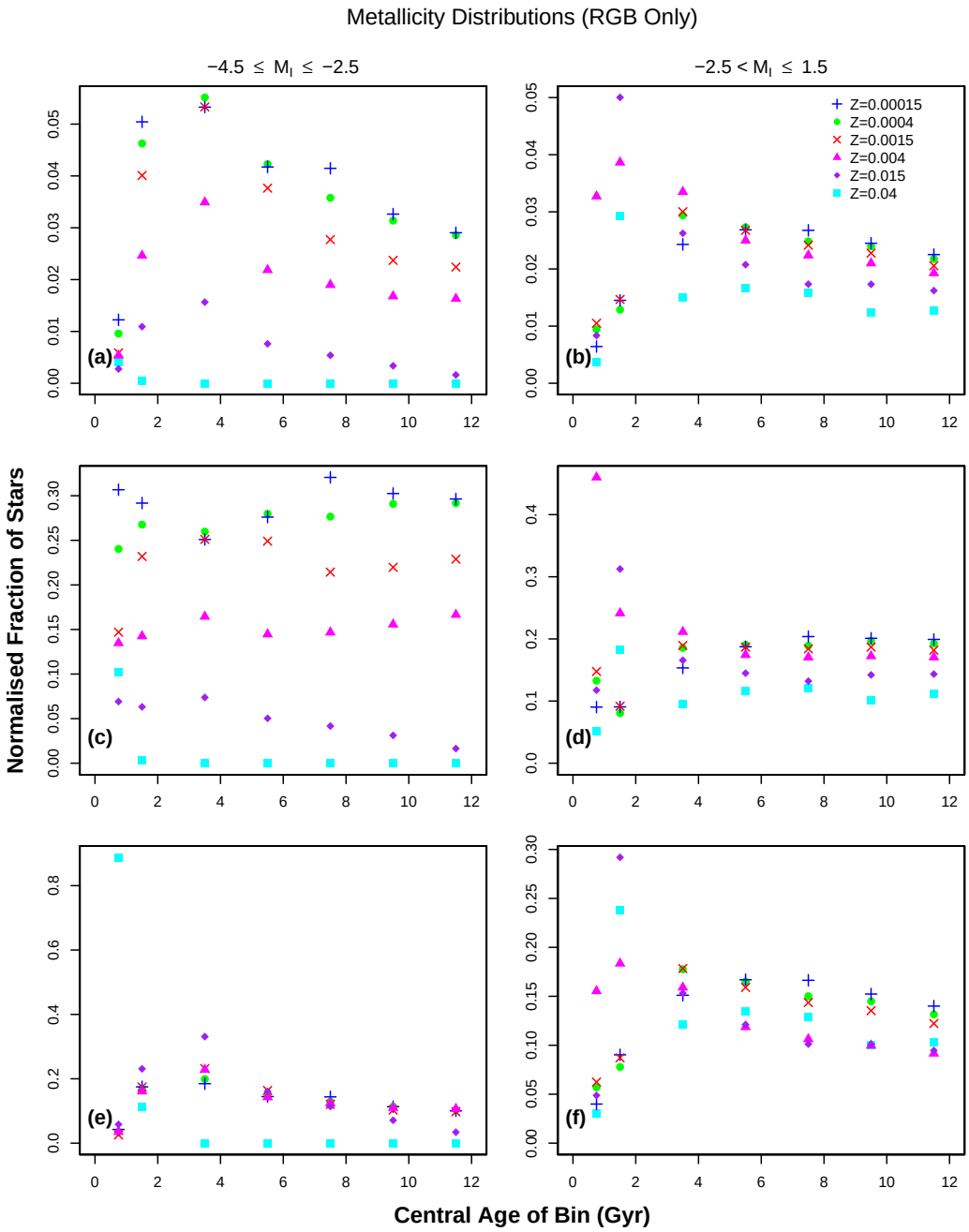

Figure 2.5: Metallicity distributions of red giants shown for both magnitude ranges. The three rows of plots are normalised to different totals (see Section 2.4.1), with panels (a) and (b) normalised to the total population, panels (c) and (d) normalised to each age population, while panels (e) and (f) are normalised to each metallicity population. The legend shown in panel (b) applies to all six plots. These data are also presented in the contour plots in Figure 2.3 (panels (b) and (d)) and the age distributions in Figure 2.4 for comparison. Note the different scales for the stellar number densities.

a) for a given age, the apparent MDF that results from a uniform distribution of metallicities; b) for a single metallicity, the age distribution of observed red giants resulting from a uniform distribution in age. Each stellar age group shown in Figure 2.4 represents a population of stars formed in the same event (for example, a star cluster), and their spread across a range of metallicities. Figure 2.5 shows the observable numbers of red giants under the conditions of a flat AMR and constant SFR.

Figure 2.4 shows the age distributions for each normalisation method, over magnitude ranges of $-4.5 \leq M_I < -2.5$ and $-2.5 \leq M_I < 1.5$ separately. Shown clearly in Figures 2.4 and 2.5, stars aged between 0 and 4 Gyr are the most unpredictable and often follow different trends to the older stars. Each age sub–population follow similar trends at brighter magnitudes, whereas over the fainter interval, the metallicity relations in each age range behave very differently. The artificial exclusions of the AGB, HB, BL and RC stars in the CMDs, which occur mainly at fainter magnitudes, could be partly responsible for panels (b), (d), and (f) in Figure 2.4 being less smooth than their bright counterparts. These exclusions were implemented manually for the most part and could introduce a small degree of inaccuracy into the data. However, it could not account for the significantly different AMRs between the two magnitude selection ranges, as evident by the fact that the metallicity distributions show the opposite trend (Figure 2.5). This is further evidence that observations need to be carefully planned to avoid biases introduced by not properly considering the inclusion or exclusion of the fainter stars. Figure 2.5 shows the metallicity distributions in a similar manner. The plots in these Figures make obvious that the high–magnitude behaves very differently to the low–magnitude population, so careful modelling is required to interpret any observations.

The obvious outliers in panel (e) of both Figures 2.4 and 2.5 represents the same data point. It demonstrates that the vast majority of metal-rich red giants (here Z=0.4) are very young (0.5–1 Gyr).

2.5 Discussion

The relationship between the observational sample selection of red giant stars and the true metallicity distribution has been investigated by simulating 42 CMDs with varying ages and metallicities. Comparing the number of stars populating each region of the CMD allowed for the calculation of approximate correction

factors to implement in current models. While the need to account for variable stellar lifetimes was appreciated very early on in the integrated light study of galaxy spectra (for example, Renzini & Buzzoni, 1986) and is easily taken into account by the procedures needed to fit whole-of-population line indices (see for example Trager et al., 2005), the issues in drawing inferences from samples of individually selected giants have been explored much less thoroughly.

2.5.1 Bias Corrections Applied to Real Data

The synthetic RGBs constructed here assume a constant SFH and a flat AMR, thus the number density contours in Figure 2.3 cannot be applied directly to a real stellar system without first accounting for the SFH and chemical evolution. Cole et al. (2009) and Dolphin (2016) have advocated simultaneous modelling of the SFH from deep–photometry and spectroscopy of a subset of bright stars but in many cases this is not practical. The age–metallicity contours in Figure 2.3 were constructed using a constant SFH and a flat AMR, which is equivalent to assuming no chemical enrichment over time, and no gaps or spikes in the SFR. To apply a correction, the number of stars in each age band should be scaled by the SFR. Some degree of knowledge about the SFH is required in order to apply these corrections, which is a limitation inherent to the use of chemical evolution probes with finite lifetimes.

Dwarf Irregular Galaxies

As an example of how to apply and use these corrections, Kirby et al. (2017) calculated scaling factors for metallicity distributions of Leo A and Aquarius, based on the SFH and AMR from Cole et al. (2014) and the simulations presented here. Although the correction did not have much effect on the Aquarius metallicity distribution, the mean metallicity of Leo A was calculated to be 0.07 dex lower than the observed value. The overall shape of the Leo A metallicity distribution was also affected. Changes in the mean metallicity and the distribution shape may lead to a different chemical evolution model being a better representation of the data. In this case, the corrections to the metallicity distribution of Leo A resulted in the shape being slightly less peaked, meaning that the pre-enriched model was more favoured over the accretion model than from the analysis of the uncorrected data (Kirby et al., 2017, see their Figure 10).

Large Magellanic Cloud Bar

Cole et al. (2005) presented spectroscopic metallicities for 373 red giants in the Large Magellanic Cloud (LMC) bar, leading to a very well–defined observed MDF. However, it is reasonable to suppose that the true MDF differs from this; with these calculated correction, the difference can now be modelled directly.

Because the SFH of this region of the LMC is well–constrained, these synthetic RGBs can be used to compare the predicted distribution of red giants to the observed distribution, as well as to provide a corrected MDF for chemical evolution model (CEM).

Only RGB–phase stars were included in the simulated data. A distance modulus of 18.50 is adopted here, to match the valued used by Cole et al. (2005). Hence, the RGB stars in the LMC bar were estimated to be $-3 \leq M_I \leq -2$, which sits comfortably within the simulated range. The 373 observed RGBs from Cole et al. (2005) are shown overlaying the simulated metallicity distribution contours in Figure 2.6. The high–end metallicities were adjusted following Van der Swaelmen et al. (2013) and the ages were re–derived using the same method as Cole et al. (2005), but with the PARSEC isochrones (Bressan et al., 2012) for consistency.

The SFH (which includes the modelled $\psi(t)$ and AMR, derived from broad–band photometry) was taken from Cole et al. (2009). The predicted distribution of RGB stars for the LMC bar is in good agreement with the distribution of observed red giants. At ages less than $\sim$4 Gyr, the metallicity distribution predicted from the CMD is broader than the observed MDF, because the SFH derived from broad–band colours does not strongly constrain [Fe/H]. The distribution of RGB ages predicted by these simulations scaled by the SFH is in good agreement with the distribution of ages predicted from the RGB colours and metallicities alone. This serves to emphasise that the observed RGB sample is biased towards young ages. The median age of the observed sample is 1.9 Gyr while the median age of star formation is $\sim$5 Gyr. The predicted metallicity distribution of LMC bar red giants suggests that stars more metal–poor than the peak are under–represented by $\sim$25% (see Figure 2.7).

Chemical Evolution Models

Cole et al. (2005) did not fit chemical evolution models to their sample, but some work was done in this area by Carrera et al. (2008). In order to overcome

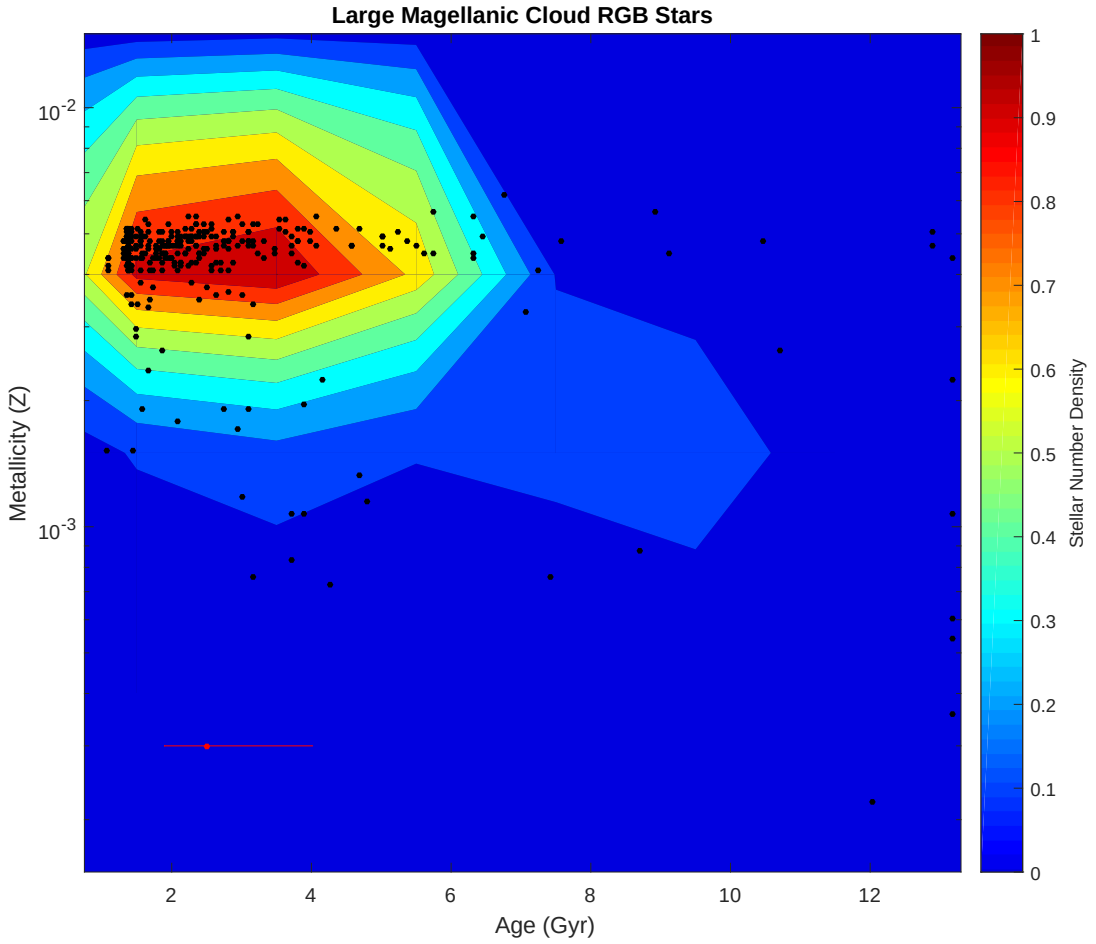

Figure 2.6: Age–metallicity distribution from simulated RGBs, for LMC bar distance reddening, AMR, and SFH. See Section 2.5.1 for details. The black points are the LMC bar RGB stars taken from Cole et al. (2005) and the red point is a representative error bar for the uncertainty in the stellar age. The colour–scale background represents the relative density of stars in the simulations, scaled by the SFH of Cole et al. (2009). Although the SFH is greatly extended, most RGB stars are expected to be 1.5–4 Gyr old.

the age–metallicity degeneracy in RGB stars (see Worthey, 1994), Carrera et al. (2008) combined spectroscopy with deep CMD photometry to calculate the ages for individual RGB stars in the LMC. While this is a good approach in that the MDF alone is not used to determine the ages, the authors did directly use the number of RGB stars to determine the SFH, likely biasing their results against old, metal–poor stars.

Here, the impact of the correction to the MDF (derived above) is tested by fitting simple chemical evolution models to the corrected LMC data following the method by Carrera et al. (2008) (see also Tinsley, 1980; Peimbert et al., 1994, for original derivations), using the instantaneous recycling approximation. The metallicity of the system as a function of time is determined via

$$\mu\frac{dZ}{d\mu} = \frac{y(1-R)\psi + (Z_f - Z)f_I}{-(1-R)\psi + (f_I - f_O)(1-\mu)} \tag{2.5}$$

where μ is the ratio of the gas mass to the total baryonic mass, y is the yield, R is the mass fraction returned to the system after each generation of stars, compared to the total mass of the stars in that generation, Z_f is the metallicity of the accreted gas, and f_I and f_O are the accretion and outflow rates, respectively. The simplest case is that of a pre-enriched closed box with no gas flowing in or out ($f_I = f_O = 0$). Integrating Equation 2.5 to solve for Z(t) gives

$$Z(t) = Z_i + y\ln[\mu(t)^{-1}] \tag{2.6}$$

where Z_i is the initial metallicity of the system. For the case where gas is accreted but none is lost ($f_O = 0$), the derivation by Carrera et al. (2008) is followed, defining the accretion rate to be $f_I = \alpha(1-R)\psi$, where α is a free parameter. Here, it was expected that accreted gas has the same metallicity as present initially in the system (that is, $Z_f = Z_i$), which is not an unreasonable assumption. In the case that $\alpha \neq 1$, Equation 2.5 becomes

$$Z(t) = Z_i + \frac{y}{\alpha}\left[1 - \left(\frac{\mu(t)}{\alpha(\mu(t)-1)+1}\right)^{\alpha/(1-\alpha)}\right]. \tag{2.7}$$

When $\alpha = 1$, the accretion model can be expressed as

$$Z(t) = Z_i + y\left[1 - e^{1-\mu(t)^{-1}}\right]. \tag{2.8}$$

Lastly, a leaky box scenario with no gas being accreted ($f_I = 0$) is considered,

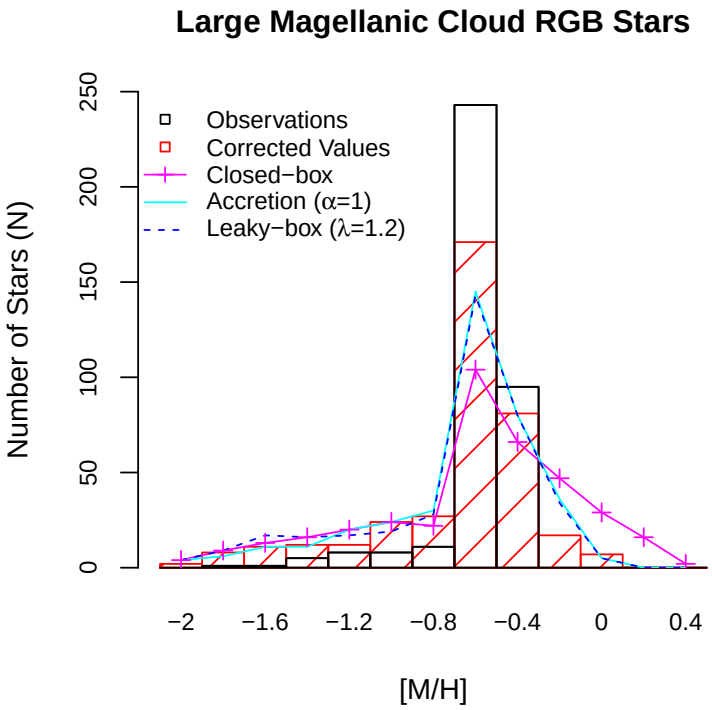

Figure 2.7: Metallicity distribution of the observed LMC bar red giants taken from Cole et al. (2005) shown in black, compared with the corrected MDF shaded in red, along with CEMs adopted from those in Carrera et al. (2008). The full AMRs are shown in Figure 2.8.

where the rate of gas flowing out of the system is $f_O = \lambda(1 - R)\psi$. λ is also a free parameter, and for the case when $\lambda \neq 1$, Equation 2.5 becomes

$$Z(t) = Z_i + \frac{y}{\lambda + 1} \ln \left[\frac{\lambda + 1}{\mu(t)} - \lambda \right]. \tag{2.9}$$

Figure 2.7 shows the metallicity distribution of the observed LMC bar red giants (taken from Cole et al., 2005) compared with the corrected MDF, along with the three simple CEMs; pre–enriched closed box, accretion, and leaky box. A yield of 0.006 was used here, in alignment with the current metallicity of the LMC. For the accretion and leaky box models, values of α and λ were chosen based on the goodness of fit when applied to the metallicity distribution. Equations 2.6, 2.8 and 2.9 were directly used to plot the AMR from each of the models over the LMC stellar distribution in Figure 2.8. The effect of including a SFR contribution from the LMC disc was investigated, but for reasonable values the changes to the AMRs were not significant.

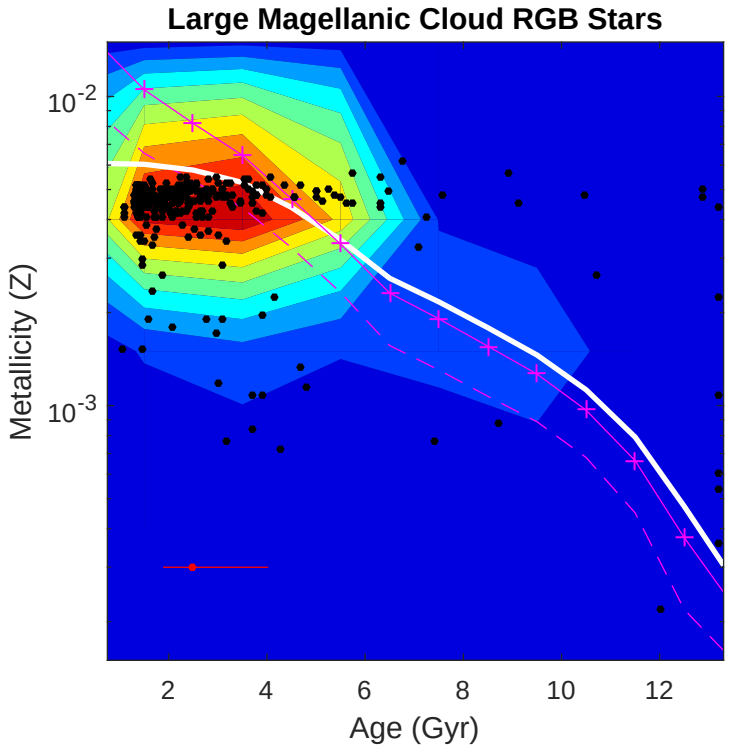

Figure 2.8: As in Figure 2.6, the black points are the observed RGB stars from the LMC bar, with the contours showing the corrected AMR. The best–fit model is the accretion model using $\alpha = 1$ and is shown as the solid white line. The magenta dashed line shows the leaky-box model with $\lambda = 1.2$, and the closed box model is shown with the crossed magenta line. The same CEMs are shown in Figure 2.7.

The metallicity distribution is best represented by either an accretion or a leaky box model when corrections for the sampling bias are taken into account (see Figure 2.7). The only differences between the two are in the low–metallicity tail. Carrera et al. (2008) proposes a model featuring gas moving both in and out of the system as the best representation, with free parameters of $\alpha = 1.2$ and $\lambda = 0.4 - 0.6$. This is equivalent to a net inflow with $\alpha = 0.6 - 0.8$, conditions not significantly different to the closed box model when representing the corrected metallicity distribution. Interestingly, the age–metallicity relation is not well–reproduced by any simple model, because of the large scatter in metallicity at intermediate ages. Increasing the yield value used in the models (to be closer to the value used by Carrera et al., 2008) better reproduces the peak metallicity in the distribution, but shifts the AMR too far to the young, metal–rich corner. The SFH predicts that only a small number of RGB stars older than 6 Gyr should be observed, in agreement with observations, but the high metallicity of stars from 6–12 Gyr is not well–fit by the simple models. The cohort of metal–poor stars at ages 2–6 Gyr is also problematic for the chemical evolution models. It is likely that both more accurate age estimates for the RGB stars are required and more complex models need to be considered, but this is beyond the scope of this research.

2.5.2 Comparison to Previous Work

In a series of papers written by Kirby et al. (2011a; 2011b), the authors derive a SFH using metallicities and α–element abundances. While Kirby et al. (2011a) noted that their selection from a spatial subsection of the galaxies favoured young, metal–rich stars, they do not account for the fact that within this sample stellar lifetimes bias them further against old, metal–poor stars. A corrected MDF could make the conclusions in Kirby et al. (2011c) regarding gas flows even stronger.

Ross et al. (2015) considered photometric rather than spectroscopic measures of the metallicity to examine the MDF of dwarf galaxies. Traditional methods involving the colour of the RGB as a function of magnitude are subject to the age–metallicity degeneracy, but Ross et al. (2015) neatly circumvent that problem by considering colour–colour plots, thus isolating metallicity as the measured parameter. They demonstrate how their method produces observed MDFs that differ from those measured by Kirby et al. (2013) based on spectra of individual giants. While their method samples all giant stars that are present, it still does

not account for the fact, demonstrated here, that their MDFs may still be biased by the over– or under–representation of stars of differing ages. In principle their approach could be generalised by using synthetic colour–colour plots based on isochrones with a wide range of ages.

However, this is a sample selection correction based on the CMD distribution of stars and not on their variable lifetimes. It is well known that metal–rich stars tend to be redder than metal–poor stars for a given stellar age. For metallicities [M/H]> -1, the TRGB no longer occurs at constant I–magnitude, so very metal–rich stars may be under–represented (Reitzel & Guhathakurta, 2002). Thus any selection based on colour could be removing a portion of either the more metal–rich or metal–poor populations. Ho et al. (2015) investigated some of the biases present in current RGB samples, applying corrections to their own MDF. While the sample selection is necessary, it does not take the place of the stellar lifetime corrections derived here.

2.5.3 Future Improvements

In order to apply the corrections derived here, the stellar age distribution needs to be roughly known; ideally this approach should be applied to combined colour–magnitude diagrams and chemical abundance data. While these corrections eliminate/alleviate some degree of the bias present in observed metallicity distributions, there is one main potential source for inaccuracy in the above analysis: determining the HB and BL cutoff point and the separation of the RGB from AGB stars. In other words, how to relate the models to the observed sample. As outlined in Section 2.3, the HB, RC, BL, AGB and PAGB phases were excluded from the sample, while keeping as many RGB stars included as possible. Since the position on the CMD of the HB varied with both age and metallicity, it was not plausible to employ one magnitude limit for every simulation. The colour–magnitude cutoffs are shown in the simulated CMDs available online, and visibly spread out at younger ages and higher metallicity, increasing the uncertainty in the analysis of these simulations in the dimmer magnitude range. Whenever giant star samples are analysed to produce chemical evolution models, the stellar lifetime biases should be analysed using identical selection criteria to the data sample.

The equations derived to RGB stars from the simulations were determined through visual inspection of the separation between the RGB and AGB tracks,

as well as the locations of any BL, RC and any PAGB stars, for each CMD. To maintain consistency, the separation equations were all given as polynomial or logarithm functions. The separation between the AGB and RGB was less pronounced at younger age ranges (0–1 and 1–2 Gyr), but at higher metallicities, the older stars on the AGB overlapped the younger RGB stars for each age limit (see Appendix A for CMD plots of the simulations).

Identifying under– and over–represented populations of red giants in observations will help to improve future chemical evolution models, both for individual stars and galaxies. The stellar number distributions calculated here are used to estimate CFP evolutionary rates across different ages and metallicities in the following Chapter.

Chapter 3

Red Giant Evolutionary Rates

There are many factors to consider when mapping stellar structure and evolution: the initial conditions of the star, the complex processes that take place within the star, and the timescales on which they occur. The conditions in stellar interiors are vastly different to those we can create in a laboratory, and the effects of many stellar processes occurring are subtle and difficult to detect. As such, modelling certain rapid stages in stellar evolution can be difficult and uncertain. The relative numbers of highly evolved, low–mass stars as a function of temperature and luminosity can be analysed as a way to gauge the timescales for structural changes preceding helium ignition and the subsequent return to hydrostatic equilibrium.

As explained in Chapter 2, the position of an RGB star in the CMD depends not only on the metallicity of the star, but also on stellar age. Investigating how these factors interact within a well–defined region of the CMD can aid in determining relative stellar numbers in different stages of evolution, and thus estimate evolutionary rates. This research is expected to identify which stellar populations will provide the most likely combination of age and metallicity for CFP stars, therefore shaping the kinds of environments in which they are likely to be found.

This research combines simulated data from two separate models to investigate CFP evolutionary rates. The first model is the PARSEC isochrones used in the previous Chapter and follows on from those results. The second model used here is a set of evolutionary tracks from MESA (see below) simulations. While evolutionary tracks are easier to derive evolution times from, isochrones represent data much similar to what can be gleaned from observations.

3.1 MIST Evolutionary Data

While PARSEC supplies isochrones covering the advanced stages of stellar evolution required in this analysis, it only provides stellar evolutionary tracks up to the TRGB and after the star reaches ZAHB. It is not uncommon for stellar evolution models to completely skip the CFP due to the high numerical complexity and vastly smaller timesteps required, compared with other evolutionary stages. For this reason, the open–source, online resource Modules for Experiments in Stellar Astrophysics (MESA; Paxton et al., 2011, 2013, 2015) was employed here. Specifically, evolution tracks of low–mass stars from the RGB through to HB or RC, were generated using MESA Isochrones and Stellar Tracks (MIST; Dotter, 2016; Choi et al., 2016). The input physics for MESA (such as EoS, opacity, diffusion, reaction rates, and boundary conditions) is organised into independent modules that generate and export data. The main advantage of this arrangement is that trialling different input physics is simple (Paxton et al., 2011).

MIST uses the one–dimensional stellar evolution package `MESA star` to produce evolutionary tracks, and from those, isochrones (detailed in Dotter (2016)). `MESA star` solves equations for the composition and fully coupled structure simultaneously (Paxton et al., 2011). MIST covers an age range of $5 \leq \log(\text{age}) \leq 10.3$, a mass range of $0.1 \leq \text{M}/\text{M}_{\odot} \leq 300$ and a metallicity range of $-2 \leq [\text{Z/H}] \leq 0.5$, from PMS to either white dwarf cooling or the end of carbon–burning, depending on stellar mass (Choi et al., 2016).

Synthetic photometry data from MIST version 1.1 were downloaded[1] in the form of stellar evolutionary tracks for this work. As with the isochrone data from PARSEC (see Chapter 2), bandpasses ACS I–band (F814W) and V–band (F555W) from the HST ACS filter set were used here. Initial ν/ν_{crit} was set to zero (rather than the default of 0.4), as PARSEC does not include rotational effects, and no extinction was implemented. Evolutionary tracks were created for each metallicity $[\text{Fe/H}] = -2, -1.6, -1, -0.6, 0, +0.4$, at mass intervals of $0.01\text{M}_{\odot}$ in the range 0.8-2 $\text{M}_{\odot}$. Currently MIST models are solar–scaled, meaning that [Fe/H]≡[M/H]. Since different solar abundance values are used in PARSEC ($\text{Z}_{\odot}$ =0.0152) and MIST ($\text{Z}_{\odot}$ =0.0142), the logarithmic values relative to solar abundances were not changed (see Section 3.1.1 for details). Stellar evolution points within each of the six age ranges (1–2, 3–4, 5–6, 7–8, 9–10 and 11–12 Gyr) were then selected for each metallicity to form 36 evolution tracks equivalent to

[1] `http://waps.cfa.harvard.edu/MIST/`, 21-10-2017

the simulations using the PARSEC ishochrones. The 0.5–1 Gyr age range was omitted in this analysis, as opposed to in Chapter 2, because low–mass stars this young would only be early–stage red giants, rather than near the onset of their CFP.

3.1.1 Comparison with PARSEC

To conduct a thorough investigation of CFP lifetimes, analysis of the stellar population simulations in Chapter 2 was combined with evolution times derived from MIST models. The PARSEC isochrones were used here to identify the proportion of the stellar population in the simulated CMDs ascending the RGB, burning quiescently on the HB, ascending the AGB, or are in the rapid stage between the HeF and ZAHB.

Choi et al. (2016) compares MIST to other commonly used models; see their Figure 15. PARSEC deviates noticeably at $\log(\text{age}) < 8.0$ for the evolutionary stages of interest here, but the effect is lessened for $\log(\text{age}) > 9.0$. This deviation for younger stars can be assumed to be due to the more complex and uncertain physics involved (such as convective core overshoot), most notably during helium–core burning (for example, McQuinn et al., 2011).

This variation between MIST and PARSEC could be due to a number of factors. Currently, MIST ignores non–solar–scaled abundances (these will be presented in later papers; see Choi et al., 2016), and uses a solar metallicity of $Z_\odot = 0.0142$ from Asplund et al. (2009), as opposed to the more recent value of $Z_\odot = 0.0152$ used in PARSEC from Caffau et al. (2011).

The two models also have different input physics, such as the values used for Reimers mass–loss (η_R=0.1 and 0.2, respectively), different opacities used for $\log(T) \lesssim 4$ (MIST uses Ferguson et al., 2005), and different models for the EoS. However, neither implement magnetic effects and both use same reaction rates from JINA REACLIB database (Cyburt et al., 2010).

Convective overshoot is also treated very differently between MIST and PARSEC. In PARSEC, Bressan et al. (2012) used the MFP of convective bubbles across the border of the convective region as the main factor in determining the overshoot, as presented in (Bressan et al., 1981). This method differs from others in that overshooting occurs at approximately 0.25 pressure scale height above the convective boundary (Meynet et al., 1994). For this technique, the overshoot parameter must depend on stellar mass, thus PARSEC employs a variable overshoot

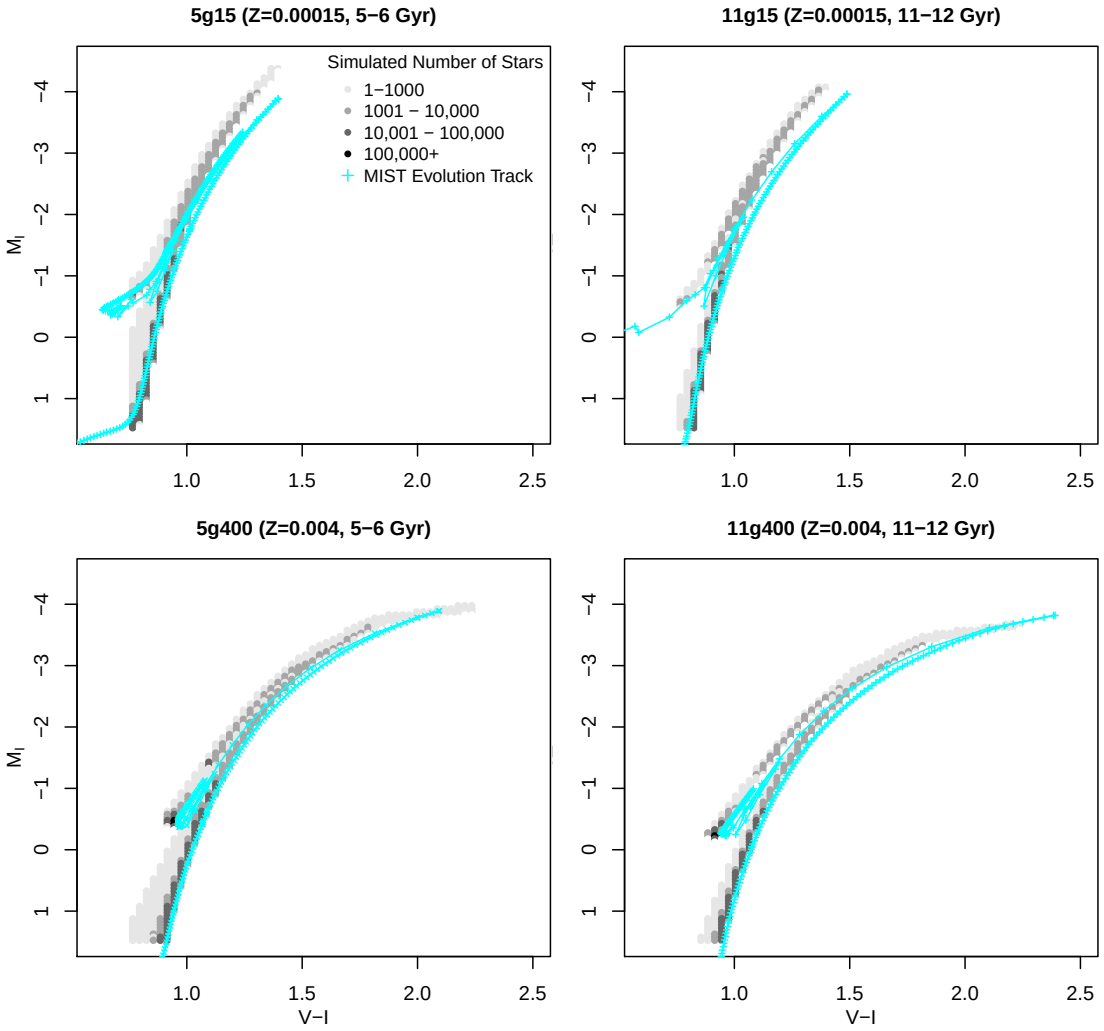

Figure 3.1: Select four simulated CMDs, with varying age and metallicity (see Chapter 2). The full 36 simulations are given in Appendix C. The legend shown in the top left plot applies to all four CMDs. These simulations are equivalent to those in Figure 2.2.

parameter.

MIST treats convective mixing as a time–dependent, diffusive process. Since MESA is one–dimensional stellar evolution code, a parametric model is used to handle convective overshoot (Paxton et al., 2011). The overshoot mixing coefficient is derived from the MLT, and also depends on the pressure scale height and an adjustable parameter (Herwig, 2000).

Efficient rotational mixing increases the size of the core and the mean molecular weight in the envelope, which in turn increases both temperature and luminosity. Rotational effects can be implemented in MIST, but are not included in PARSEC. In their investigation, Choi et al. (2016) used $\nu_{\rm ZAMS}/\nu_{\rm crit} = 0.4$ in the MIST simulations for their comparison with PARSEC isochrones (shown in their Figure 15). Figure 3.1 compares four stellar population simulations (generated using PARSEC isochrones) and the corresponding MIST evolution tracks. The Figure here shows that larger deviations between the two models occur at lower metallicities, but age appears to have less of an effect than the results from Choi et al. (2016) indicate. This is probably because Choi et al. (2016) compare PARSEC (which does not include rotational effects) to MIST tracks with rotational effects implemented. Here, MIST models were set to zero rotation to be more comparable with PARSEC. As a result, the differences between MIST and PARSEC models here are smaller than the differences presented in Choi et al. (2016).

3.2 Results

Relative stellar numbers in colour–magnitude space were simulated from PARSEC isochrones (detailed in Chapter 2). These values were used to deduce the effects of age and metallicity on the evolution of low–mass stars, focussing on immediately pre– and post–HeF. All stars evolving from the TRGB to ZAHB were visually identified on the synthetic CMDs and counted. The counts were then compared with the total number of stars present in each CMD and scaled by the 1 Gyr timespan of each simulation. The results, given in Table 3.1, show a clear trend of increasing CFP evolution time with stellar age.

Satisfactory separation of the CFP from surrounding RGB and AGB phases was only possible in simulations of older, high–metallicity stars (see Figures in Appendix C). Due to the requirement of manual inspection to isolate CFP stars,

	0.015	**0.04**
5–6 Gyr	1.4	2.0
7–8 Gyr	1.7	2.2
9–10 Gyr	1.6	2.1
11–12 Gyr	1.9	2.3

Table 3.1: Estimated evolution time (Myr) of the CFP for low–mass stars of different ages and metallicities using synthetic stellar populations generated from PARSEC isochrones. The CFP was only possible to separate from surrounding RGB and AGB phases in simulations of older, high–metallicity stars. Compare to the results from stellar population simulation results in Table 3.2. These values are plotted in Figure 3.2.

a reliable uncertainty estimate was impossible. However, it is worth noting that due to this inherent possibility of overlap from neighbouring phases, the values given in Table 3.1 are most likely an overestimate.

The TRGB and ZAHB were defined directly from the PARSEC isochrones, and applied to the stellar population simulations. The TRGB and the point at which the initial HeF occurs are indistinguishable in isochrones, since the effects from the HeF take some time to reach the stellar surface. The ZAHB was simply determined to be the point at which the colour–magnitude slope ($dI/d(V-I)$) of the locus of points in the simulation approaches zero.

Using the stellar evolution tracks available from MIST, times for the evolution from TRGB (just after the initial HeF) to ZAHB were calculated (see Table 3.2). The same trend of increasing CFP evolution time with stellar age, is also evident here.

Figure 3.2 compares the evolution times calculated from both PARSEC and MIST (Tables 3.1 and 3.2, respectively). In most cases, the results from the stellar population simulations match the calculations from MIST (within uncertainty bounds), with the tendency for the values simulated from PARSEC isochrones to be towards the slower end. This supports the prediction of overestimation due to overlapping RGB, AGB and CFP loci in colour–magnitude space. There is also a visible trend of the evolution time increasing with metallicity. However, except for the initial jump in evolution time from stars aged 1–2 Gyr to older, the evolution time does not vary significantly with age.

The uncertainties represent both the time–steps in the MIST simulations and the range of evolution times present in each stellar age group. Generally these values are greater for the younger stars (1–2 Gyr) due to there being a higher pop-

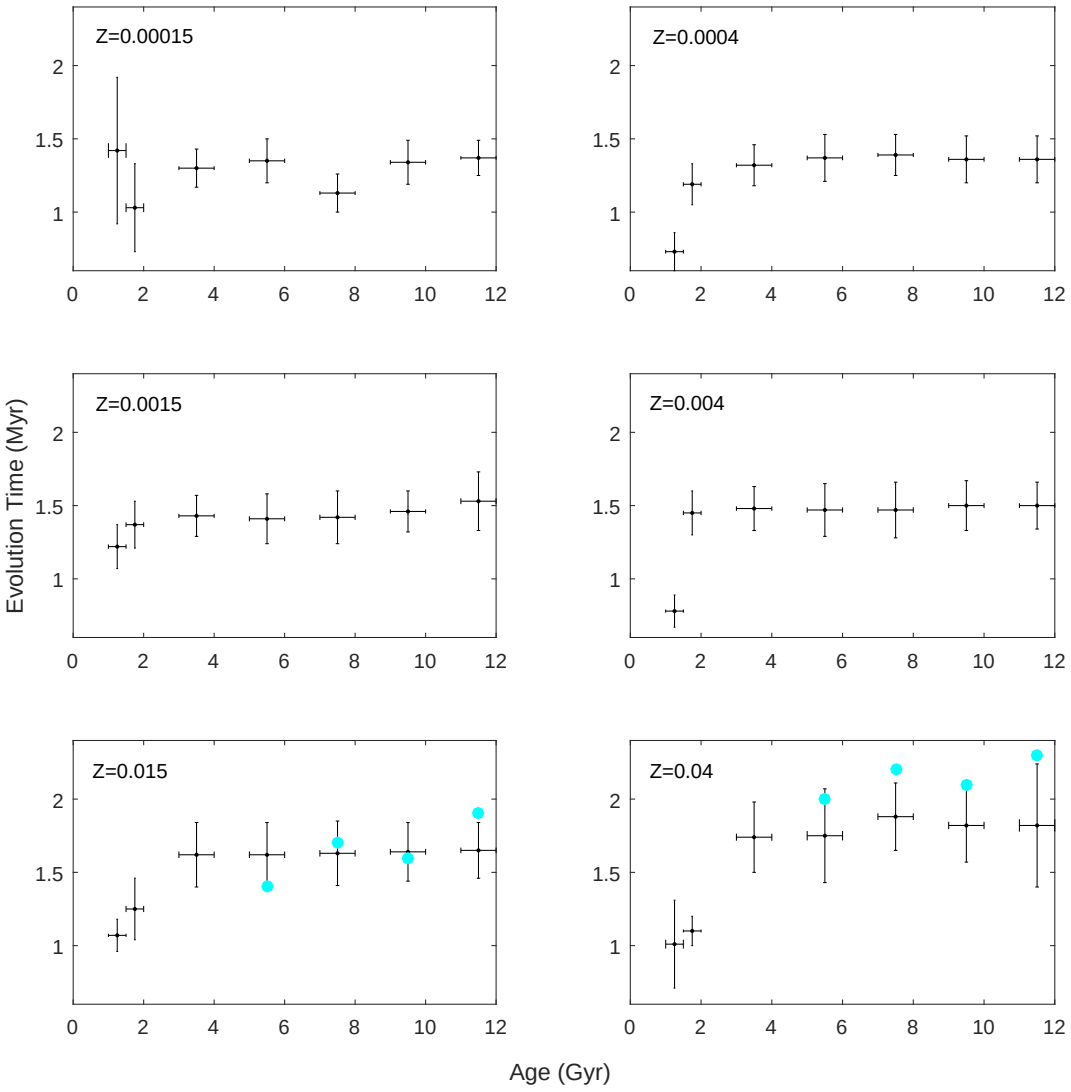

Figure 3.2: Estimated evolution time (Myr) of the CFP for low–mass stars of different ages and metallicities. The values with black errorbars were calculated from MIST evolutionary tracks, while the cyan points represent the estimates derived from the stellar population simulations. These results are given in Tables 3.1 and 3.2.

	0.00015	**0.0004**	**0.0015**
1–1.5 Gyr	1.42±1.0	0.73±0.13	1.22±0.15
1.5–2 Gyr	1.0±0.3	1.19±0.14	1.37±0.16
3–4 Gyr	1.30±0.13	1.32±0.14	1.43±0.14
5–6 Gyr	1.35±0.15	1.37±0.16	1.41±0.17
7–8 Gyr	1.1±0.3	1.39±0.14	1.42±0.18
9–10 Gyr	1.34±0.15	1.36±0.16	1.46±0.14
11–12 Gyr	1.37±0.12	1.36±0.16	1.53±0.20
	0.004	**0.015**	**0.04**
1–1.5 Gyr	0.78±0.11	1.07±0.11	1.0±0.3
1.5–2 Gyr	1.45±0.15	1.25±0.21	1.1±0.1
3–4 Gyr	1.48±0.15	1.62±0.22	1.74±0.24
5–6 Gyr	1.47±0.18	*1.62±0.22*	*1.75±0.32*
7–8 Gyr	1.47±0.19	*1.63±0.22*	*1.88±0.23*
9–10 Gyr	1.50±0.17	*1.64±0.20*	*1.82±0.25*
11–12 Gyr	1.50±0.16	*1.65±0.19*	*1.82±0.42*

Table 3.2: Estimated evolution time (Myr) of the CFP for low–mass stars of different ages and metallicities using MIST simulations. The values italics can be compared to the results from the stellar population simulation results in Table 3.1. These values are plotted in Figure 3.2.

ulation in this age range, hence a larger range of evolution times. For this reason, the younger stars were split into two groups: 1–1.5 and 1.5–2 Gyr. Interpolation was used to determine the evolution times where the mass steps of 0.01 $M_\odot$ were too coarse to resolve the tracks, or to smooth outliers. This problem was mainly limited to metallicity Z=0.04, hence the larger uncertainties quoted in Table 3.2 for these tracks.

Serenelli et al. (2017) noted that due to the relationship between the bolometric correction and effective temperature, helium ignition does not always occur at the TRGB in $M_I-(V-I)$ space, especially at high metallicities. The simulated CMDs and the MIST models in Appendix C show that the RGB did tend to flatten out towards the tip at high metallicities.

Unlike when using the PARSEC data, the HeF, TRGB and ZAHB for the MIST simulations could be determined through evolution calculations, rather than morphology. The evolutionary time between the onset of the CFP and the observable TRGB, is shown in Table 3.3. The ZAHB was defined by the point at which helium–burning has stabilised; specifically, the change in luminosity due to helium–burning across three time–steps of the evolutionary track

	0.00015	**0.0004**	**0.0015**	**0.004**	**0.015**	**0.04**
1–1.5 Gyr	0.14	0.24	0.20	0.17	0.15	0.16
1.5–2 Gyr	0.26	0.23	0.20	0.18	0.17	0.12
3–4 Gyr	0.23	0.21	0.19	0.18	0.16	0.14
5–6 Gyr	0.22	0.20	0.19	0.18	0.16	0.15
7–8 Gyr	0.21	0.20	0.19	0.18	0.17	0.15
9–10 Gyr	0.21	0.20	0.19	0.18	0.17	
11–12 Gyr	0.21	0.20	0.36	0.18	0.17	

Table 3.3: Evolution time (Myr) between the onset of the CFP and the observable TRGB, according to MIST simulations. The equivalent values are not available for PARSEC data since the evolutionary tracks between TRGB and ZAHB are not simulated.

$\Delta\log(L_{He}/L_{\odot}) \leq 0.05$.

However, given that the TRGB and the onset of helium ignition cannot be separated in the case of the PARSEC isochrones, there is added uncertainty in the CFP lifetimes reported in Table 3.1. If the time differences displayed in Table 3.3 for the MIST models are accepted as applicable, this would add uncertainties of $7 - 12\%$.

3.2.1 Mass Bias

Figure 2.1 shows how bias can be introduced by restricting an observation sample based on colour and magnitude, because the number of red giants depends on the average red giant mass, as well as the mass range on the RGB. Using the evolutionary tracks from MIST, the stellar mass ranges present in each age–metallicity pair are shown in Table 3.4. The wide range of masses present in younger stars across all metallicities tested here, further demonstrates the need to carefully consider the shape of the IMF and stellar evolutionary lifetime effects, to avoid biasing samples towards younger stars, as discussed in Chapter 2.

3.2.2 Red Giant Branch Tip

Determining the position of the initial HeF in colour–magnitude space may help identify those stars that are immediately pre– and post–HeF, in order to monitor them and possibly observe a HeF occurring for the first time. In a similar procedure to that outlined above, the TRGB was identified directly from the PARSEC isochrones as the brightest, most red–ward point on the RGB. The results are

	0.00015	**0.0004**	**0.0015**
1–1.5 Gyr	1.5–1.72	1.5–1.72	1.58–1.72
1.5–2 Gyr	1.38–1.5	1.38–1.5	1.48–1.58
3–4 Gyr	1.18–1.22	1.18–1.22	1.18–1.22
5–6 Gyr	0.98–1.02	0.98–1.02	1.04–1.06
7–8 Gyr	0.9–0.94	0.92–0.94	0.94–0.96
9–10 Gyr	0.84–0.86	0.84–0.86	0.89–0.91
11–12 Gyr	0.8–0.82	0.81–0.83	0.84–0.86
	0.004	**0.015**	**0.04**
1–1.5 Gyr	1.62–1.8	1.8–2	1.95–2
1.5–2 Gyr	1.5–1.62	1.66-1.8	1.85–1.95
3–4 Gyr	1.2–1.3	1.38–1.42	1.47–1.49
5–6 Gyr	1.08–1.12	1.2–1.24	1.31–1.33
7–8 Gyr	0.98–1.02	1.12–1.14	1.2–1.22
9–10 Gyr	0.92–0.94	1.04–1.06	
11–12 Gyr	0.86–0.88	0.98–1	

Table 3.4: Approximate mass ranges ($M_\odot$) present in MIST evolutionary tracks at each age and metallicity.

plotted in Figure 3.3 (data in Table D), with different colour scales across each subplot. Figure 3.3 also shows the results from MIST simulations (Table D).

The RGB is located more redward with increasing age, as expected. Additionally, for a given age, higher metallicities also push the RGB more redward. There is a clear trend across higher metallicities (Z=0.004, 0.015, 0.04), where the brightness significantly decreases with increasing age, and for a given age, generally the brightness decreases as the metallicity increases. Lower metallicities vary less with age: most of the points clustered between $0.9 < V - I < 1.9$, and all but the youngest stars brighter than ~ -3.5.

In most cases, the errorbars in Figure 3.3 representing the uncertainties, are quite small. The uncertainties are greater for the younger stars (1–2 Gyr) due to there being many more stars in this age range, and therefore a larger range of evolution times and TRGB colour–magnitude coordinates. For this reason, there was a large difference between PARSEC isochrones at 1 Gyr and those for stars aged 2 Gyr, thus these age isochrones were considered separately. The younger stars behave very differently to all other ages presented here (see Appendix C).

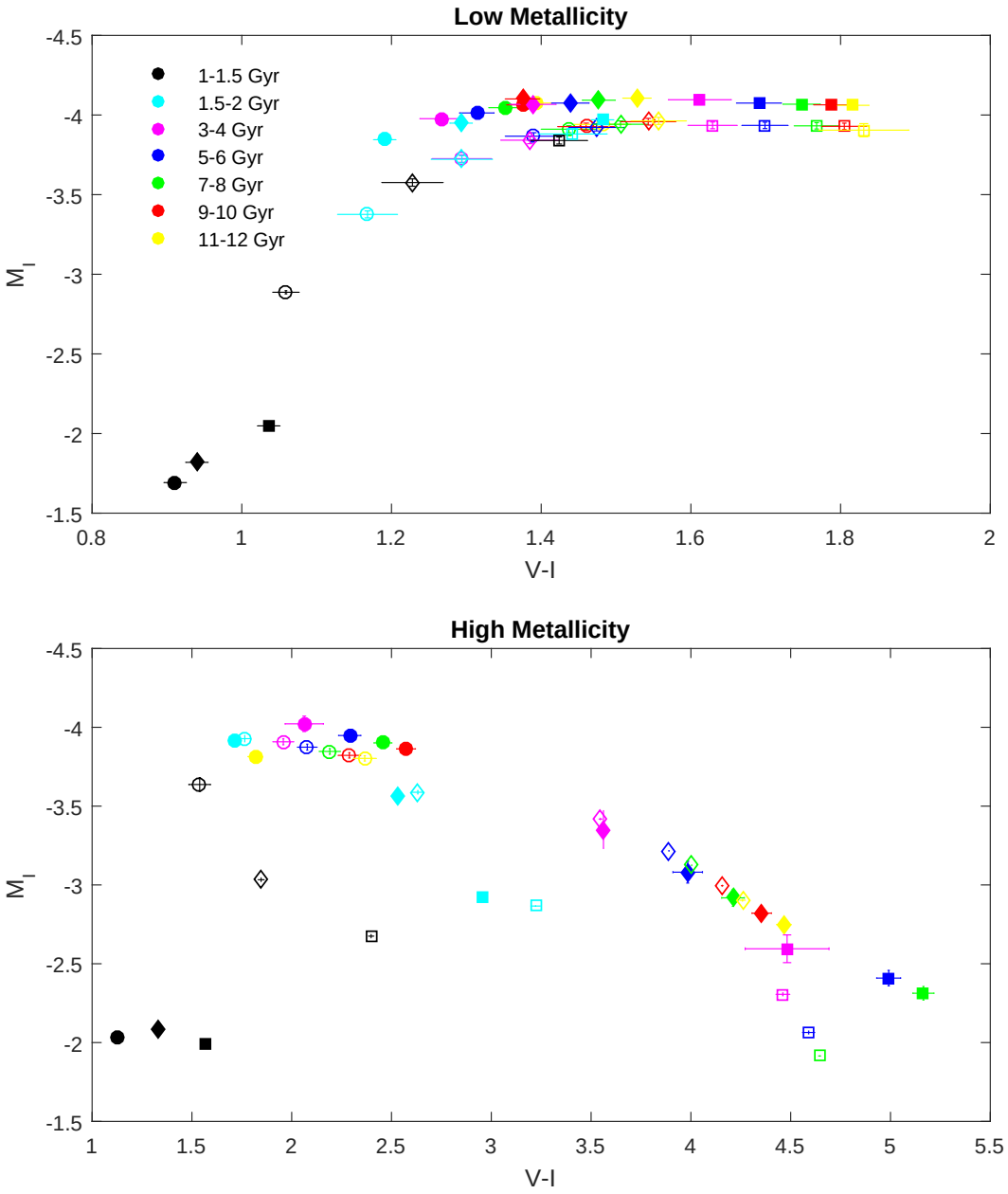

Figure 3.3: Estimated location of the TRGB in colour–magnitude space as determined by PARSEC isochrones and MIST evolution tracks, for each age range and metallicity. The six metallicities have been split into two groups to aid comparison; low–metallicity (0.00015 - circles, 0.0004 - diamonds, 0.0015 - squares) in the top panel and high–metallicity (0.004 - circles, 0.015 - diamonds, 0.04 - squares) in the bottom panel. Note the different colour scales across each axis. The filled points are from PARSEC while the open points are from MIST. Each has errorbars corresponding to the uncertainties in calculations and the range of values calculated. The data for these are given in Tables D and D.

	0.00015	**0.0004**
1 Gyr	(0.911,-1.692)±(0.015,0.025)	(0.940,-1.819)±(0.015,0.025)
2 Gyr	(1.191,-3.845)±(0.015,0.025)	(1.293,-3.949)±(0.015,0.025)
3–4 Gyr	(1.267,-3.977)±(0.029,0.031)	(1.389,-4.067)±(0.031,0.026)
5–6 Gyr	(1.314,-4.013)±(0.023,0.034)	(1.439,-4.075)±(0.025,0.029)
7–8 Gyr	(1.351,-4.046)±(0.021,0.030)	(1.477,-4.093)±(0.022,0.028)
9–10 Gyr	(1.375,-4.064)±(0.021,0.029)	(1.375,-4.101)±(0.023,0.027)
11–12 Gyr	(1.394,-4.075)±(0.019,0.027)	(1.528,-4.106)±(0.019,0.026)
	0.0015	**0.004**
1 Gyr	(1.036,-2.048)±(0.015,0.025)	(1.127,-2.031)±(0.015,0.025)
2 Gyr	(1.482,-3.970)±(0.015,0.025)	(1.717,-3.919)±(0.015,0.025)
3–4 Gyr	(1.612,-4.096)±(0.042,0.031)	(2.063,-4.022)±(0.096,0.049)
5–6 Gyr	(1.691,-4.075)±(0.030,0.027)	(2.291,-3.948)±(0.056,0.037)
7–8 Gyr	(1.748,-4.068)±(0.025,0.026)	(2.457,-3.901)±(0.045,0.033)
9–10 Gyr	(1.788,-4.064)±(0.024,0.026)	(2.573,-3.863)±(0.047,0.039)
11–12 Gyr	(1.817,-4.061)±(0.021,0.026)	(1.817,-3.814)±(0.036,0.035)
	0.015	**0.04**
1 Gyr	(1.334,-2.086)±(0.015,0.025)	(1.566,-1.994)±(0.015,0.025)
2 Gyr	(2.529,-3.567)±(0.015,0.025)	(2.953,-2.918)±(0.015,0.025)
3–4 Gyr	(3.56,-3.35)±(0.20,0.12)	(4.48,-2.595)±(0.21,0.088)
5–6 Gyr	(3.984,-3.081)±(0.074,0.069)	(4.991,-2.409)±(0.060,0.049)
7–8 Gyr	(4.211,-2.918)±(0.057,0.054)	(5.165,-2.313)±(0.053,0.043)
9–10 Gyr	(4.355,-2.821)±(0.049,0.048)	(5.301,-2.247)±(0.049,0.041)
11–12 Gyr	(4.466,-2.749)±(0.036,0.039)	(5.414,-2.200)±(0.037,0.031)

Table 3.5: Colour–magnitude coordinates of the TRGB derived from PARSEC isochrones. Due to the large difference between 1 and 2 Gyr values, these have been split into separate groups. These data are plotted in Figure 3.3.

	0.00015	**0.0004**
1–1.5 Gyr	(1.059,-2.887)±(0.018,0.010)	(1.228,-3.576)±(0.041,0.023)
1.5–2 Gyr	(1.168,-3.376)±(0.040,0.022)	(1.294,-3.722)±(0.041,0.023)
3–4 Gyr	(1.294,-3.726)±(0.040,0.023)	(1.385,-3.842)±(0.039,0.022)
5–6 Gyr	(1.390,-3.867)±(0.038,0.022)	(1.474,-3.922)±(0.037,0.022)
7–8 Gyr	(1.437,-3.911)±(0.037,0.022)	(1.506,-3.942)±(0.037,0.021)
9–10 Gyr	(1.460,-3.927)±(0.038,0.022)	(1.543,-3.958)±(0.037,0.021)
11–12 Gyr	(1.482,-3.941)±(0.038,0.022)	(1.557,-3.963)±(0.037,0.022)
	0.0015	**0.004**
1–1.5 Gyr	(1.424,-3.840)±(0.038,0.022)	(1.539,-3.637)±(0.054,0.044)
1.5–2 Gyr	(1.442,-3.881)±(0.046,0.031)	(1.765,-3.928)±(0.027,0.020)
3–4 Gyr	(1.628,-3.935)±(0.033,0.021)	(1.958,-3.908)±(0.053,0.019)
5–6 Gyr	(1.699,-3.935)±(0.031,0.020)	(2.078,-3.874)±(0.050,0.019)
7–8 Gyr	(1.768,-3.932)±(0.030,0.020)	(2.191,-3.847)±(0.054,0.018)
9–10 Gyr	(1.805,-3.929)±(0.030,0.020)	(2.289,-3.822)±(0.057,0.017)
11–12 Gyr	(1.831,-3.905)±(0.060,0.041)	(2.366,-3.803)±(0.059,0.017)
	0.015	**0.04**
1–1.5 Gyr	(1.847,-3.033)±(0.016,0.012)	(2.398,-2.675)±(0.014,0.011)
1.5–2 Gyr	(2.632,-3.588)±(0.030,0.011)	(3.222,-2.866)±(0.026,0.001)
3–4 Gyr	(3.547,-3.418)±(0.009,0.006)	(4.461,-2.306)±(0.036,0.009)
5–6 Gyr	(3.890,-3.216)±(0.004,0.001)	(4.590,-2.064)±(0.032,0.009)
7–8 Gyr	(4.004,-3.125)±(0.003,0.002)	(4.645,-1.915)±(0.007,0.002)
9–10 Gyr	(4.157,-2.995)±(0.006,0.005)	*5.188,-1.779*
11–12 Gyr	(4.259,-2.903)±(0.015,0.007)	*5.412,-1.677*

Table 3.6: Colour–magnitude coordinates of the TRGB derived from MIST evolution tracks. Due to the large difference between 1 and 2 Gyr values, these have been split into separate groups. These data are plotted in Figure 3.3. Mass steps of 0.01 $M_{\odot}$ were not sufficient to resolve evolution tracks for the oldest stars at Z=0.04 (shown in italics); the values given were interpolated.

3.3 Discussion

Comparing the number of stars populating each region of simulated CMDs allowed for the calculation of approximate evolutionary rates of the CFP for different ages and metallicities. This was combined with data from stellar evolutionary tracks to improve estimates. The clear trend in evolution rates (Figure 3.2) is that longer times are associated with higher metallicities, most likely due to the associated increased opacity (see Chapter 1). With the exception of younger stars (1–2 Gyr) evolving quicker across all metallicities, the evolution rates do not vary significantly with age. This is advantageous due to the fact that age can be difficult to determine and cannot be measured directly like metallicity, for example.

Battich et al. (2018) modelled hot pre–HB stars through their CFP, exploring a range of compositions and helium–core masses at the TRGB by artificially removing different portions of the envelope at this point. The mechanism behind the mass loss is irrelevant, only the mass at helium ignition is of any consequence. Battich et al. (2018) found that for higher metallicities (and helium abundances), there is a lower number of subflashes following the main HeF event due to the lower helium–core mass at helium ignition, leading to a lower level of degeneracy. However, their modelled CFP occurred over roughly 2 Myr in all cases. The agreement between the two different models analysed here in Figure 3.2, indicates that contrary to previous assumptions (Thomas, 1967; Serenelli & Weiss, 2005; Bildsten et al., 2012), the metallicity does play a role in determining the CFP lifetime. These results suggest that evolution rates through the CFP are longer in higher metallicity stars. While a lower degree of degeneracy will take less energy to lift, that energy is expected to take longer to radiate from the nuclear–burning region.

The CFP lifetimes derived here are in good agreement with previous results. Models by Sweigart (1994) suggest an evolution time for the CFP of $\sim 10^6 - 10^7$yr, a range which encompasses almost all of the values calculated here. More specifically, Despain (1981) reports a time of ∼1.7 Myr for a star of mass 0.6 $M_\odot$ and Z=0.001, while Brown et al. (2001) calculated an evolution time of ∼2 Myr for a star at age 13 Gyr with Z=0.0015. The trend here (Table 3.2) predicts a CFP lifetime of ∼1.6 Myr. Also using MESA data, Paxton et al. (2011) modelled stars of masses 0.9–1.5 $M_\odot$ at Z=0.01, 0.02, calculating an evolution time for this stage to be ∼2 Myr. The calculations made here using MIST evolutionary tracks sug-

gest a value of ∼1.6 Myr, while the calculations using PARSEC isochrones give a range of 1.4–1.9 Myr. Silva Aguirre et al. (2008) however reports a much shorter CFP lifetime of ∼1.12–1.4 Myr for a star 13 Gyr old, with Serenelli & Weiss (2005) reporting 1.325 Myr for Z=0.0001, both using GARSTEC simulations (see Chapter 1 for details on GARSTEC).

As described in Chapter 1, after the initial HeF, the rapid contraction of the red giant envelope greatly increases coupling between the p-modes to the g-modes in the core. Research by Bildsten et al. (2012) shows that during their CFP, stars occupy an underpopulated region of $\Delta\nu - \Delta P_g$ space, allowing them to be isolated from other red giants.

The results presented here on TRGB colour–magnitude coordinates and CFP evolutionary rates, as functions of age (mass) and metallicity, could guide expectations regarding the type of HeF star most likely to be detectable. Higher metallicity populations of intermediate–age to old red giants will spend the most time in their CFP and so should be form the basis of future observational searches. Combining the criteria derived here and those presented in Bildsten et al. (2012), will allow for highly targeted asteroseismology observations in the future, with the aim of presenting the first observational evidence of the HeF or the subsequent subflashes.

3.3.1 Future Efforts

The format of these results allows for ease of implementation in future analysis that may include additional complexities, such as magnetic and rotational effects, or the conversion to an alternate solar–scaled metallicity. The ratios between the evolutionary rates and CMD coordinates as derived here could be scaled directly if the magnitude of additional effects is known.

In order to apply these evolution rates to a realistic population of stars, the stellar age distribution needs to be roughly known. Ideally this approach should be applied to combined CMDs and chemical abundance data. While these simulations eliminate/alleviate some degree of the bias present in observed metallicity distributions, there is one main potential source for inaccuracy in this analysis: manually determining which stars are evolving between TRGB and ZAHB in the population distribution simulations. The separation between the AGB and RGB is less pronounced at younger age ranges (1–2 Gyr), but at higher metallicities, the older stars on the AGB over–lapped the younger RGB stars for each age limit

(see Appendix C for CMDs of the simulations), making isolating the post–TRGB stars more difficult. Relations between the fraction of stars in this phase, and the age and metallicity were used to determine the evolutionary rates for the cases where manual inspection was impossible. For future efforts, more sophisticated techniques should be developed to isolate the post–TRGB stars.

As explained in Chapter 1, the evolution during the CFP is generally accepted to be hydrostatic (see, for example Thomas, 1967; Deupree, 1996; Serenelli & Weiss, 2005; Paxton et al., 2011). Because hydrostatic evolution is also expected during the star's ascent of the RGB, the star will closely follow the RGB back down as it evolves towards the HB. Chapter 4 aims to identify possible pre– and post–HeF candidates from observations of variable stars. This expected overlap of RGB and CFP stars' locations in colour–magnitude space is a complication that must be considered in any search for observational evidence of this rare stellar population. Since metallicity affects the colour of a star during this stage, only metal–poor stars will be sufficiently blue to cross the instability strip, immediately before they reach ZAHB. Compounding this, intermediate–age stars will also be too red to cross through. These factors are explored in the following Chapter with the aim of identifying possible HeF candidates in the variable star population of the Small Magellanic Cloud.

Chapter 4

Variable Stars

Variable stars experience changes in their luminosity over time, due to either internal driving forces or external influences. These two conditions define the variability classes. Extrinsic variables include stars which are part of an eclipsing binary system; while eruptive, cataclysmic, rotational, and pulsating variables are all a result of intrinsic factors. Variable stars are also broadly classified into three types according to their light curve shape: regular, semi–regular and irregular. Intuitively, regular variables having a repeating pattern over a constant periodicity, while irregular variables fluctuate seemingly at random. Semi–regular variable stars lie somewhere between these two cases.

Intrinsically varying stars can be a very important tool in the quest to understand the nature of stellar interiors and how they evolve. As outlined in Chapter 1, a star undergoing a core helium–flash (HeF) could possibly be identified as a pulsating variable star with large changes in its period. The period–mean density relation (Equation 1.13 Ritter, 1879) states that the period of a pulsating star depends on the luminosity and radius, both of which are changing on very rapid timescales during the HeF (on the order of hours up to 10^4 yr during the initial flash Paxton et al., 2011; Bildsten et al., 2012), when compared to surrounding variable stars. In this way, the identification problem of core–flash phase (CFP) candidates sharing the same loci on the HRD as the RGB, AGB and HB, may be avoided.

As the post–cor–flash star evolves to a lower luminosity and higher effective temperature, it may pass through the Cepheid instability strip before settling into hydrostatic equilibrium on the horizontal branch. RR Lyrae and Type II Cepheids variables are old, low–mass, regular variables whose periods

and light curve shapes are highly sensitive to the internal structure of the star. Thus, they may offer a way to observationally probe the rare population of stars during the CFP. Although stellar evolution occurs on a thermal and not a nuclear timescale after the HeF, total brightness changes might still take decades or centuries to observe. The high photometric sensitivity required to detect these evolutionary changes is very difficult to achieve. However, very small period changes can be observed with regular sampling over a shorter timescale, while avoiding the demand for such high sensitivity.

RR Lyrae Variables

RR Lyrae stars vary radially via pressure waves travelling from the centre to the surface and back (Hansen et al., 2004), with periods of 0.2–1.0 days and are located on the HRD where the pulsation instability strip intersects the HB. Only certain stellar ages and metallicities have sufficiently extended HBs that they cross the instability, namely metal–poor, old stars (see Chapter 2). They are divided into subsets according to their pulsation modes; the fundamental mode RRab (sometimes called RR0), the first–overtone RRc or RR1, and double–mode RRd or RR01. Originally, RR Lyrae variables were subdivided into types RRa, RRb, and RRc by Bailey (1902), based on the amplitude and shape of their light curves. Later it was discovered that RRc–type oscillate in a different mode to RRa and RRb, thus the latter were merged into one group - RRab. There is controversy over the existence of RR Lyrae second–overtone pulsators (RRe; see Kovács, 1998; Clement et al., 2001), exploration of which is beyond the scope of this research. Using data from the Wide–field Infrared Survey Explorer (WISE), Gavrilchenko et al. (2014) found it sufficiently difficult to distinguish between RRc stars and those classified as RRe, that the authors amalgamated them into one category. Coupled with the fact that this class of RR Lyrae are rare (Soszyński et al., 2009), the RRe type were simply excluded from this analysis.

High period change rates for RR Lyrae stars are generally considered to be $|\dot{P}| \gtrsim 0.1 - 0.5$ d/Myr (see, for example Sweigart & Renzini, 1979; Koopmann et al., 1994; Kunder et al., 2011), and have been observed among field and cluster stars (Smith, 1995). Canonical stellar evolution theory gives the typical absolute period change rate of RR Lyrae stars to be less than ~ 0.1 d/Myr (equivalent to $\sim 3 \times 10^{-10}$ d/d; see Lee, 1991; Smith, 2013). Higher values of $|\dot{P}|$ tend to occur only when stars near the end of their HB phase and start their ascent of the

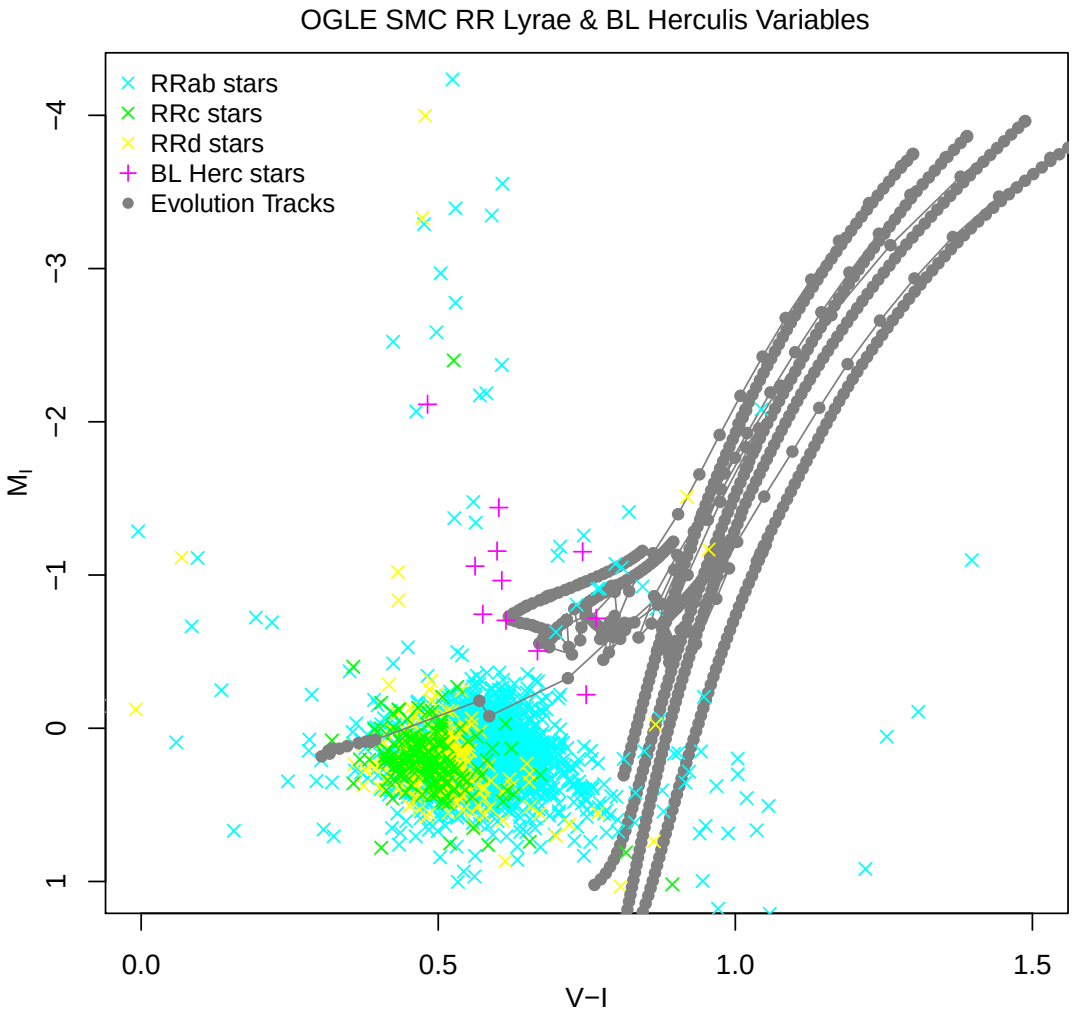

Figure 4.1: The complete sample of Small Magellanic Cloud (SMC) RR Lyrae and BL Herculis variables used in this analysis (see Section 4.2.1 below), plotted along with intermediate–age to old, low–metallicity stellar MIST evolutionary data (recall Chapter 3; see also Paxton et al., 2011), showing the RGB and HB phases (in grey). The RRab stars are marked in cyan, the RRc in green, and the RRd in yellow. The BL Herculis variables are shown in magenta. Only the oldest, most metal–poor stars fully cross the instability strip. The apparent magnitudes provided in the data were converted to absolute magnitudes based on the distance modulus of 18.95 ± 0.07 calculated by Graczyk et al. (2014).

AGB. However, large negative period changes should only occur in stars during the CFP, or during short periods of unstable structural changes such as mixing events (Sweigart & Renzini, 1979; Koopmann et al., 1994; Silva Aguirre et al., 2008). Thus, detection of such period change rates was the primary aim here.

Type II Cepheid Variables

Type II Cepheids variables lie above RR Lyrae stars in the instability strip and are generally thought to have periods ranging from about 1-25 days. However, studies by Clement et al. (2001) and Gautschy & Saio (1996) both propose the lower limit to be ∼0.8 days. This overlaps marginally with the upper limit for RR Lyrae periods, leading to difficulty distinguishing between them. Catelan & Smith (2015) suggest identifying the RR Lyrae with stars in the core helium–burning stage, and Type II Cepheids with stars in the later, shell helium–burning phase, but these can be difficult to separate observationally. Similarly, distinguishing between the short period BL Herculis Type II Cepheids stars and the longer period W Virginis stars can be blurry when relying on the period–luminosity relation to categorise them (see, for example Matsunaga et al., 2011). The Optical Gravitational Lensing Experiment (OGLE; Udalski et al., 2008a, also see Section 4.2.1) uses periods of 1 d to be the cutoff between RR Lyrae and BL Herculis stars, 4 d for the cutoff between BL Herculis and W Virginis in the Magellanic Clouds and 5 d for the Galactic Bulge. Since OGLE data is used in this analysis, those definitions were adopted here.

Type II Cepheids with masses of ∼0.52–0.53 $M_\odot$ may cross the instability strip several times during thermal pulses (see Chapter 1 for details), evolving along blue–ward loops over 0.7–1.5 Myr. Meanwhile, Type II Cepheids with masses ∼0.55–0.59 $M_\odot$ are expected to cross the instability strip from blue to red over 1–2 Myr. If these evolution calculations from Bono et al. (1997) are correct, W Virginis stars are low–mass stars evolving along blue loops, crossing the instability strip, and so could undergo either period increases or decreases, depending on where they are on their evolution track (see, for example Percy & Hale, 1998; Percy & Hoss, 2000; Berdnikov et al., 2007; Templeton & Henden, 2007; Rabidoux et al., 2010). BL Herculis variables are predicted to be stars evolving towards the AGB and would experience positive period change rates of up to about 20 d/Myr (see discussions in Smith, 2013; Catelan & Smith, 2015).

As stellar evolution theory predicts both large increases and decreases in the

periods of W Virginis stars in other stages of evolution (see Bono et al., 1997; Catelan & Smith, 2015), they were not considered for HeF candidates here. For this reason, RV Tauri stars were also omitted. Thus, the total sample analysed here includes RRab, RRc, RRd and BL Herculis stars, as available in OGLE–III. These are plotted in Figure 4.1, alongside PARSEC isochrones with ages and metallicities representative of the SMC's metal–poor population, where the average metallicity is Z$\approx$ 0.0015 and the distribution tails off towards lower values (Dobbie et al., 2014). The Figure shows that a significant proportion of the analysed variable stars overlap with a low–mass star's pre-ZAHB evolution, but predominantly with the old isochrones. Thus, the oldest, most metal–poor stars are the best candidates for crossing the HB. Unfortunately, the majority of stars in the SMC are intermediate–age. The limitations of this are discussed later in this Chapter.

Results from the previous Chapter demonstrate that stars in the CFP are likely to be evolving quickly back down the giant branch following the initial HeF, but slowing as they approach the HB. While the most rapidly evolving stars will display the highest rate of period change, they are also hardest to identify since post–HeF stars have the highest probability of being located towards the ZAHB (indicated in Figure 4.1).

4.1 Calculating Periodicity

In astronomy, observations often cannot be made at evenly–spaced intervals, which makes determining the period of an object complex. Conversely, an advantage of having unevenly–sampled data is that measurements can be taken less often than the Nyquist frequency. There have been many past astronomical studies attempting to detect periodicity in such situations, using both parametric and non–parametric methods (see Broersen et al., 2000; Graham et al., 2013; VanderPlas, 2018, and references therein).

There are broadly four different types of methods for frequency analysis on an unevenly sampled timeseries: model–based, phase–folding, interpolation, and direct transform. As the name suggests, model–based methods fit a model to the timeseries, but unlike the other techniques listed here, require prior knowledge about the behaviour of the source (see Harteveld et al., 2005, and references therein).

Phase–folding, or slotting methods, bin the data in the phase domain to de-

termine the correlation function based only on the points which deviate from the expected value by less than half a bin width (Stellingwerf, 1978; Edelson & Krolik, 1988; Mayo, 1978). Techniques based on this principle are often used in astronomy (Böttcher & Dermer, 2010; Fan et al., 2010; Nieppola et al., 2009; Zhang et al., 2010). It is worth noting that phase–folding methods can produce correlation function estimates that are neither finite nor positive. To combat this, different weighting methods have been trialled based on sinc kernels (Stoica et al., 2009), and Gaussian and Laplacian kernels (Babu & Stoica, 2010). Other methods exist for producing positive finite correction estimates, but these result in a loss of information as they do not use all available data (Mudelsee, 2013).

Timeseries reconstruction methods use interpolation to resample the "missing" data to form an evenly–spaced timeseries, which can then be analysed using standard techniques. Common interpolation methods, when used towards this end, result in significantly lower accuracy of the estimated power spectrum at the higher end of the frequency range (Schulz & Stattegger, 1997). Meaning that for a smaller period (such as that of an RR Lyrae variable), much of the crucial phase information may be lost or warped. For this reason, these methods should be avoided, especially when looking at short–term variations (compared with the average sampling interval).

In comparison, direct transform methods can be applied to the raw data. The Lomb–Scargle Periodogram (LSP; Lomb, 1976; Scargle, 1982) is the most commonly used direct transform method in astronomy to determine periodicity in unevenly–sampled observations. A periodogram provides a measure of the relative power (likelihood) of a particular timeseries representing the data, as a function of frequency (see Section 4.1.1 for more details), and can be derived from Bayesian probability theory (Jaynes, 1987; Bretthorst, 1988). It is worth noting that according to Bayesian probability theory, utilising least–squares in a periodogram model is the most accurate method for identifying a sinusoidal periodic signal in Gaussian noise (Jaynes & Bretthorst, 2003). The Lomb–Scargle method also shares similarities with bin–based phase–folding techniques in some situations (Swingler, 1989), and so it has advantages of all these techniques. For a full discussion on this subject, see Zechmeister & Kürster (2009).

Here, LSP analysis is used because of its ability to incorporate measurement uncertainties, and directly use unevenly sampled data without requiring any form of interpolation. Due to it being such a common tool in astronomy, there is also much literature available on the subject, and free programs for its implementation.

Its relation to Bayesian probability and least–squares statistics make it useful in a wide range of situations, as well as provide an alternate insight into internal calculations.

4.1.1 Lomb–Scargle Periodograms

A periodogram presents numerous peaks of differing heights and widths across the range of trialled frequencies (see Figure 4.2; Schuster, 1898; Barning, 1963). The highest peak is reported as the actual frequency of the source. The LSP algorithm is a Fourier–transform method, converting data in the time domain to frequency space. Lomb (1976) and Scargle (1982) earned the naming rights of the LSP algorithm by making significant improvements to previous definitions of the normalised periodogram. These authors eliminated the requirement of evenly sampled data, and also removed the dependence of the calculated spectral power on translations in time by introducing a time–offset (see Press et al., 2007).

The LSP algorithm fits a sinusoidal function to the data at each pre–specified frequency f:

$$y(t; f) = A_f \sin(2\pi f(t - \phi_f)), \tag{4.1}$$

where y is the magnitude of the light observed at a particular time (t), and A_f and ϕ_f are both functions of the trialled frequencies. To determine the periodicity from a set of observations, a Fourier series is constructed at each pre–specified frequency. The goodness–of–fit for each frequency is reported as a significance measure between zero and one.

As mentioned above, the Fourier analysis behind the LSP can also be considered in terms of a least–squares method. The sinusoidal model constructed at each candidate frequency has a corresponding $\chi^2(f)$ statistic, the minimisation of which leads to the optimisation of the model's parameters (see Lomb, 1976; VanderPlas, 2018):

$$\chi^2(f) \equiv \sum_n \left(\frac{y_n - y(t_n; f)}{\sigma_n} \right)^2. \tag{4.2}$$

However, like all least–squares methods, the LSP is not well–equipped to deal with outliers (illustrated in Schimmel, 2001). Additionally, because the underlying model of the LSP is non–linear, in general the periodogram contains many local maxima in addition to the peak at the true frequency (see Figure 4.2; also

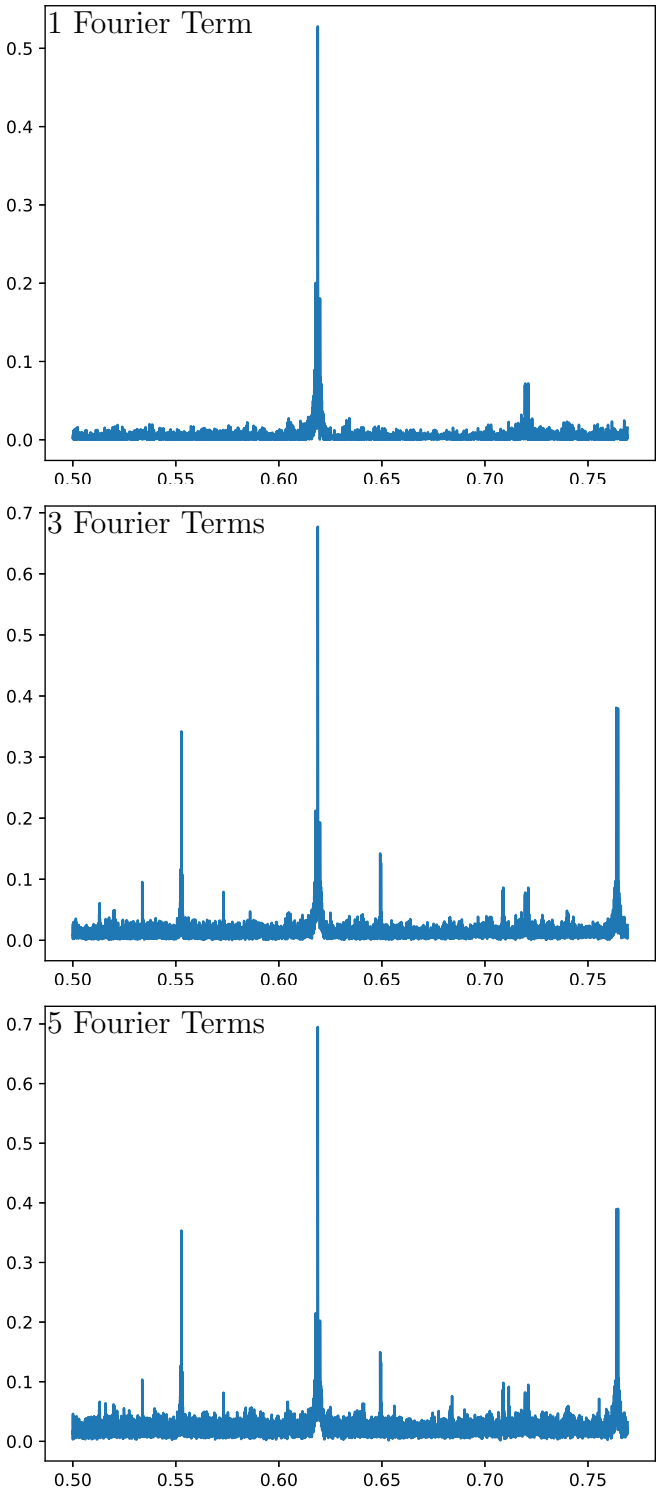

Figure 4.2: Periodograms produced using the Lomb–Scargle analysis with one, three, and five Fourier terms (see Section 4.1.1), showing the significance (peak height), and accuracy (peak width) at each trialled period value. The highest peak is selected as the "true" period. The source is RR Lyrae OGLE-LMC-RRLYR-10752 from the OGLE database.

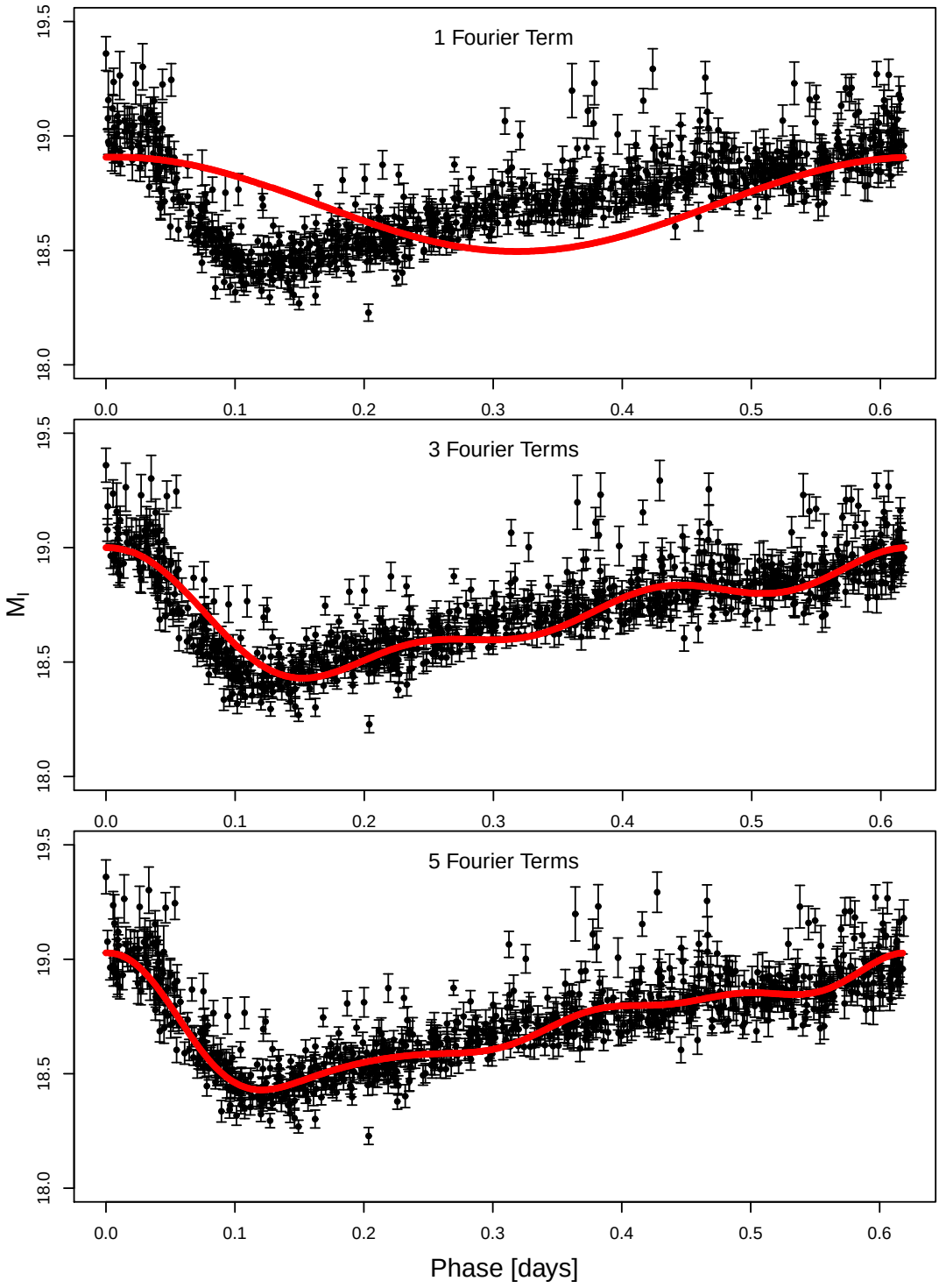

Figure 4.3: Phase plots of observations (black points), and the light curve as determined by Lomb–Scargle analysis with one, three and five Fourier terms (red line). The source is RR Lyrae OGLE–LMC–RRLYR–10752 from the OGLE database.

VanderPlas & Ivezić, 2015; VanderPlas, 2018, for discussions). In some cases when the peak heights are comparable, it can be difficult to correctly isolate the true period. Furthermore, if there is significant scatter present in a phase plot of the light curve (see Figure 4.3), this could mean that the period is changing and so the data cannot be fit accurately to one value for the period, or simply that the data are noisy.

Popular Modifications to the Lomb–Scargle Periodogram

There have been many cumulative steps building towards formally generalising the LSP, in order to make it more suited to a wider range of applications. This process has also served to produce more accurate results, and reduce the effects of aliasing (see Zechmeister & Kürster, 2009). Arguably one of the most useful modifications to the LSP was to incorporate an ability to handle measurement errors in the input data. This involved introducing weighted sums into the calculations (the σ_n term in Equation 4.2; Gilliland & Baliunas, 1987; Irwin et al., 1989; Scargle, 1989).

Another useful concept that has been incorporated into most modern LSPs is to remove the assumption that the data are centred around the mean. This can be fixed by simply including an offset term to the fitted sinusoidal for each candidate frequency, a method that Cumming et al. (1999) called the "floating–mean periodogram".[1] In some cases where there is an even distribution of data across the entire phase, using the sample mean as the centre is sufficient (Zechmeister & Kürster, 2009). However, when selection effects and survey cadence (common in ground–based observations) result in uneven phase coverage, simply using the sample mean can suppress peaks in the periodogram. By introducing this offset, the statistical fluctuations in sampled data can be accounted for in the model, making it more robust when there are few observations, as well as when the observations are preferentially located at certain phases of the light curve (demonstrated in VanderPlas & Ivezić, 2015; VanderPlas, 2018). The floating–mean periodogram is also advantageous when searching for long–period variability (Cumming et al., 1999).

Another obvious improvement to the standard LSP is the use of multi–term

[1] Also called "date–compensated discrete Fourier transform" by Ferraz-Mello (1981), or "generalised Lomb–Scargle method" by Bretthorst (2001) and Zechmeister & Kürster (2009). Because this latter designation also refers to other techniques of "generalising" the standard periodogram, here the case of introducing this offset is referred to as the floating–mean periodogram.

Fourier analysis, rather than relying on a single sinusoid to model the data. Following the derivation in VanderPlas (2018), Equation 4.3 incorporates the three modifications listed here, with $y_0(f)$ as the offset term, and K is the number of Fourier terms used.

$$y(t; f) = y_0(f) + \sum_{k=1}^{K} A_f^{(k)} \sin(2\pi f(t - \phi_f^{(k)})) \tag{4.3}$$

This is the form of the LSP used in this analysis.

Increasing the number of terms in the Fourier–series makes the model more robust, increasing its ability to accurately represent more complex light curve shapes, for example, the sawtooth shape of RRab stars (see Figure 4.3). Because a multi–term Fourier model can be considered a nested linear model, adding more terms to the model can only provide a better fit to the data or have no effect. The disadvantage is that the addition of terms also provides a better fit to the noise in the data as well as the signal, resulting in a noisier periodogram. As a general rule, there will be N aliases of every peak in the periodogram for a N–term Fourier model (VanderPlas, 2018). If the original data is already quite noisy, additional aliases from multi–term models can make it difficult to detect the true period.

While the Fourier coefficients primarily describe the shape of the light curve by definition, they can provide additional information. Simon & Lee (1981) were the first to show that low–order coefficients correlate with period length. Additionally, [Fe/H] values, average T_{eff}, luminosities, and masses of RR Lyrae can all be estimated from Fourier coefficients (Jurcsik & Kovacs, 1996; Clement & Shelton, 1997; Kovács, 2005; Morgan et al., 2007). While [Fe/H] values can also be derived from period–amplitude relations, it is more accurate to use Fourier terms (Sandage, 2004; Bono et al., 2007; Kunder & Chaboyer, 2009; Smith et al., 2011).

CLEAN and the Lomb–Scargle Algorithm

Performing a Fourier transform on the observation window function is equivalent to the transform of the signal and the observation window, with an inverse proportionality existing between the width of the window and the width of its transform. An observation window spans the entire duration of the measurements taken of the signal, and each observation time (assumed nearly instantaneous)

within the window, can be represented as a Dirac delta function (see Figure 7 of VanderPlas, 2018).

Because the Fourier transform of a series of Dirac delta functions (representing the near instantaneous observations), called a Dirac Comb, is another Dirac Comb, a sequence of aliases of the underlying signal are created, with their regularity corresponding to the inverse of gap widths between observations (VanderPlas, 2018). When non–uniform spacing occurs, the aliases are difficult to predict. One method of identifying the true period from alias peaks in the periodogram might be achieved via isolation of the true signal transform. The convolution theorem states that a Fourier transform of the observations is a convolution of the true signal transform and the window function transform. However, this deconvolution problem is under constrained because the window function is zero at most times, due to the near instantaneous observations.

Roberts et al. (1987) presented a new iterative approach to this problem, based on a version of the CLEAN algorithm commonly used in image reconstruction. The technique was developed in the context of radio astronomy and provided a method of removing these aliases introduced through the presence of "missing" (that is, non–uniformly sampled) data. However, VanderPlas (2018) argues the process of directly CLEAN–ing a LSP to be ineffective. The first problem is that at each iteration, the CLEAN algorithm requires the highest peak represent the primary signal, and not an alias. This is generally not the case in faint objects - cases where deconvolution is most important. Another assumption made in CLEAN is of classical fast Fourier analysis. This is not the case when LSP analysis is applied to unevenly sampled data, and adjusting the technique to suit the CLEAN process would negate the benefits of the LSP method outlined above. Thus, CLEAN was not implemented here.

4.2 Analysis

4.2.1 The OGLE Catalogue

Due to the inverse proportionality between the width of the observation window and the width of its Fourier transform, observations carried out over a long time interval result in less spread in the Fourier transform (VanderPlas, 2018). For this reason, OGLE is an excellent source of data, because observations span many years, and it has sufficient photometric sensitivity to gauge any period changes.

The OGLE catalogue, freely available online[2] (Udalski et al., 2008a), is the largest, most uniform database of variable stars, containing over 400,000 entries. It provides light–curves for many different types of variable stars (and subsets of those), including over 65,000 RR Lyrae stars (Soszyński et al., 2009, 2010a, 2011a) and 600 Type II Cepheids (Soszyński et al., 2008, 2010b, 2011b, 2013) from the Small and Large Magellanic Clouds, and Galactic Bulge. OGLE is a large–scale, unbiased sky survey that has been conducted since 1992 through the University of Warsaw Astronomical Observatory. Observations have been carried out using the 1.3 m Warsaw Telescope at the Las Campanas Observatory in Chile. An eight–chip CCD mosaic camera was used, total field of view is 1.4 square degrees, with a scale of 0.26 arcsec/pixel. Data were collected over 8 or 13 years (Soszyński et al., 2010a,b).

The OGLE survey has gone through several different phases, I to IV, distinguished by successive improvements to the CCD camera used and increasing sky coverage. The photometry for stage III (used here) is outlined in Udalski et al. (2008b). Complete observational data from OGLE–IV are not yet publicly available, and as such were not utilised here.

The OGLE catalogue provides calculated periods and corresponding Fourier coefficients (see Simon & Lee, 1981), as well as observations in both I– and V–band filters. However, since only about 10% of observations were taken in V–band compared with in I–band, only the latter data were used here. Since the amplitude (and possibly the phase) of the V– and I–band data vary, adding observations in V–band to this analysis would increase complexity without much gain in precision.

4.2.2 Lomb–Scargle Periodogram Implementation

This analysis was performed in Python using the `LombScargle` code, from the `gatspy` package[3] (VanderPlas, 2016). The `gatspy` package is used for general astronomical timeseries analysis, and performs fast calculations by utilising both the `numpy`[4] (Van Der Walt et al., 2011) and `astroML`[5] (VanderPlas et al., 2012) Python packages. The implementation of LSP analysis in Python is detailed in

[2] `http://ogledb.astrouw.edu.pl/~ogle/CVS`

[3] `http://github.com/astroml/gatspy`

[4] `http://www.numpy.org`

[5] `http://www.astroml.org`

VanderPlas (2016); VanderPlas & Ivezić (2015).

The `LombScargle` code constructs a generalised LSP (Equation 4.3), which allows for measurement uncertainties to be taken into account, the option of multi–term analysis, and removal of the original assumption that the mean is zero by solving for this mean explicitly.

OGLE data in I–band was used to construct the LSPs and from these, calculate the period of a star during consecutive subsets of the data, in order to determine whether the period changed across the observation interval. The `LombScargle` code was run with a three–term Fourier–series. The reader could be forgiven for assuming that higher–order Fourier analysis would produce more accurate results, especially since RR Lyrae light curves are generally more complicated than a sinusoid, but this is not always the case. Too many terms lead to over–fitting of the data because the model becomes more responsive to the observational noise as well as the underlying signal (VanderPlas & Ivezić, 2015). Figure 4.2 shows that there is an advantage in increasing the number of terms from one to three in the case shown (the peak is narrower and significance higher in the three–term case), but there is no real advantage in increasing the number of terms to five. In most cases, even though the model may be less robust to fitting the shape of the light curve, lower–term Fourier analysis still calculates the correct frequency to a high degree of accuracy and significance (Scargle, 1982, see also Section 4.1.1). Additionally, a higher number of terms results in aliasing at multiples of $\sim$0.5 d and reported a very large significance. While three terms may not be enough to accurately represent the light curve shape of some of the RR Lyrae stars, it is sufficient to determine the period (VanderPlas, 2018). Comparing the three– and five–term models in the phase plots (Figure 4.3), there again appears to be little gain in increasing the number of terms past three, although it is obvious that one term is insufficient. Period iterations were on the order of 10^{-8} d in most cases, as this was deemed to be sufficient to identify changes in periods on the scale required. The uncertainties provided in the OGLE catalogue are quoted to a limit of 10^{-7} d.

The stars were divided into groups based on their periods and analysed separately for a number of reasons, primarily to make the LSP–analysis calculations as efficient as possible. Since the period was already known from OGLE, the frequency search interval could be narrowed considerably. A smaller search window also has the added bonus of simply not allowing for many aliases of the signal. Additionally, the problem period value of 0.5 d could be avoided, and double mode

oscillators can be put in a group that included their fundamental frequency, but not their overtone. In this way, it was guaranteed that the analysis was looking at changes to the primary period and not switching between the two.

To determine whether a change in the period had occurred, the observations were divided into subsets in two ways. The first being simply in four sections, covering four successive time intervals. The second method was to create a "moving–window" time interval using 30% of the data at a time. The moving–window was implemented by dividing the data into ten sections, and using three to form each time interval for the period analysis. Each successive time subset was created by excluding the earliest section from the previous time subset and including the next section along. In this way, each time subset analysed had overlapping sections with the subset prior and following (except in the cases of the first and last time intervals). The data subset were of equal number of observations, rather than equal time intervals. This was done because of the high variation in accuracy of the method with changing number of data samples. Additionally, there were gaps in the data where no observations were made on some sources. The preliminary analysis here found that the signal–to–noise ratio (S/N) was too low to be significantly different from alias signals when there were less than about 100 samples in a calculated LSP. Because of this, an observation number threshold was imposed for a star to be included in this research. As a result 37 sources out of the $\sim$ 2400 type–RRab, RRc, RRd, and BL Herculis stars were excluded.

The period was also calculated using all observations, to determine an overall value, which was compared to the value supplied in the OGLE database. For the few cases where this differed significantly (8% of total sample), the stars were omitted from further analysis. This was done as a level of assurance of the accuracy of the results derived using the LSP method.

Uncertainty/Significance Estimates

In Fourier–space, the accuracy of the frequency reported by the LSP is directly related to the peak width. However, this assumes that this reported frequency is indeed correct. The S/N of the highest peak gives an indication of how likely it actually is that the frequency chosen represents the data (that is, the significance of the estimate), and so should also be considered (Scargle, 1982). VanderPlas (2018) provides a detailed discussion on why presenting the uncertainty of a peak in the LSP in terms of peak width or Gaussian error bars is flawed. The author

suggests a more useful concept would be a measure of the significance of a peak in the periodogram, or the probability that the peak is the true period or an artefact of random errors aligning. In this case, due to the periods calculated here being directly compared with those already provided by OGLE, this is not a necessary consideration. For the purposes of this analysis, some method of estimating the accuracy (and thus, usability) of calculated periods was essential in order to determine whether the observed change in the period is due to an actual change in the structure of the star or simply a result of noise in the data.

When estimating this accuracy of the peak frequency reported in a periodogram, a cursory approach might be to simply use the half–width at half–maximum of the peak ($f_{1/2}$). This can be approximated as the inverse of observation window ($1/T$), for observations spanning many periods (see VanderPlas, 2018, for a discussion). Owing to the fact that $1/T$ would be very small in this case due to the OGLE survey spanning years, this would result in a very high reported accuracy, and so does not provide the best estimate, especially in the case of a long observation cadence.

A more realistic representation of the accuracy of a period peak reported by a LSP model would be to assume the period peak is a Gaussian curve (a justified assumption; see Jaynes, 1987; Bretthorst, 1988) of the form

$$y(x) = \frac{1}{\sigma\sqrt{2\pi}} e^{-\frac{(x-\mu)^2}{2\sigma^2}}, \tag{4.4}$$

where μ and σ^2 are the mean and variance respectively. In the case of a normal distribution, the mean is equal to the mode, leading to the following

$$y(f_{1/2}) = y(\mu)/2. \tag{4.5}$$

In this way, standard deviation (σ) can be expressed in terms of the half–width at half–maximum of the periodogram peak:

$$\sigma = \frac{f_{1/2}}{\sqrt{2\ln 2}}. \tag{4.6}$$

Another approach would be to consider the LSP model in terms of Bayesian statistics. Again, treating the periodogram peak as a Gaussian curve, the uncertainty in that peak can be related to number of observations N and their average S/N (Σ), through the following approximation from VanderPlas (2018; see also Gregory, 2001):

$$\sigma_f \approx f_{1/2}\sqrt{\frac{2}{N\Sigma^2}}. \tag{4.7}$$

This method returns a more realistic representation of the accuracy of a period peak reported by a LSP model because it also accounts for the number of observations and the measurement uncertainties through the S/N. In this analysis, Equation 4.7 is used to estimate the uncertainties. The derived values are on a similar order to those provided in the OGLE data.

Aliasing Considerations

As outlined in Section 4.1.1 above, in some cases the highest peak in the periodogram is not the true period, but an alias of it. This can be due to a number of reasons.

When data are not sampled at uniform intervals, the lack of structure in the observation spacing results in signal aliases that can be difficult to predict the frequency of, and hence, exclude from the calculated periodogram (VanderPlas, 2018). This can also cause random noise in the Fourier transform. However, it does mean that the Nyquist observing limit no longer applies in the traditional sense. In most cases, a much smaller period is able to be detected than in an equivalent uniformly sampled dataset. For a detailed discussion of this phenomenon, see VanderPlas (2018) and references therein. In the case of this research however, it is irrelevant because changes in the period are being sought, with an average period already established by OGLE.

Additionally, for multi–term LSP models, it is possible to have extra peaks in the periodogram from higher harmonics of the fundamental frequency. Even in a single–term model, there is the potential for aliases of the signal to occur in the resulting periodogram, due to the beat frequency between the true period and the time between observations (usually approximately 1 d in ground–based surveys; see VanderPlas & Ivezić, 2015; VanderPlas, 2018). Thus, all suspected changes in the period detected must be further investigated to determine if the period is actually changing or whether the new highest peak in the periodogram is simply an alias.

4.2.3 Phase Analysis

In addition to directly considering the change in source periods across different time intervals, the LSP–derived values were also used to construct Observed–Calculated (O–C) plots, a popular method for periodicity analysis. The models derived in the LSP method were used to calculate the amplitude across one period cycle and the results compared to the observations made in OGLE, once they too had been transformed to phase space. In this way, the shift in phase can be plotted over time to isolate changes in the periodicity. This is similar to the Hertzsprung method outlined in Berdnikov (1992). Fitting a representative light curve to the observations based on minimising the sum of squared differences happens as part of the LSP process.

Only those observations determined to be maxima were used (magnitude values within 5% of the determined maximum), since there is inherent ambiguity in choosing samples at any other points in the period cycle. Due to the sawtooth–shaped light–curves of RRab–type stars (the most common RR Lyrae), the minima of the calculated light curve often did not align perfectly with the observed values in the phase–plots. Rather than increasing the number of Fourier terms in the models and risk aliasing washing out significant results, observations taken at the minimum point in the cycle were also excluded. The maximum brightness was set to zero in phase space, for ease of calculations.

4.3 Results

Two methods of determining periodicity variation were utilised here. The first was to calculate the average period across consecutive subsets of the observations. A moving average was calculated to smooth out extraneous noise in the source signal. Results of the LSP analysis were checked for significant ΔP values, taking into account uncertainties. Each star reporting a significant change in period across an observation subset was then manually checked for any inconsistencies (for example, aliasing). In the case of double–mode pulsators (RRd), the assumption was made that it was the fundamental frequency that was varying in the initial analysis and followed up on any cases in later stages. Since canonical stellar evolution theory predicts period variability to occur in RR Lyrae at a rate of less than $\sim 3 \times 10^{-10}$ d/d under normal conditions (detailed above, see also Lee, 1991; Smith, 2013), this was used as a cutoff criterion.

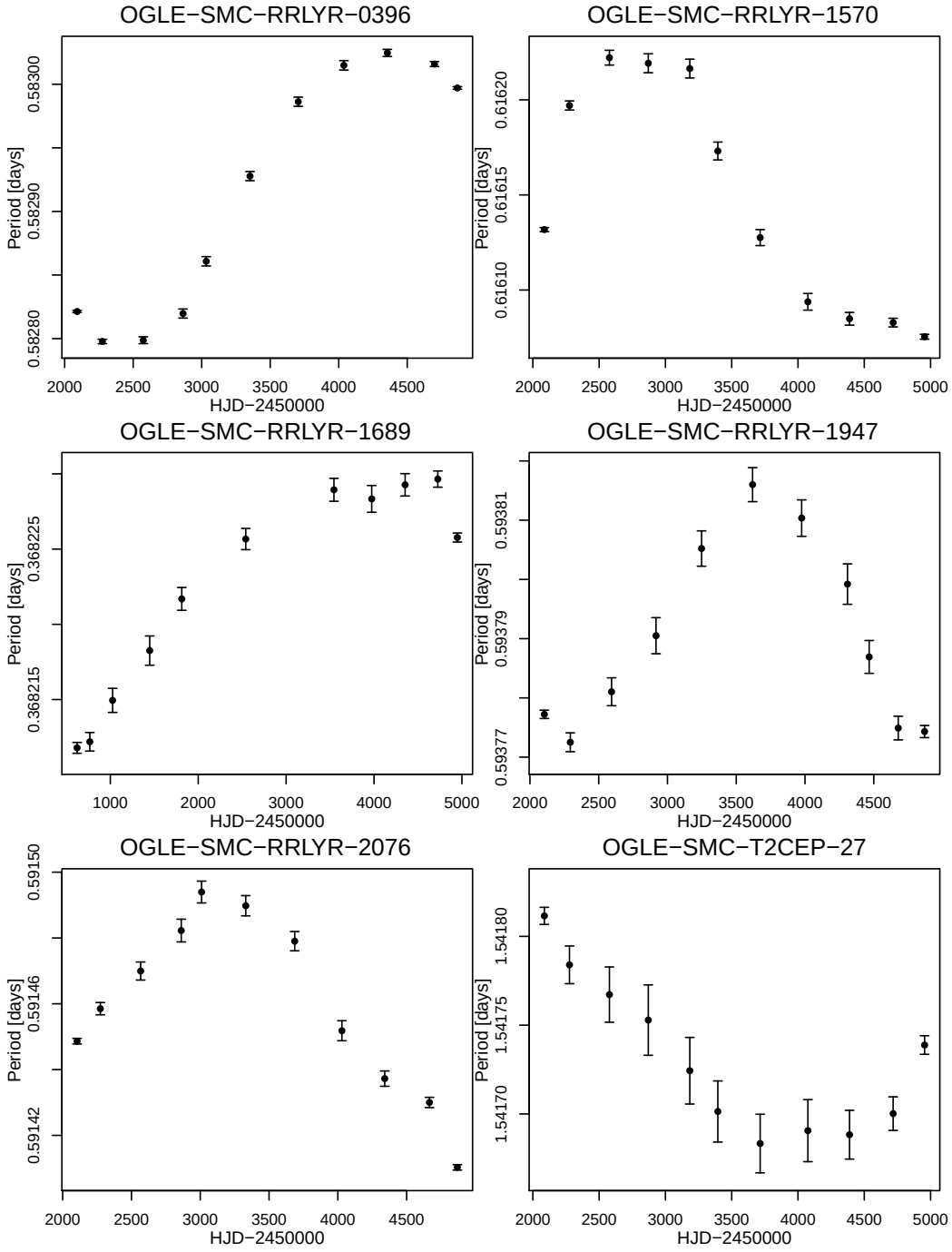

Figure 4.4: Change in period across selected variables from the OGLE database. The values were calculated using Lomb–Scargle analysis and smoothed across a moving average. The full results are in Appendix E.

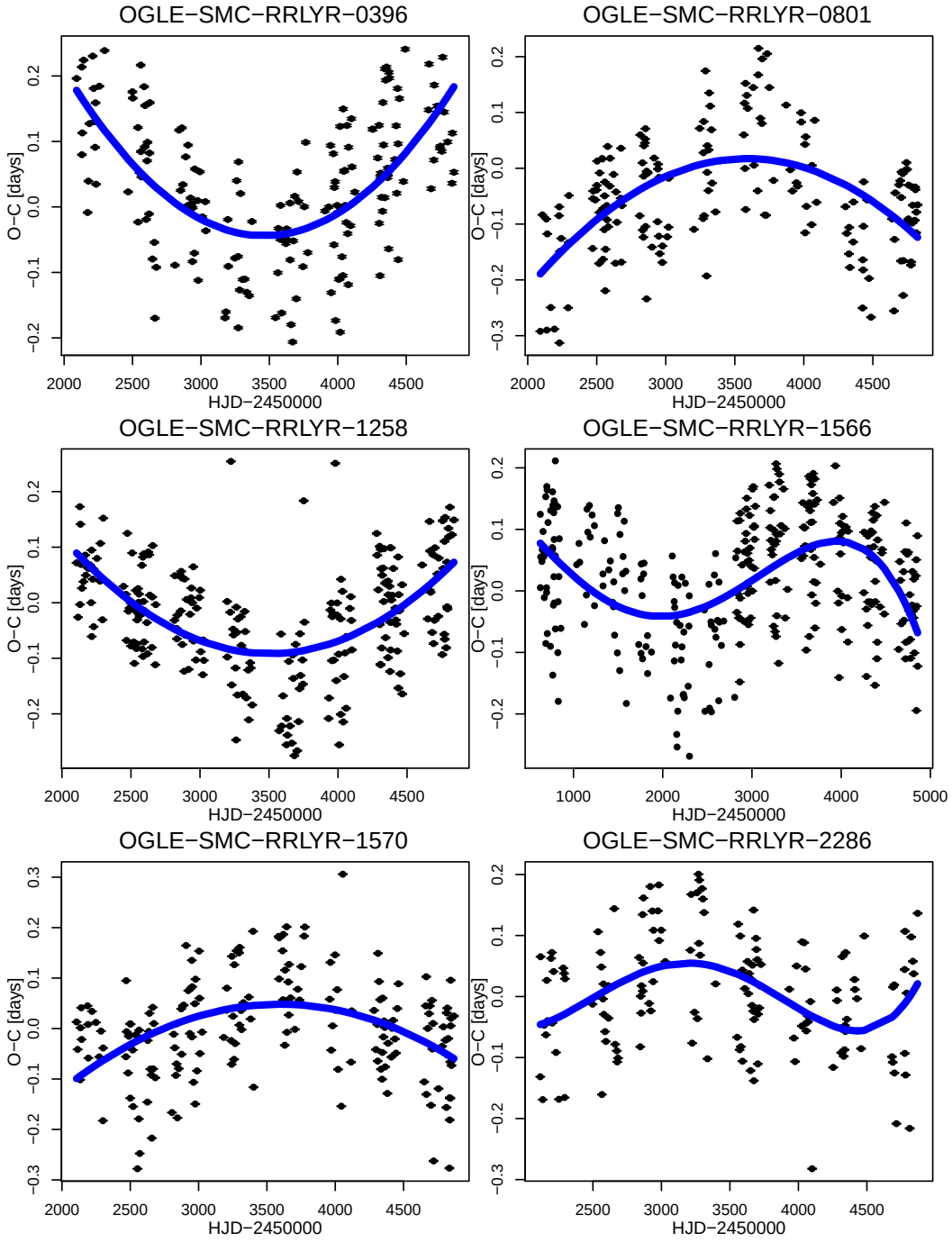

Figure 4.5: O–C plots of selected variables from the OGLE database. The values were calculated using Lomb–Scargle analysis and then converted to phase space. See Figure 4.7 for phase plots.

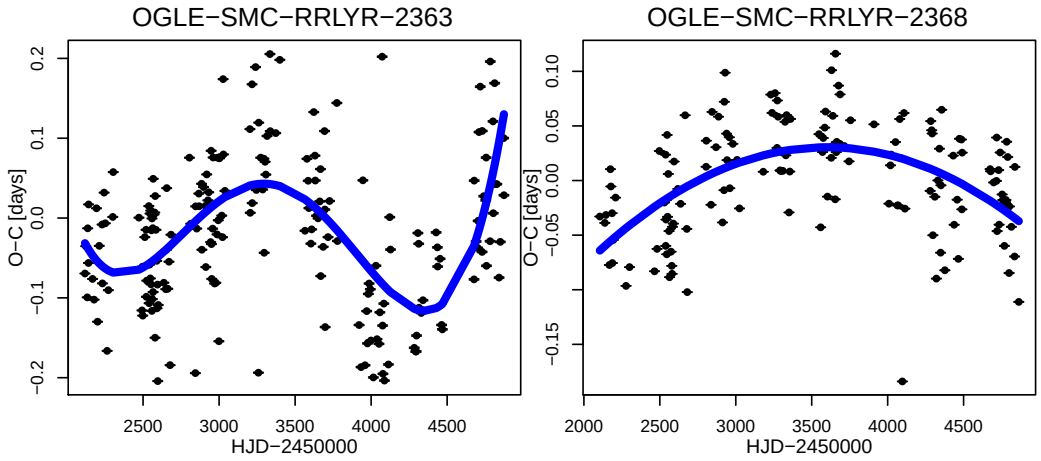

Figure 4.6: O–C plots of selected variables from the OGLE database. The values were calculated using Lomb–Scargle analysis and then converted to phase space. See Figure 4.7 for phase plots.

Analysing the average period of the moving window identified 176 variables with significant changes in their periodicity, out of a sample of 2366 RR Lyrae and 17 BL Herculis Type II Cepheids from the SMC. The results of six cases are shown in Figure 4.4 as period/time plots, with the full list of results in Appendix E.

The second approach was to construct O–C plots based on the period produced in the LSP analysis for the entire set of observations. Figures 4.5 and 4.6 show the stars where O–C plots showed evidence of period variability (also listed in Appendix E). The results from O–C plots can be compared with the period/time plots by taking into account the number of cycles that the O–C plots span. Only these eight cases were identified as varying in periodicity, compared with the 176 sources from the first method. Two RR Lyrae were identified by both methods: OGLE-SMC-RRLYR-0392 and OGLE-SMC-RRLYR-1570 (shown in Figure 4.4). Figure 4.8 plots all 182 identified cases. The source OGLE-LMC-RRLYR-10752 has been previously identified as having a negative period change rate by Soszyński et al. (2016) and is shown in the Figure for comparison. Out of these, 62 had negative $\dot{P}$ values, while a further 64 experienced both increases and decreases in their period over the OGLE observation interval.

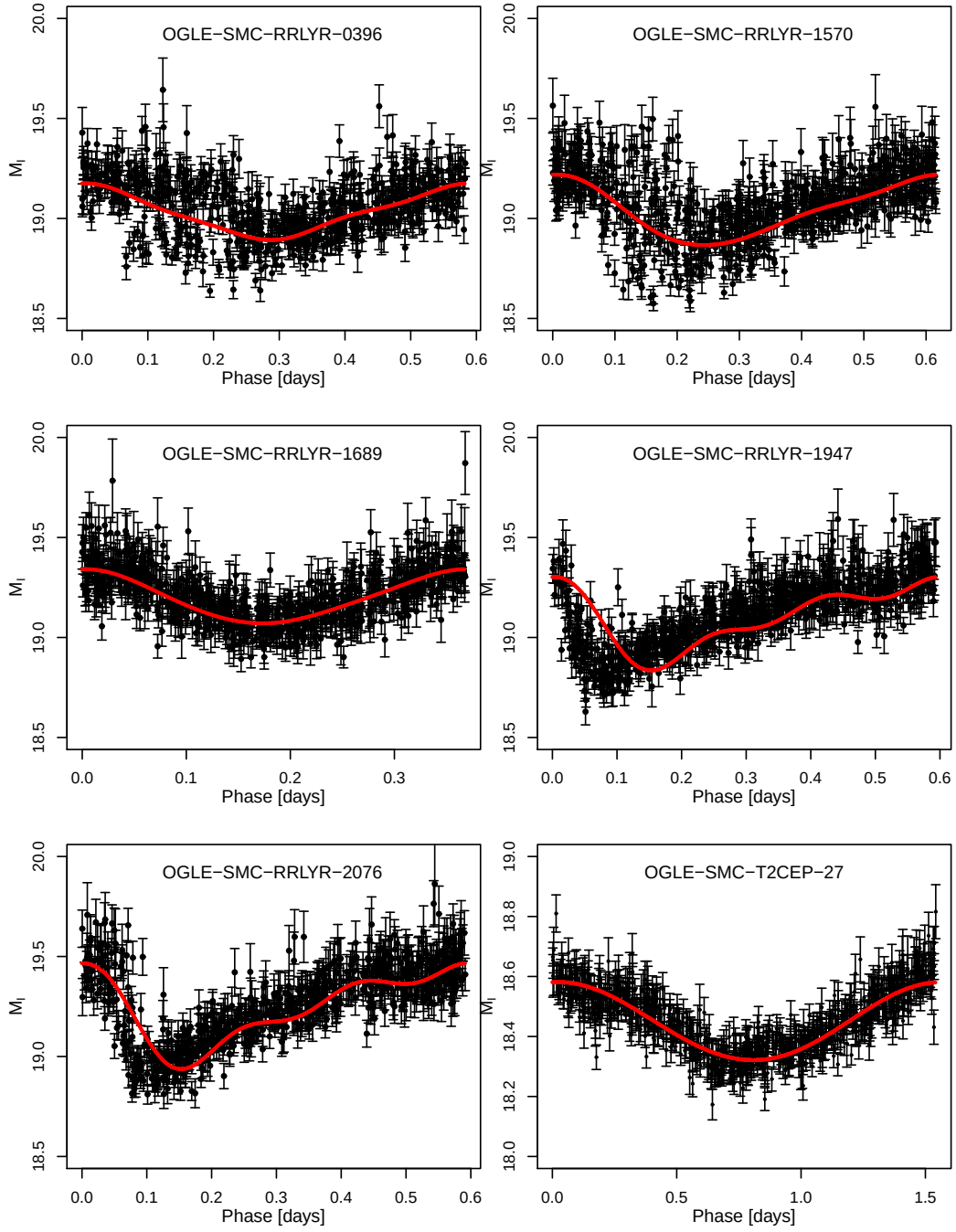

Figure 4.7: Phase diagrams for sources in Figures 4.4 and 4.5, demonstrating the need for complex methods to isolate changes in periodicity from observational noise.

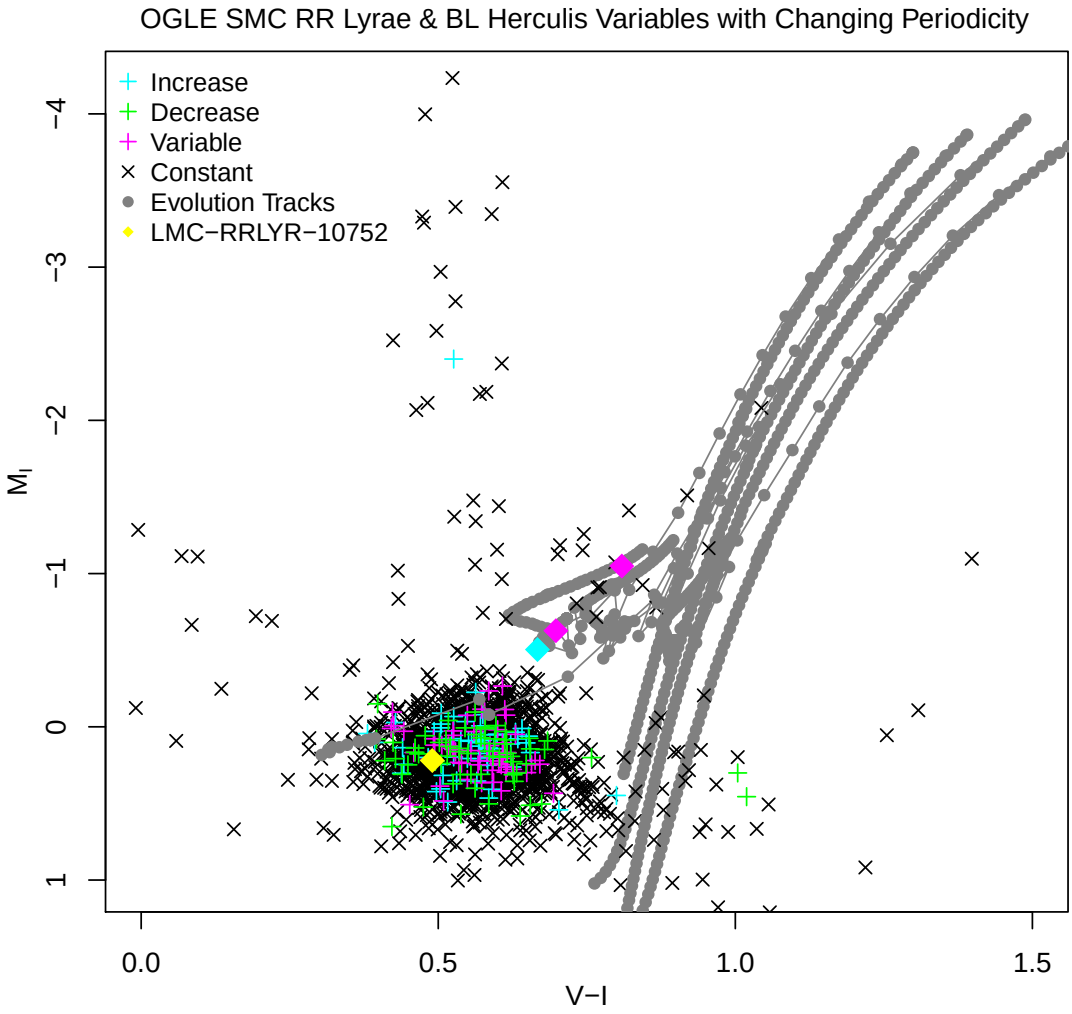

Figure 4.8: Similar to Figure 4.1, the RR Lyrae and BL Herculis variables calculated to have undergone a change in periodicity are plotted (see Section 4.3), with MIST evolutionary data showing the RGB and HB phases for reference. Those stars with a positive rate of change in periodicity are marked in cyan, a negative $\dot{P}$ in green, while those stars undergoing both increases and decreases in their periods are shown in magenta. There does not appear to be any trend present those with non–zero $\dot{P}$ values and those with constant periods (marked in black). The cases with a negative $\dot{P}$ value that follow closely along the path from TRGB to HB have been identified as high–possibility CFP stars (see Section 4.3.1). Three solitary stars have been identified as travelling blue–ward along the RGB towards the HB (see Section 4.3.1 for discussion). The source OGLE-LMC-RRLYR-10752 has been previously identified as having a negative period change rate by Soszyński et al. (2016) and is shown here for comparison (distance modulus of 18.49 for LMC used Hoyt et al., 2018).

4.3.1 Likely Helium–Flash Candidates

In the search for possible HeF candidates, the ideal case was where there was a negative rate of period change in a star positioned above the ZAHB. In their CFP evolution simulations, Silva Aguirre et al. (2008) calculated $\sim 76\%$ pre–ZAHB variables to have negative $\dot{P}$ values. Additionally, according to the period–mean density relation in Equation 1.13, the period is inversely proportional to the square–root of the average density. Thus, as the star descends the RGB to the ZAHB, the density increases as the star shrinks, the periodicity is expected to decrease.

Ten such cases were selected from Figure 4.8 where there was strong overlap with the expected CFP evolution path of low–metallicity isochrones, representative of the SMC stellar population. These are identified in Table 4.1. The majority of the cases were fundamental mode oscillating RR Lyrae (seven), with two RRc cases and just one double mode oscillators identified. No Type II Cepheids were isolated with these criteria. Cases where the period increased or decreased but then returned to a previous value could be secondary subflashes following the main event, or it could be due to unstable structural changes such as mixing events (Sweigart & Renzini, 1979; Koopmann et al., 1994; Silva Aguirre et al., 2008). Since these cases are less likely to be CFP stars, these are shown separately in Table 4.2.

Twenty cases with either positive, or positive and negative $\dot{P}$ values are listed in Table 4.2. Figure 4.8 shows three blue–ward sources, following the RGB path down to the HB. While sources with decreasing periods are more likely to be HeF candidates, these three cases are important to note because they could represent slightly younger, less metal–poor stars than the majority - thus more representative of the actual SMC stellar population (Dobbie et al., 2014; Choudhury et al., 2018). The two stars showing an increase and decrease in period length are OGLE-SMC-RRLYR-0728 and OGLE-SMC-RRLYR-0921 (shown in magenta in Figure 4.8), while OGLE-SMC-T2CEP-27 (shown in cyan in Figure 4.8) has an increasing period.

4.4 Discussion

As a variable red giant star evolves from the initial HeF through the CFP towards the HB, its period is expected to decrease (Silva Aguirre et al., 2008; Catelan,

OGLE ID #	**Type**	$\dot{P}$ [$\times 10^{-9}$ **d/d**]
0056	RRab	-16.97 ± 0.72
0138	RRab	-10.11 ± 0.41
0148	RRc	-6.44 ± 0.32
0305	RRab	-13.74 ± 0.28
0486	RRd	-3.61 ± 0.48
0978	RRc	-9.304 ± 0.051
1049	RRab	-5.60 ± 0.31
1530	RRab	-24.91 ± 0.33
1644	RRab	-7.56 ± 0.46
2191	RRab	-66.40 ± 0.31

Table 4.1: The cases of negative period change rate identified as likely HeF candidates from Figure 4.8. For comparison to other studies, these change rates are on the order of 0.7–25 d/Myr. The sources all have the prefix OGLE-SMC-RRLYR-.

2009). This is due to changes in the structure of the star causing variations in the periodicity which can be described through the period–mean density relation (outlined above; see also Chapter 1).

RR Lyrae and BL Herculis stars were chosen for this study because their structures and variability mechanisms are generally understood, they have relatively short periods, meaning that change across many cycles could be measured, and they pulsate radially (as opposed to more complicated mechanisms). These stars represent a way to observationally probe the rare CFP population because their periods and light curve shapes are highly sensitive to the internal structure of the star.

Apart from drastic internal structural changes brought about during the CFP, high period change rates in RR Lyrae could also be caused by small random mixing events brought on by the redistribution of elements in the cores of HB stars (Sweigart & Renzini, 1979). Another possible explanation for changes in periodicity exists if the star has similar magnetic cycles to the Sun, specifically hydromagnetic effects. Stothers (2006) suggested transient magnetic fields in hydrogen and helium ionisation zones might in fact be a cause of the Blažko effect. The Blažko effect (Blažko, 1907) is periodic modulation of the light curve shape from as yet uncertain causes, on timescales longer than the fundamental period. A study by Chadid et al. (2004) concluded that Blažko modulation does not require strong surface magnetic activity to occur, but the presence of such effects

OGLE ID #	**Type**	$\dot{P}$ [$\times 10^{-9}$ **d/d**]
0396	RRab	$\|109.1\| \pm 1.1$
0534	RRab	37.91 ± 0.17
0728	RRab	$\|31.8\| \pm 1.4$
0771	RRab	$\|23.0\| \pm 1.8$
0921	RRab	$\|13.78\| \pm 0.35$
1028	RRd	$\|24.4\| \pm 1.7$
1077	RRab	5.87 ± 0.12
1400	RRab	$\|42.08\| \pm 0.93$
1423	RRab	8.45 ± 0.21
1522	RRab	2.62 ± 0.34
1670	RRab	$\|8.77\| \pm 0.60$
1918	RRab	7.94 ± 0.36
1964	RRab	$\|11.97\| \pm 0.64$
2129	RRab	$\|20.8\| \pm 1.6$
2286	RRab	$\sim \|5.2\|$
2363	RRc	$\sim \|300\|$
2368	RRc	$\sim \|16\|$
2445	RRab	45.74 ± 0.87
2471	RRc	11.20 ± 0.33
27	BLHer	$\|78.8\| \pm 7.5$

Table 4.2: The cases of positive and variable (sources exhibiting both positive and negative $\dot{P}$ values) period change rate identified as possible HeF candidates from Figure 4.8. These are less likely to be HeF candidates than those presented in Table 4.1. The sources all have the prefix OGLE-SMC-RRLYR-, except for the last source (OGLE-SMC-T2CEP-27).

could possibly contribute to the modulation through deeply embedded magnetic fields, as in our Sun (Stothers, 2006). No Blažko modulation was identified from this analysis, possibly requiring the observations to span even longer.

An RR Lyrae reported to have its period shorten at the rate of $(2.9 \pm 0.3) \times 10^{-9}$ d/d by Soszyński et al. (2016, ; OGLE-LMC-RRLYR-10752) is suspected to be a fast–evolving binary pulsator (see Pietrzyński et al., 2012). If this assertion is correct, it is possible that the HeF candidates identified in Table 4.1 might also fall into this binary pulsator category. The overlap in colour–magnitude space of OGLE-LMC-RRLYR-10752 in Figure 4.8, coupled with similar magnitude changes, supports this. Excluding such binary systems from these results would require follow–up spectroscopic observations, which is beyond the scope of this project. However, Pietrzyński et al. (2012) calculated that a mere 0.2% of RR Lyrae stars would fall into this category, while the cases listed in Table 4.1 represent 0.8% of the population of RR Lyrae within the SMC. The changing periodicity of OGLE-LMC-RRLYR-10752 is explored further in Section 4.4.1.

Figure 4.8 shows that the vast majority of the RR Lyrae and Type II Cepheids identified here as having a variable period, overlap with the HB of old, metal–poor stars. Results from Chapter 3 show the evolution time through the entire CFP is approximately 1.4 Myr for a typical RR Lyrae or Type II Cepheid SMC star (intermediate–age, metal–poor). Utilising MIST data (recall Chapter 3; Dotter, 2016; Choi et al., 2016), a typical HB lifetime for an SMC–type low–mass star would be 85–100 Myr. As such, it can be expected that roughly 35 SMC variable stars from the sample of 2383 here are in their CFP. Realistically the number will be slightly lower since stars spend the majority of their CFP close to the HB; after the initial onset of helium–ignition, the rapid descent gradually slows down towards ZAHB (for example, see Figure 6 of Silva Aguirre et al., 2008).

Figure 4.8 does not indicate any patterns in stars with detectable period changes, compared with those with constant periods. Both groups are concentrated in the same area in colour–magnitude space. Seeing both positive and negative period change rates around the HB is to be expected, since this where blue loops and other mixing events occur. It is worth noting that the variables identified here as having both positive and negative period change rates, often have the change centred on the middle of the observation interval (see Figures 4.4, 4.5 and 4.6), suggesting that perhaps there may be some kind of interference or observational effect present.

Another source of uncertainty to bear in mind is that the method of identify-

ing maximum brightness points for use in the O–C plots may not be as accurate as required for this level of analysis, but was left in this project as a comparison. Bright outliers can shift the apparent observed maximum point in the light curve, making it appear as though the periodicity is shifting, and so should be removed automatically in the analysis process. Given the increased complexity in implementing this extra stage in the analysis, the recommendation would be to instead just use the moving average technique, if sufficient observations are available.

This high level of scatter evident in the phase plots (Figure 4.7) is possibly a result of the sampling rate being close to once a night which is approximately twice or three times the period value. For one of the two cases where there was period change evident in both direct period analysis and O–C methods, the results between the two are identical (OGLE-SMC-RRLYR-0396, $\dot{P} \approx \pm 10^{-7}$). However for OGLE-SMC-RRLYR-1570, the results were quite different, with the period/time plot measuring a rate $\dot{P} \approx -6 \times 10^{-8}$, while the O–C method reported $\pm 7 \times 10^{-9}$.

The average scatter in the O–C plots is $\sim$ 2.7 d across roughly 5000–6000 period cycles, while the error bars in the period/time plots generally represent $\sim 5 \times 10^{-6}$ d across the same time interval. This means that while the period/time analysis has uncertainties on the order of 10^{-10} d/cycle (below which can be considered normal variability in RR Lyrae; see Section 4.3; Lee, 1991; Smith, 2013), the O–C method here only has an accuracy on the order of 10^{-5} d/cycle. As such, an improved method, reducing the uncertainty in determining the maximum brightness observations, would be preferable to collecting data spanning many decades.

4.4.1 Comparison with Previous Results

In order to gauge the accuracy of both methods utilised above, the analysis was also performed on six variable stars (also from the OGLE catalogue), previously shown to have changes in their periodicity. A selection of five Classical Cepheids with short periods (0.8–3 days) were chosen from Poleski (2008), along with an RR Lyrae presented in Soszyński et al. (2016). Table 4.3 compares the changes in periodicity calculated here with the values reported in the previous studies. These results are in good agreement except for the case of OGLE-LMC-CEP-1861, where the period rate of change calculated here is positive, while Poleski

(2008) shows a negative value over the same observation time interval. This is surprising considering how well the other results are reproduced.

Figure 4.10 shows the LSP calculated periods smoothed across a moving average, clearly demonstrating significant changes in the period of each star. For the most part, the period change trends visible here compare favourably with those in Figure 6 of Poleski (2008), backing up the numerical analysis. Figure 4.11 shows the O–C plots of the same stars. There is a slight offset visible between the results of the period/time plots in Figure 4.10 and the O–C plots in Figure 6 of Poleski (2008) and the case of OGLE-LMC-CEP-1742 in Figure 4.11 because the points in the period/time plots are averaged over a small time window.

In this analysis, only OGLE-LMC-CEP-1742 can be assumed to be changing in periodicity from the O–C plots, the other cases are inconclusive. This is due to the high levels of scatter evident across the phase plots in Figure 4.9. A more sophisticated method for isolating points of maximum magnitude in phase–space and excluding outliers may have yielded better results. Unfortunately, such an involved approach was outside the scope of this project. However, the trend shown in Figure 4.11 is very similar to that demonstrated in Figure 6 of Poleski (2008), and the calculated period change rates are equivalent to Poleski's in both methods used here. Thus, the analysis here can be assumed to be generally equivalent to previous studies.

Recently, Michail et al. (2018) has analysed period change rates in a random sample of twenty fundamental–mode LMC Classical Cepheids, using photometry data from the OGLE database in a pilot study. Data was used from both OGLE-III and OGLE-IV, with observations spanning 15 yrs. The authors describe a similar method to that used here: a Fourier model with 5–15 terms is fitted to the phase–folded light curve based on least–squares method which takes into account measurement uncertainty (detailed in Tegmark, 1997). The difference is the light curve is phase–folded before the model is fitted, rather than here where the LSP model is applied straight to the raw data. Figure 1 from Michail et al. (2018) gives a $\dot{P}$ value of -0.26 s/yr ($\sim 8 \times 10^{-9}$ d/d), comparable in magnitude with most detections here.

The initial results of Michail et al. (2018) suggest that LMC Cepheids may undergo smaller rates of period change than Cepheids in the Milky Way with similar periods (Turner, 1998; Sirorattanakul et al., 2017; Erickson et al., 2018), however the current sample is too small to provide concrete evidence. The authors are currently analysing the full LMC Cepheid catalogue to provide more

OGLE ID	LSP $\dot{P}$ [$\times 10^{-9}$ d/d]	Previous Works $\dot{P}$ [$\times 10^{-9}$ d/d]
OGLE-LMC-CEP-1007	-7.81 ± 0.40	-5
OGLE-LMC-CEP-1119	$\|269.3\| \pm 7.6$	200
OGLE-LMC-CEP-1159	$\|93.5\| \pm 5.2$	$\|80\|$
OGLE-LMC-CEP-1742	372 ± 90	300
OGLE-LMC-CEP-1861	40.2 ± 1.6	-20
OGLE-LMC-RRLYR-10752	-4.49 ± 0.82	-2.9 ± 0.3

Table 4.3: Approximate rates of change in periodicity ($\dot{P}$; days per day) as calculated here using the LSP analysis detailed in Section 4.1.1, compared to results from previous studies over the same time interval (Poleski, 2008; Soszyński et al., 2016, for the Cepheid and RR Lyrae, respectively). Absolute values represent both positive and negative period changes over interval. The O–C plot in Figure 4.11 suggests a $\dot{P}$ value for OGLE-LMC-CEP-1742 similar to the result from Poleski (2008, $\sim 3 \times 10^{-7}$).

quantitative conclusions, in addition to Cepheids from the SMC to represent a lower metallicity population.

4.4.2 Future Efforts

The cases listed in Appendix E should serve as a basis for follow–up observations, with the aim of gaining a more comprehensive understanding of varying periodicity in RR Lyrae and BL Herculis stars in general, with the possibility of isolating red giants currently evolving through the CFP. Table 4.1 provides a list of the most likely HeF candidates. Unfortunately, the attributes that made them probable post–HeF stars (Silva Aguirre et al., 2008; Catelan, 2009), also apply to fast–evolving binary pulsators. Separating these two types of variables would require spectroscopic observations or determination of the stellar mass. Pietrzyński et al. (2012) calculated OGLE-BLG-RRLYR-02792 to have a mass of 0.26 $M_{\odot}$, meaning that it could not be a classical RR Lyrae star, leading the authors to investigate other periodic driving mechanisms and conclude a binary system to be the cause.

The results from Chapter 3 showed that while stellar age had very little effective on the evolutionary times (with the exception of stars 1–2 Gyr), high–metallicity stars spent much longer in the CFP than their low–metallicity counterparts (see Figure 3.2). For this reason, more HeF candidates should be expected in the LMC as it is more metal–rich than the SMC, and so will be spending

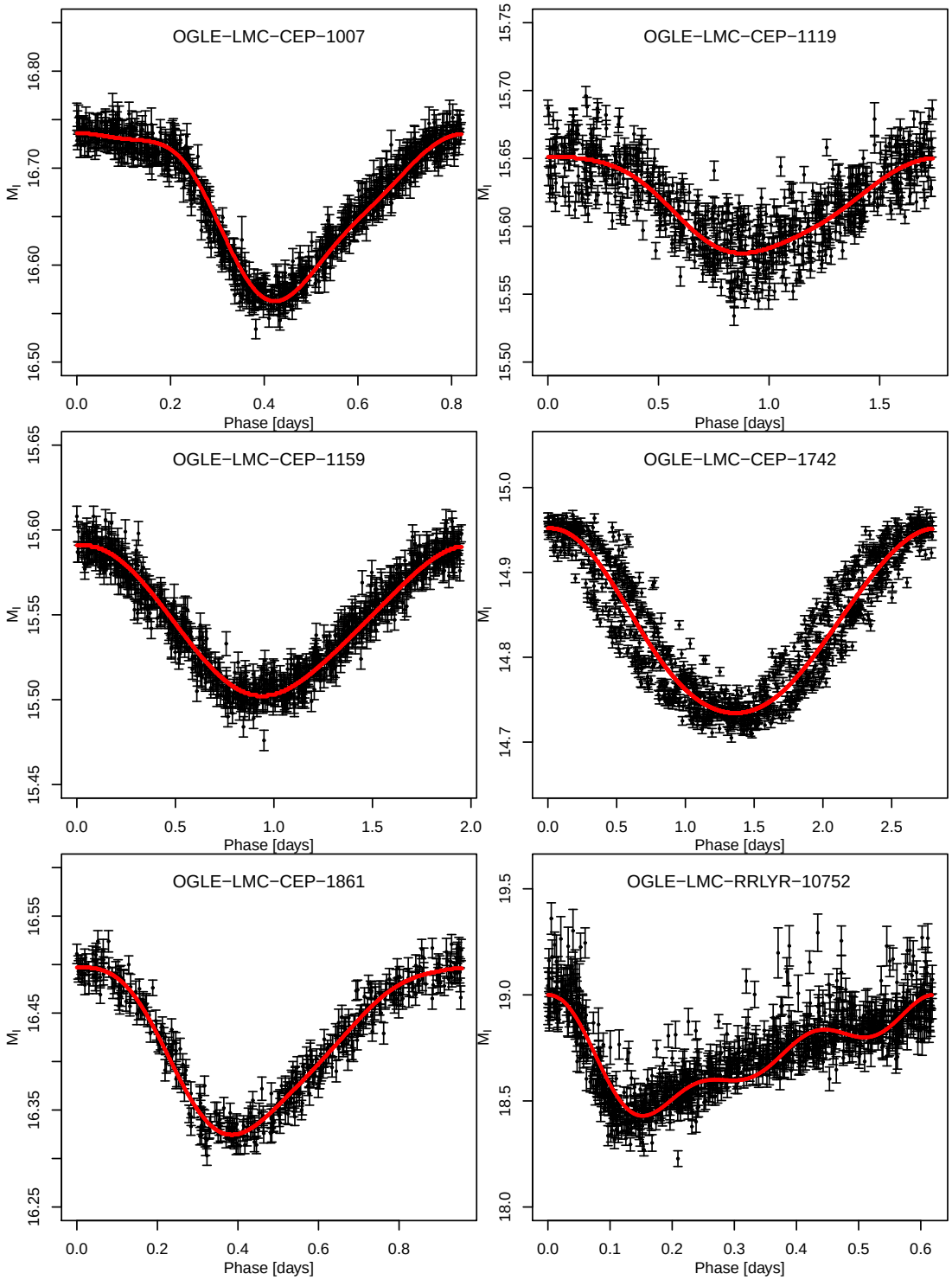

Figure 4.9: Phase plots of observations (black points) over one period cycle. The light curve as determined by Lomb–Scargle analysis is shown in red. The sources were chosen to compare results with previous studies.

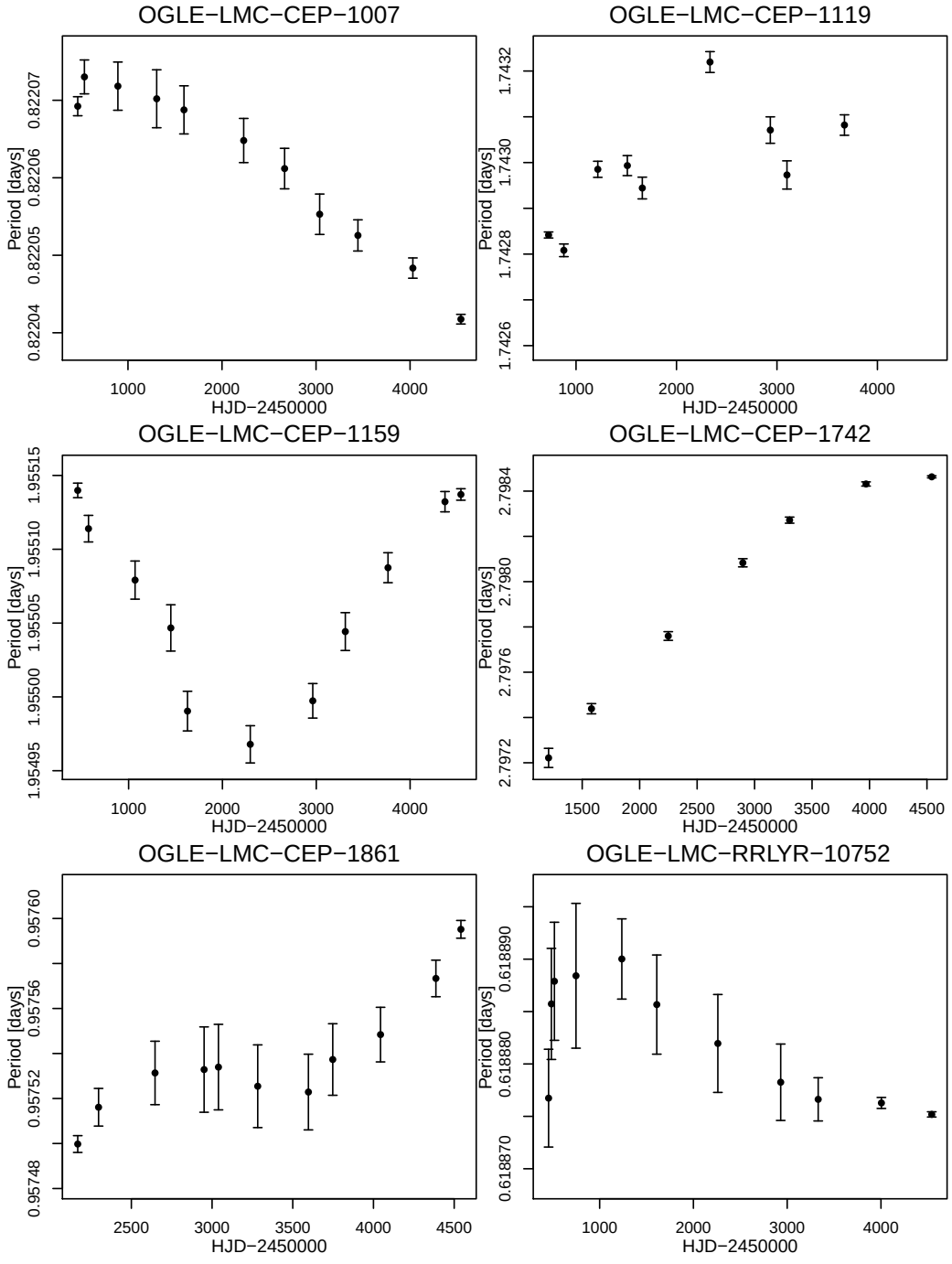

Figure 4.10: Calculated changes in period for comparison with previous studies. Compare Cepheid results to Figure 6 of Poleski (2008), and the RR Lyrae to results in Soszyński et al. (2016). See also Table 4.3.

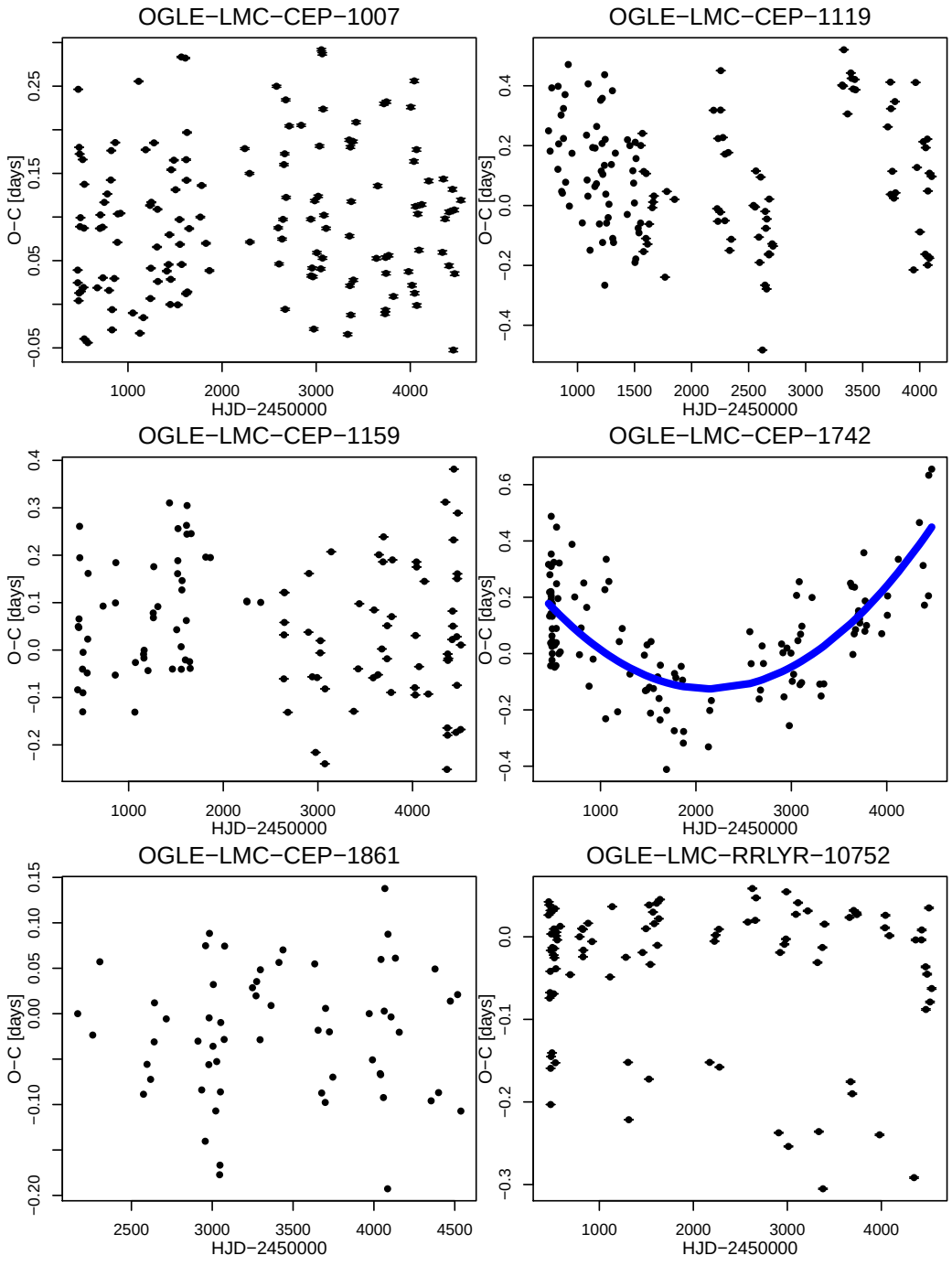

Figure 4.11: Observed–Calculated (O–C) plots of sources from previous studies. Only OGLE-LMC-CEP-1742 can be assumed to be changing in periodicity from these plots.

more time in the CFP. Conversely, the lower metallicity stars present in the SMC would tend to spend a larger fraction of the post–HeF evolution in the instability strip due to the extended HB (see Chapter 2), although this is unlikely to offset the effects of the much larger sample size and the larger proportion of old stars in the LMC. Since only the oldest, metal–poor stars cross the instability strip and the SMC is mainly intermediate–age, there are few stars that match these search criteria.

Stars from the SMC were chosen for this foundational analysis as there were a small enough number to use the complete sample from the OGLE database. There are roughly ten times more of RR Lyrae and Type II Cepheids in the LMC catalogue. A representative sample of LMC stars would have been required if they were to be utilised here, and as such a complete search for periodicity changes would not have been possible, making the results less applicable to other astrophysical areas of research.

For the broad application of studying any changes in periodicity, more up to date observations can be incorporated into the analysis to identify cases where the trend of change in periodicity continues, once OGLE-IV data are available. To continue the search for HeF candidates, this variability analysis can then be extended to candidates in the LMC, where more CFP stars are expected.

As stated above, Scargle (1982) shows that while RR Lyrae light curves are more complicated than a sinusoidal wave, Fourier–series analysis can still detect the correct frequency to a high degree of accuracy (peak width) and significance (peak height). However, in order to effectively and accurately utilise the O–C method, the light curves should be represented as accurately as possible by the model (see Figure 4.7 and Section 4.2.3). This is especially true of RRab–type stars, the typical case having a sawtooth–shaped light curve. A method of suppressing aliasing would greatly assist here, allowing for an increased number of Fourier terms in the LSP model, without the risk of the true period being lost in the periodogram (recall Section 4.2.2).

While this research represents the first search for HeF candidates within catalogued observation data, follow–up continuous observations of these identified variables are required to comprehensively test the validity of these results before definitive conclusions can be made.

Chapter 5

Summary and Conclusions

The core–helium flash is the most violent event in a low–mass star's evolution, at its peak producing as much luminosity as some galaxies ($L_{\rm He} \approx 10^{9.3}$; Shen & Bildsten, 2009). Most of this energy is used to lift the electron degeneracy in the core, meaning that very little, if any, makes its way to the surface of the star. These subtle surface effects, coupled with the fact that the Kelvin–Helmholtz contraction following the initial flash occurs over a mere 10^4 years (Thomas, 1967), the event has yet to be observationally proven. Because of this, accurate stellar models covering the physical conditions and processes present during this phase are vital to the understanding of this evolutionary stage.

The overall aim of this research was to derive search criteria for future targeted observations that will aid in identification of low–mass stars immediately preceding and following helium–core ignition, as well as guide expectations regarding the type of HeF star most likely to be detectable. This was achieved by combining stellar evolution information on these very rapid phases, both through modelling stellar population distributions, and analysis of existing variable star observational data.

Predicted observational signatures of stars just prior to their helium–core ignition were determined in Chapters 2 and 3. As a foundational step, biases inherent in red giant age and metallicity distributions were studied and correction factors derived from synthetic stellar populations, based on PARSEC isochrones. Although not the final goal here, these preliminary results have immediate applications, as detailed in Manning & Cole (2017). These corrections to spectroscopic samples provide details on over– and under–represented red giant populations, depending on age and metallicity. Kirby et al. (2017) postulated that when these biases are

corrected for, galactic chemical evolution history can be significantly different, as shown in the case of the Local Group dwarf galaxy Leo A. The key finding of Manning & Cole (2017, see also Chapter 2) was that a sample of RGB stars taken from a mixed population will preferentially include younger stars over older populations, leading to the latter being under–represented. Low–metallicity stars are more likely to be observed at a given age, but affect sampled populations to a lesser degree than age.

Building on these findings, Chapter 3 focussed on red giant evolution immediately preceding the initial HeF and the subsequent evolution time through the CFP. Stellar population data from the simulated CMDs were combined with data from MESA evolutionary tracks, following the star from TRGB to ZAHB. These results show that higher metallicity is indicative of longer CFP lifetimes, and with the exception of younger stars (1–2 Gyr), these times do not vary significantly with age. This is advantageous since stellar metallicity is often easier to determine than age. The CFP evolution times derived here agree with past studies by Despain (1981); Sweigart (1994); Brown et al. (2001); Paxton et al. (2011), and align well with the generally accepted standard of $\sim$ 2 Myr. However, despite the general consensus being that the HeF process is almost independent of both total mass and metallicity (Thomas, 1967; Serenelli & Weiss, 2005; Bildsten et al., 2012), these results indicate that this is not necessarily the case.

If the age (mass) and the metallicity of red giants can be reliably determined, the colour–magnitude coordinates of the TRGB presented in Chapter 3 provide a method of identifying stars that may soon experience their initial HeF, commencing their rapid journey back down the RGB. The morphologies of stellar evolution tracks provide information on the position and length of the HB (or red clump) for each age and metallicity, guiding expectations of overlap between CFP stars and those in surrounding evolutionary stages. Thus, in some cases the HeF candidates may be more obviously separated from their quiescent–burning counterparts.

Stars evolving through the CFP may be expected to cross the instability strip before they settle on the HB. Due to this, variable stars with changing periodicity could be indicative of this rapid evolution stage. The results from Chapter 3 indicate that for a given total stellar mass, a relatively young, low–metallicity population would yield the highest chance of observing a CFP star. However, the assertion that the downward evolution is largely hydrostatic (Thomas, 1967; Deupree, 1996; Serenelli & Weiss, 2005; Paxton et al., 2011) and closely follows

the RGB, suggests that the star will be too red to become a radial pulsator until very close to its ZAHB position. Only the very old, low–metallicity populations, which are already known to populate the instability strip at low–mass when core helium–burning (RR Lyrae and Type II Cepheids), are likely to cross the instability strip during the CFP phase.

Chapter 4 presented period analysis of SMC RR Lyrae and BL Herculis (Type II Cepheids) variables in the OGLE-III catalogue. A generalised Lomb–Scargle technique was used to determine changes in the periodicity over the entire observation interval of each star, accounting for both measurement uncertainty and statistical fluctuations in sampled data due to survey cadence. Since the sample of RR Lyrae stars used here was almost (only ∼9% excluded), the changes in periodicity derived here can also be applied to other areas in future research.

Based on past evolutionary simulations of the CFP, stars exhibiting negative rates of period change, located towards the HB, were selected as highly possible post–HeF candidates (Silva Aguirre et al., 2008; Catelan, 2009). Stars exhibiting positive and variable change rates, located between the RGB and HB, were also identified, but are less likely to be in their CFP according to (Silva Aguirre et al., 2008), reporting $\sim 76\%$ of pre–ZAHB variables to have negative $\dot{P}$ values.

Unfortunately, no variables with changing periodicity were identified near the TRGB (see Kiss & Bedding, 2003, for a study of pulsating stars in the LMC below the TRGB), however three stars stood out from the main group overlaying the HB. These three could be perceived as being on their way to the ZAHB, descending the RGB following their main HeF, two of which showed both positive and negative rates of period change, while the remaining just exhibited lengthening of their periods. Although Silva Aguirre et al. (2008) reported that the majority of CFP stars crossing the instability strip will exhibit negative period change rates, positive ones are still possible.

Ten variables with negative rates of period change, closely aligning with the HB, were isolated as highly possible CFP stars. However, there are also other plausible explanations for this variability, such as fast–evolving binary pulsators (see Pietrzyński et al., 2012; Soszyński et al., 2016), or due to the mysterious Blažko effect (Blažko, 1907), or caused by small random mixing events brought on by the redistribution of elements in the cores of HB stars (Sweigart & Renzini, 1979). Despite of these possibilities, the location of the ten selected stars in colour–magnitude space still indicates a likely explanation is that they are pre–ZAHB.

5.1 Future Work

This research provides a foundation for future targeted searches in the quest to find observational evidence of the HeF and subsequent subflashes. Currently, there are only theoretical models in this space. Combining the TRGB coordinates and CFP evolution times derived here with results from other areas of study, such as asteroseismology, has the potential to provide highly detailed observational criteria immediately pre– and post–HeF. Additionally, the discovery that higher metallicity populations of intermediate–age to old red giants have the longest CFP evolution time, and so are more likely to be undergoing subflashes than other populations of low–mass stars, may further influence future search criteria.

The late–CFP (pre–ZAHB) candidates presented here, should form the basis of follow up observations, collecting both continuous photometric data, and spectroscopic data in the hopes proving their stellar evolution status, or at least ruling out other mechanisms driving the changes in periodicity (such as fast–evolving binary systems). There are currently a number of extensive, continuous spectroscopic surveys producing enormous catalogues that could be used for this purpose, including the GALAH survey (GALactic Archaeology with Hermes; De Silva et al., 2015) in the Southern Hemisphere, the LAMOST survey (Large Sky Area Multi–Object Fibre Spectroscopic Telescope; Luo et al., 2015) in the Northern Hemisphere, and 4MOST (4 m Multi–Object Spectroscopic Telescope; de Jong et al., 2012) also in the Southern Hemisphere. These catalogues should provide an initial data source for follow–up analysis of the variables listed here.

The results here represent a significant advancement in the quest for observational evidence of this rapid, yet violent core helium–burning stage, forming the foundation of future efforts in this area.

Appendix A

Simulated Colour–Magnitude Diagrams

The 42 synthetic CMDs of red giant star population densities derived from PARSEC isochrones (see Chapter 2 for details). The legend shown applies to every plot. The red horizontal line in each plot represents the individual BL and HB colour-cutoff determined for each simulation, where possible. The red parabola is the cutoff between AGB and RGB stars. The younger and older isochrones represent the younger and older age limits.

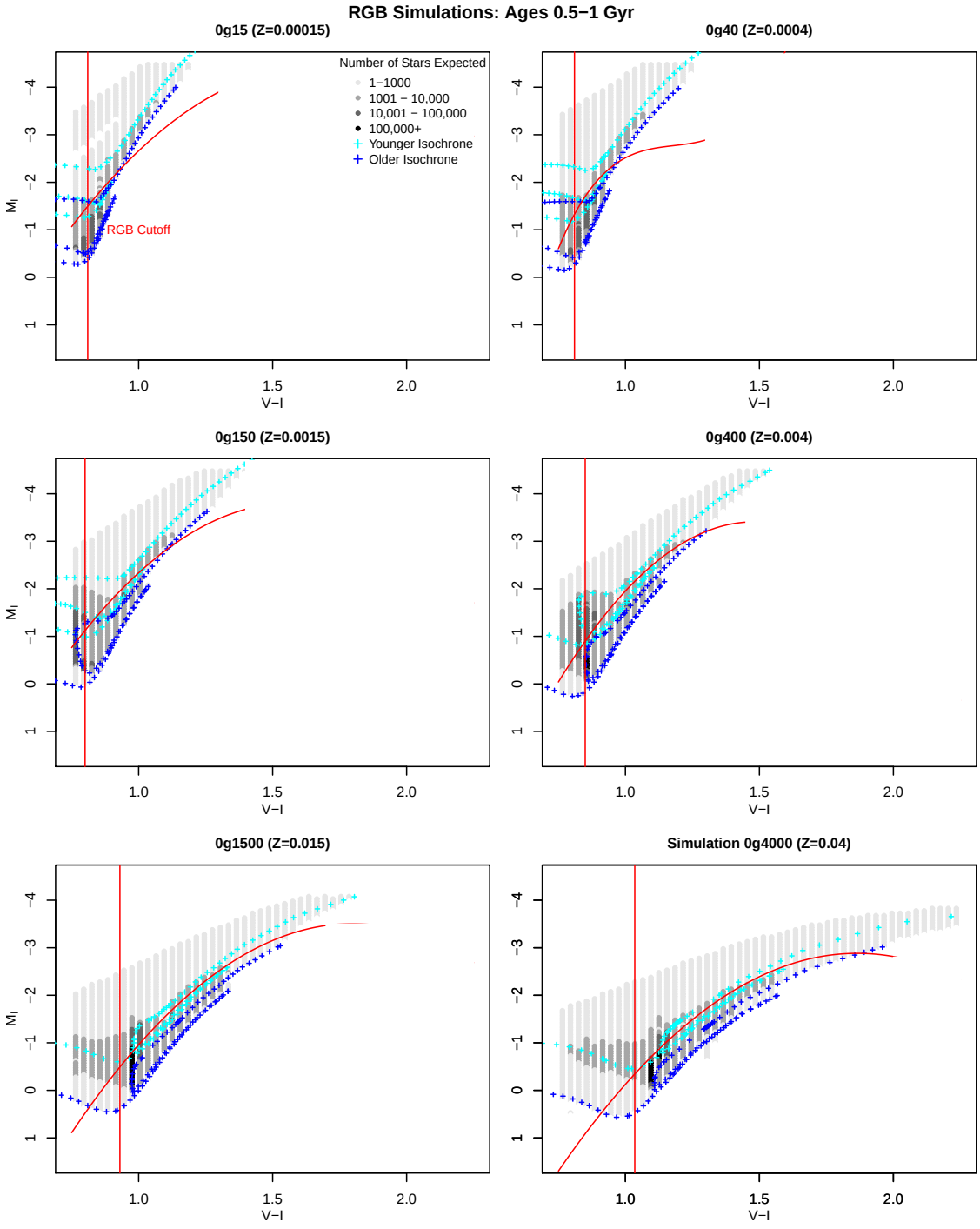
RGB Simulations: Ages 0.5−1 Gyr
0g15 (Z=0.00015)
0g40 (Z=0.0004)
0g150 (Z=0.0015)
0g400 (Z=0.004)
0g1500 (Z=0.015)
Simulation 0g4000 (Z=0.04)
Number of Stars Expected
1−1000
1001 − 10,000
10,001 − 100,000
100,000+
Younger Isochrone
Older Isochrone
RGB Cutoff
M_I
V−I

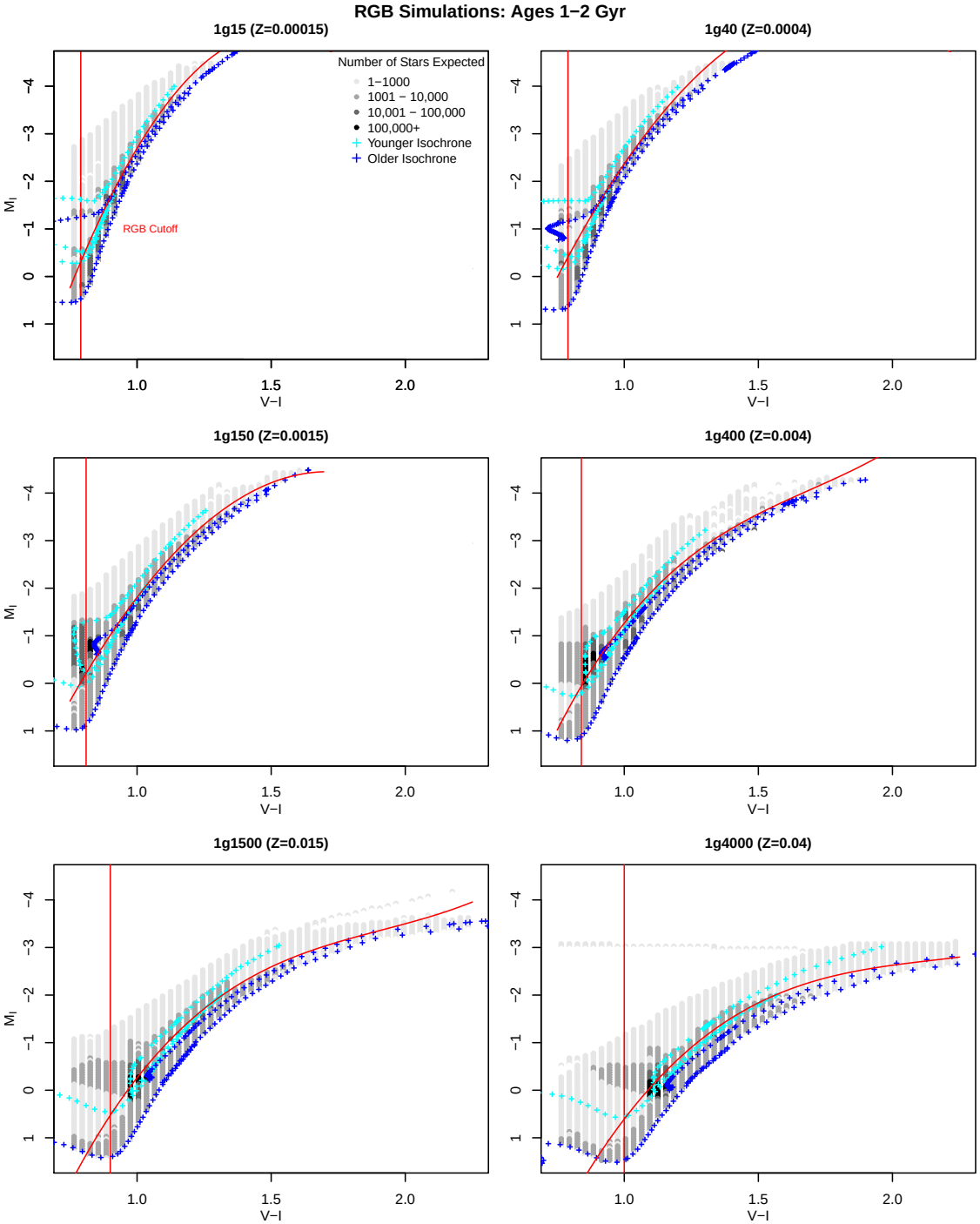
RGB Simulations: Ages 1−2 Gyr
1g15 (Z=0.00015)
1g40 (Z=0.0004)
1g150 (Z=0.0015)
1g400 (Z=0.004)
1g1500 (Z=0.015)
1g4000 (Z=0.04)
Number of Stars Expected
1−1000
1001 − 10,000
10,001 − 100,000
100,000+
Younger Isochrone
Older Isochrone
RGB Cutoff
M_I
V−I

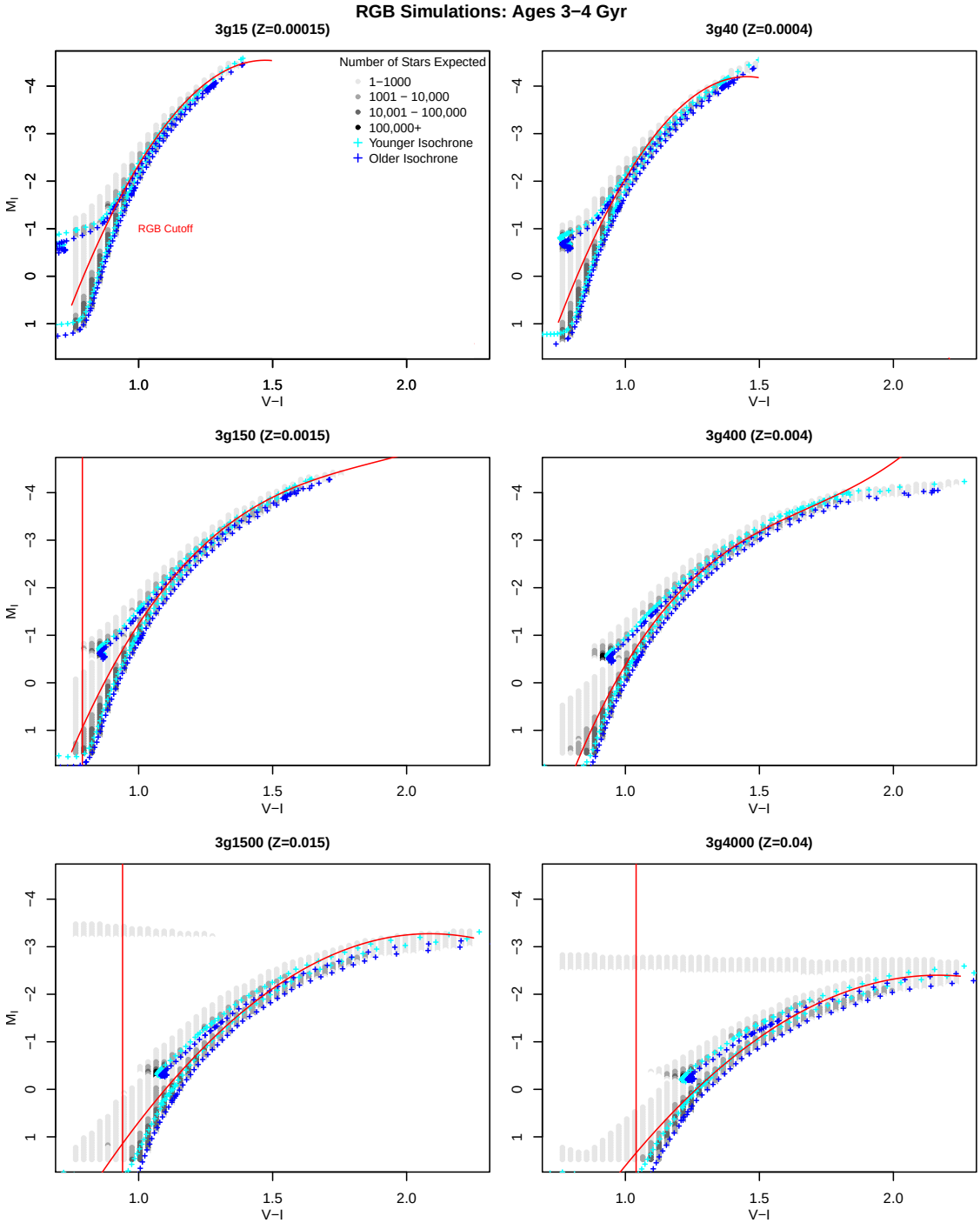
RGB Simulations: Ages 3−4 Gyr
3g15 (Z=0.00015)
3g40 (Z=0.0004)
3g150 (Z=0.0015)
3g400 (Z=0.004)
3g1500 (Z=0.015)
3g4000 (Z=0.04)
Number of Stars Expected
1−1000
1001 − 10,000
10,001 − 100,000
100,000+
Younger Isochrone
Older Isochrone
RGB Cutoff
M_I
V−I

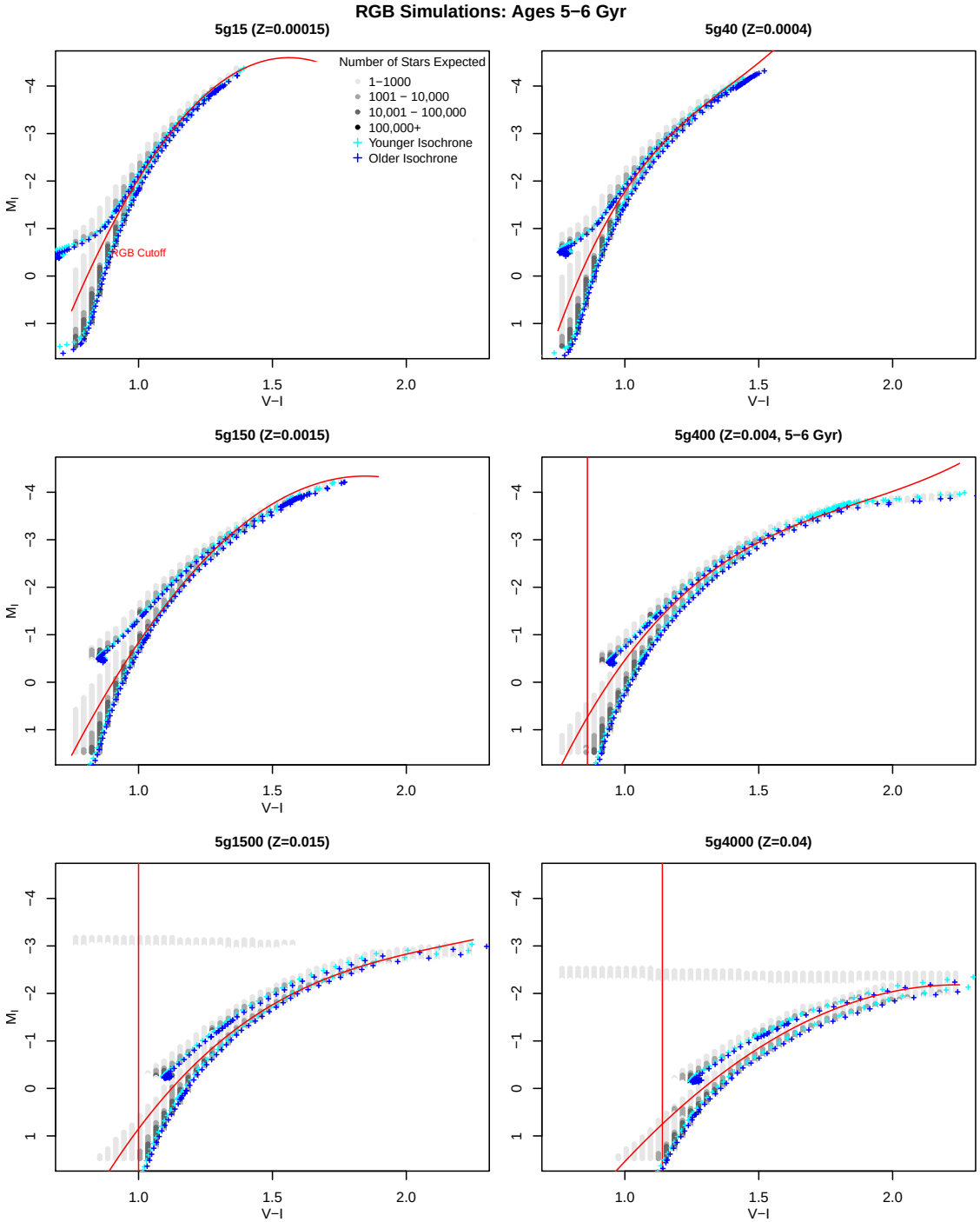
RGB Simulations: Ages 5−6 Gyr
5g15 (Z=0.00015)
5g40 (Z=0.0004)
5g150 (Z=0.0015)
5g400 (Z=0.004, 5−6 Gyr)
5g1500 (Z=0.015)
5g4000 (Z=0.04)
Number of Stars Expected
1−1000
1001 − 10,000
10,001 − 100,000
100,000+
Younger Isochrone
Older Isochrone
RGB Cutoff
M_I
V−I
1.0
1.5
2.0
−4
−3
−2
−1
0
1

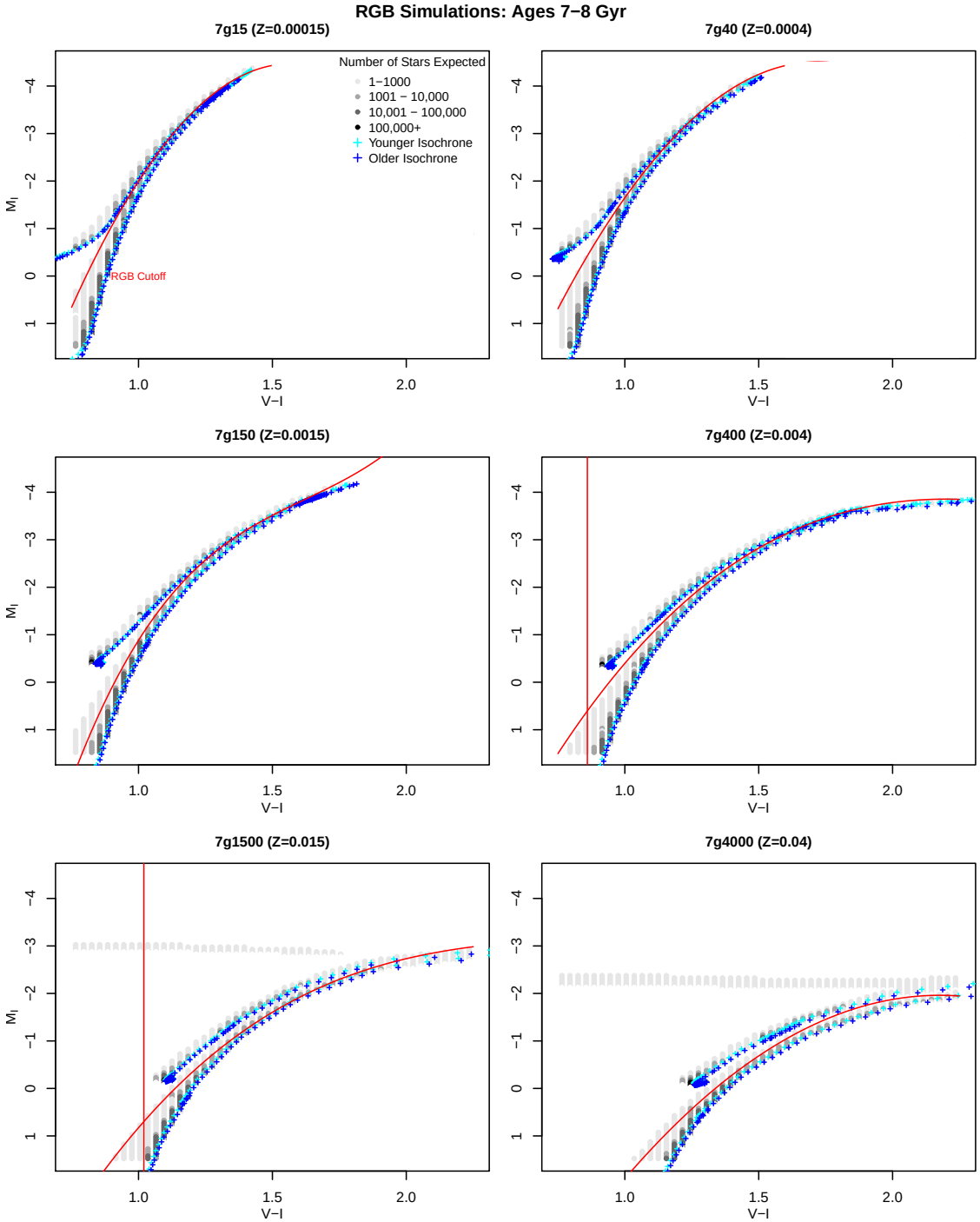
RGB Simulations: Ages 7−8 Gyr
7g15 (Z=0.00015)
7g40 (Z=0.0004)
7g150 (Z=0.0015)
7g400 (Z=0.004)
7g1500 (Z=0.015)
7g4000 (Z=0.04)
Number of Stars Expected
1−1000
1001 − 10,000
10,001 − 100,000
100,000+
Younger Isochrone
Older Isochrone
RGB Cutoff
M_I
V−I

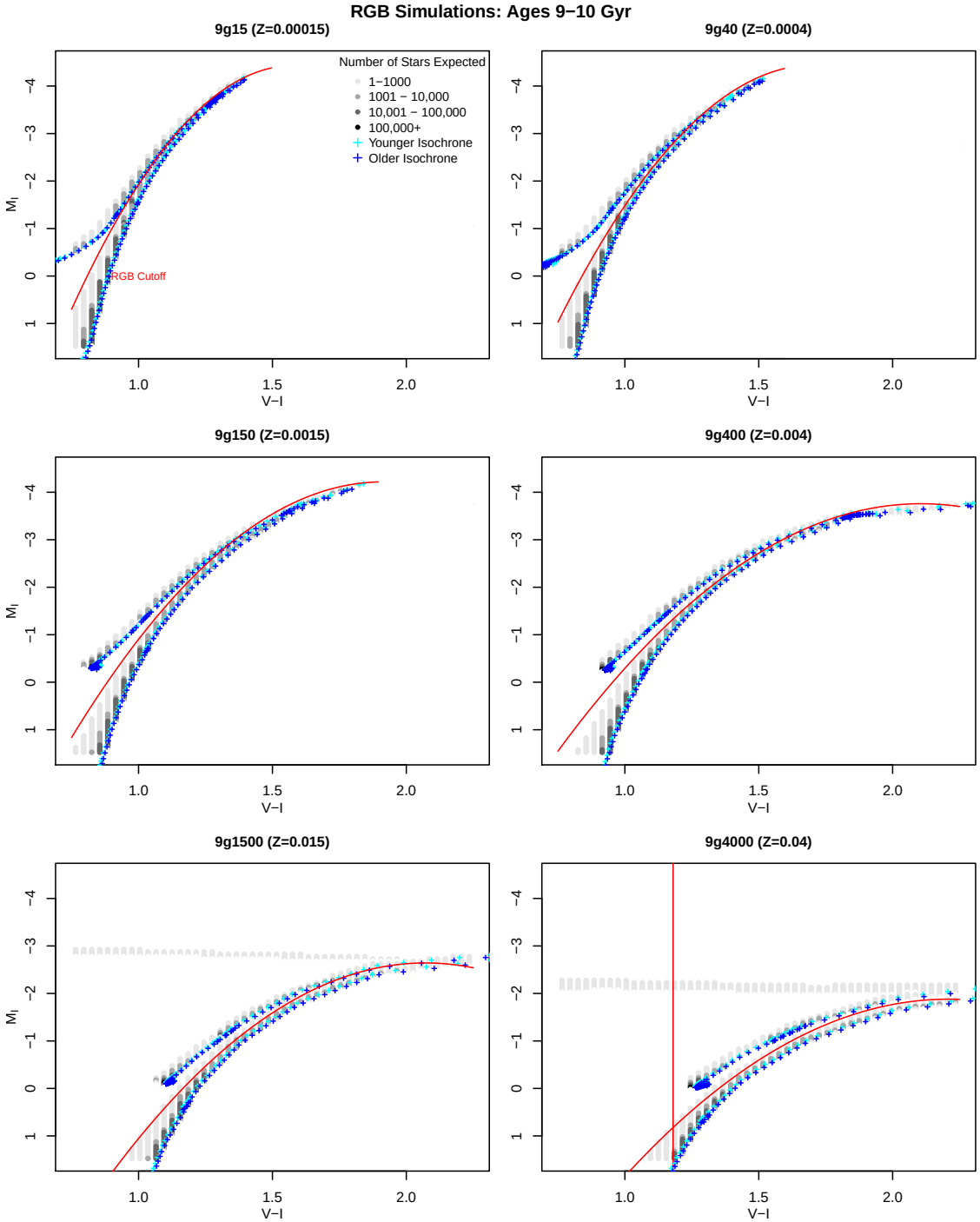
RGB Simulations: Ages 9−10 Gyr
9g15 (Z=0.00015)
9g40 (Z=0.0004)
9g150 (Z=0.0015)
9g400 (Z=0.004)
9g1500 (Z=0.015)
9g4000 (Z=0.04)
Number of Stars Expected
1−1000
1001 − 10,000
10,001 − 100,000
100,000+
Younger Isochrone
Older Isochrone
RGB Cutoff
M_I
V−I
1.0
1.5
2.0
−4
−3
−2
−1
0
1

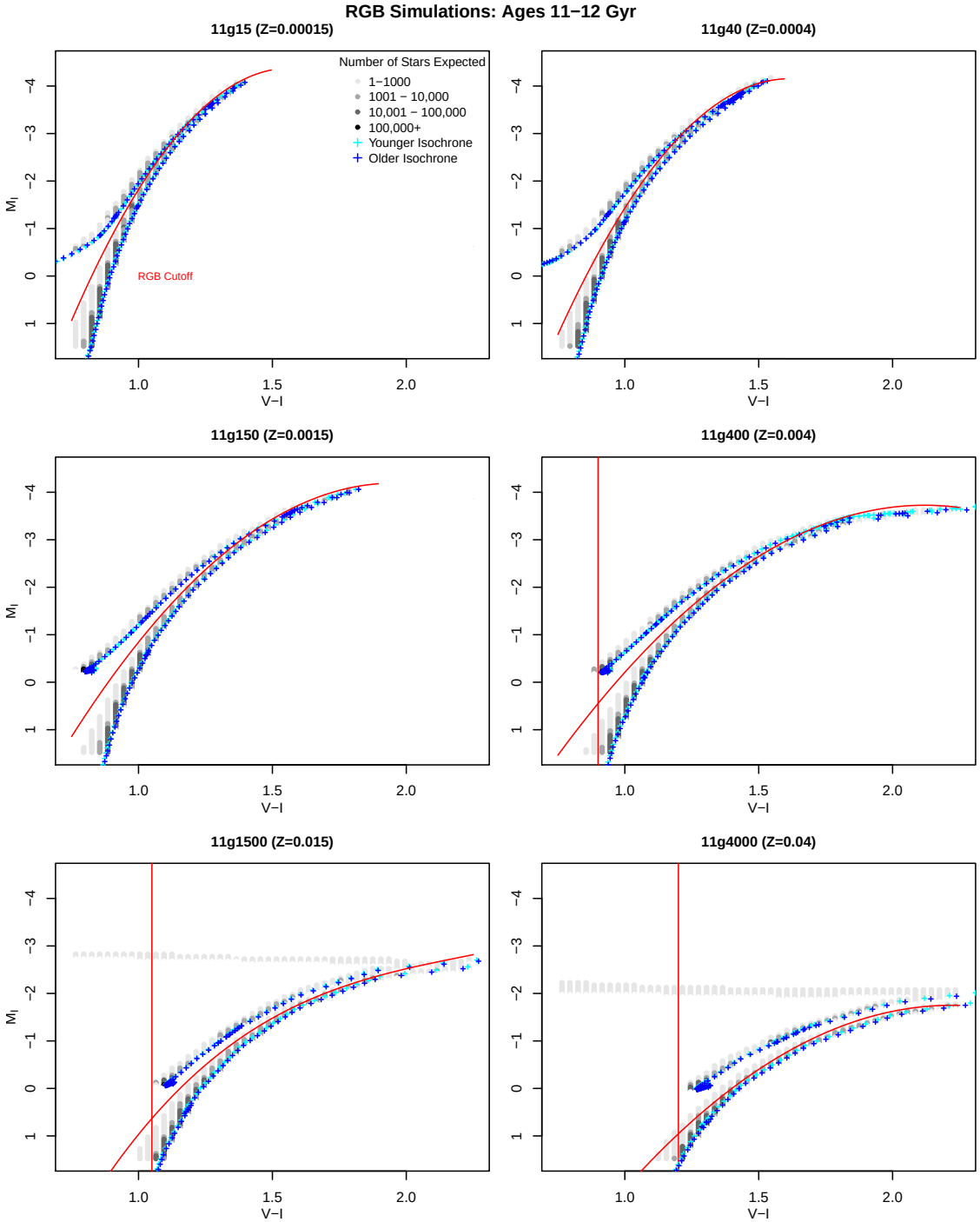
RGB Simulations: Ages 11−12 Gyr
11g15 (Z=0.00015)
11g40 (Z=0.0004)
11g150 (Z=0.0015)
11g400 (Z=0.004)
11g1500 (Z=0.015)
11g4000 (Z=0.04)
Number of Stars Expected
1−1000
1001 − 10,000
10,001 − 100,000
100,000+
Younger Isochrone
Older Isochrone
RGB Cutoff
M_I
V−I

Appendix B

Age–Metallicity Bias Correction Factors

Normalised age–metallicity bias correction factors as calculated from simulated colour–magnitude space (see Chapter 2). Values are given for two separate magnitude ranges, comparing distributions of entire stellar populations with selections of only red giant branch (RGB) stars.

	0.5–1 Gyr	**1–2 Gyr**	**3–4 Gyr**	**5–6 Gyr**
0.00015	0.433	0.810	0.801	0.629
0.0004	0.438	0.815	0.829	0.636
0.0015	0.427	0.810	0.814	0.587
0.004	0.364	1.00	0.710	0.501
0.015	0.269	0.357	0.353	0.213
0.04	0.234	0.120	0.105	0.000

	7–8 Gyr	**9–10 Gyr**	**11–12 Gyr**
0.00015	0.629	0.490	0.436
0.0004	0.540	0.489	0.432
0.0015	0.501	0.454	0.394
0.004	0.409	0.359	0.306
0.015	0.148	0.119	0.024
0.04	0.000	0.000	0.000

Table B.1: Normalised age–metallicity correction factors for entire stellar population over the magnitude range $-4.5 \leq M_I \leq -2.5$.

	0.5–1 Gyr	**1–2 Gyr**	**3–4 Gyr**	**5–6 Gyr**
0.00015	0.092	0.207	0.350	0.383
0.0004	0.133	0.195	0.613	0.518
0.0015	0.157	0.231	0.730	0.550
0.004	0.535	0.922	0.710	0.525
0.015	0.161	1.00	0.643	0.477
0.04	0.081	0.929	0.488	0.432

	7–8 Gyr	**9–10 Gyr**	**11–12 Gyr**
0.00015	0.383	0.347	0.319
0.0004	0.410	0.351	0.313
0.0015	0.489	0.456	0.408
0.004	0.464	0.438	0.394
0.015	0.397	0.385	0.353
0.04	0.402	0.332	0.316

Table B.2: Normalised age–metallicity correction factors for entire stellar population over the magnitude range $-2.5 \leq M_I \leq 1.5$.

	0.5–1 Gyr	**1–2 Gyr**	**3–4 Gyr**	**5–6 Gyr**
0.00015	0.222	0.915	0.966	0.757
0.0004	0.1734	0.839	1.00	0.767
0.0015	0.106	0.727	0.967	0.683
0.004	0.098	0.447	0.633	0.396
0.015	0.050	0.198	0.284	0.138
0.04	0.074	0.009	0.000	0.000

	7–8 Gyr	**9–10 Gyr**	**11–12 Gyr**
0.00015	0.752	0.592	0.527
0.0004	0.649	0.569	0.518
0.0015	0.503	0.430	0.407
0.004	0.344	0.305	0.296
0.015	0.098	0.061	0.029
0.04	0.000	0.000	0.000

Table B.3: Normalised age–metallicity correction factors for only RGB stars over the magnitude range $-4.5 \leq M_I \leq -2.5$.

	0.5–1 Gyr	**1–2 Gyr**	**3–4 Gyr**	**5–6 Gyr**
0.00015	0.128	0.290	0.486	0.537
0.0004	0.189	0.258	0.587	0.546
0.0015	0.210	0.293	0.600	0.535
0.004	0.654	0.773	0.670	0.499
0.015	0.167	1.00	0.525	0.415
0.04	0.074	0.587	0.300	0.333

	7–8 Gyr	**9–10 Gyr**	**11–12 Gyr**
0.00015	0.535	0.490	0.450
0.0004	0.496	0.479	0.435
0.0015	0.483	0.455	0.411
0.004	0.447	0.420	0.385
0.015	0.347	0.346	0.324
0.04	0.317	0.246	0.254

Table B.4: Normalised age–metallicity correction factors for only RGB stars over the magnitude range $-2.5 \leq M_I \leq 1.5$.

Appendix C

Comparison of PARSEC and MIST Simulations

The 36 synthetic CMDs of red giant star population densities derived from PARSEC isochrones (see Chapter 2 for details), with the evolutionary tracks from MIST shown in cyan (see Chapter 3 for details). Mass steps of 0.01 $M_{\odot}$ were not sufficient to resolve evolution tracks for the oldest stars (9–12 Gyr) at Z=0.04, as such none are displayed in these cases. The legend shown applies to every plot.

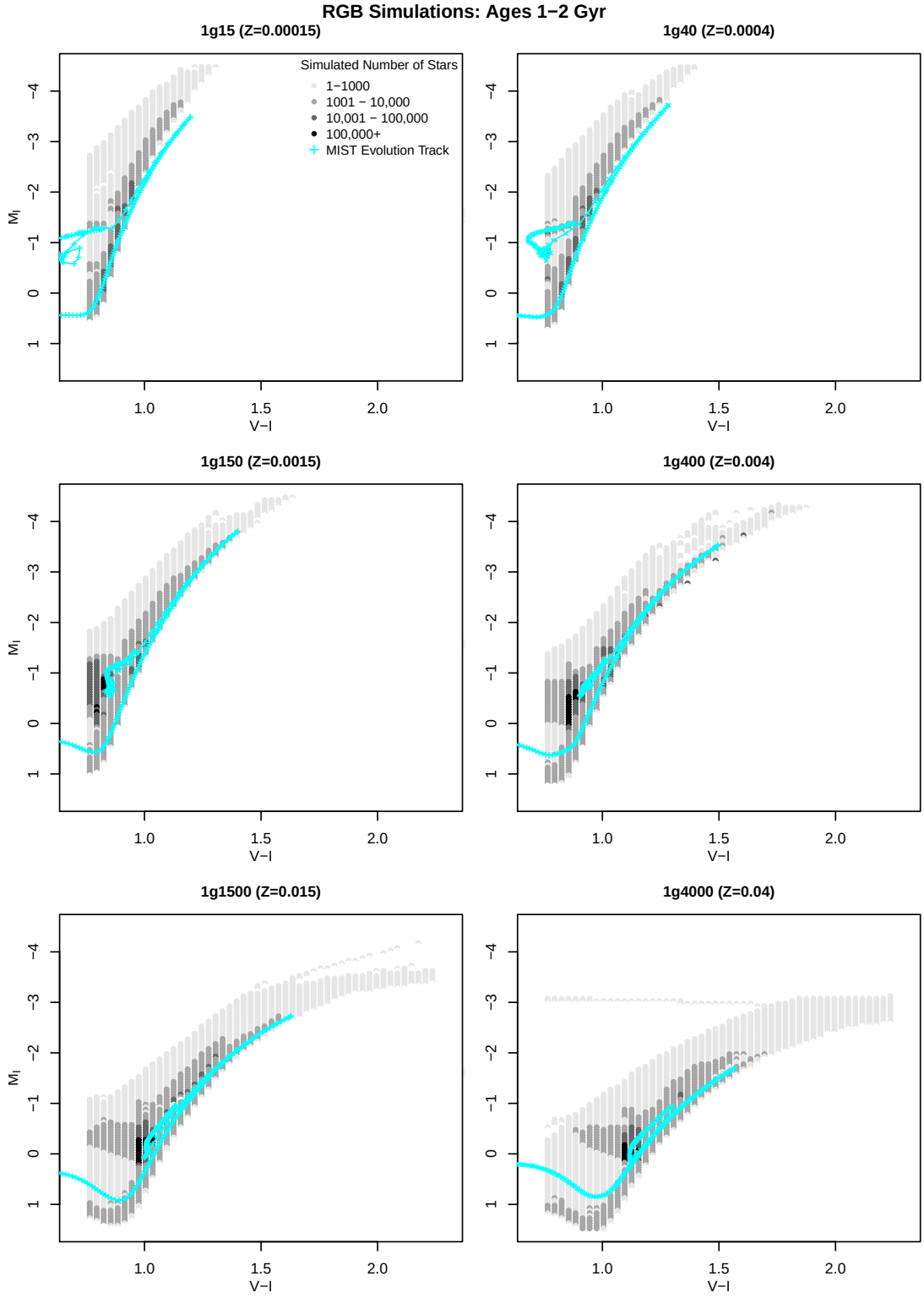
RGB Simulations: Ages 1−2 Gyr
1g15 (Z=0.00015)
1g40 (Z=0.0004)
1g150 (Z=0.0015)
1g400 (Z=0.004)
1g1500 (Z=0.015)
1g4000 (Z=0.04)
Simulated Number of Stars
1−1000
1001 − 10,000
10,001 − 100,000
100,000+
MIST Evolution Track
M_I
V−I
1.0
1.5
2.0
−4
−3
−2
−1
0
1

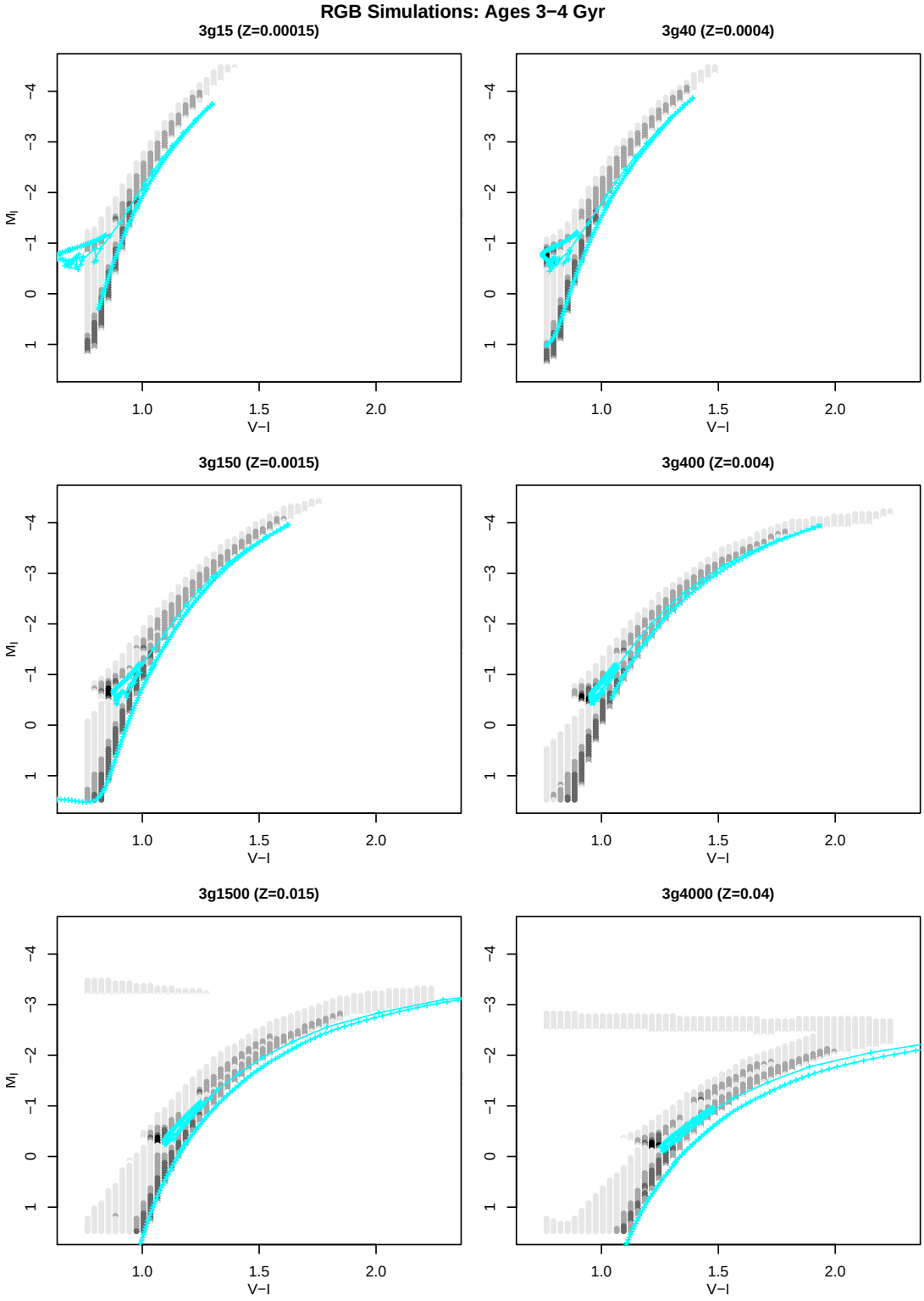
RGB Simulations: Ages 3−4 Gyr
3g15 (Z=0.00015)
3g40 (Z=0.0004)
3g150 (Z=0.0015)
3g400 (Z=0.004)
3g1500 (Z=0.015)
3g4000 (Z=0.04)
M_I
V−I
1.0
1.5
2.0
−4
−3
−2
−1
0
1

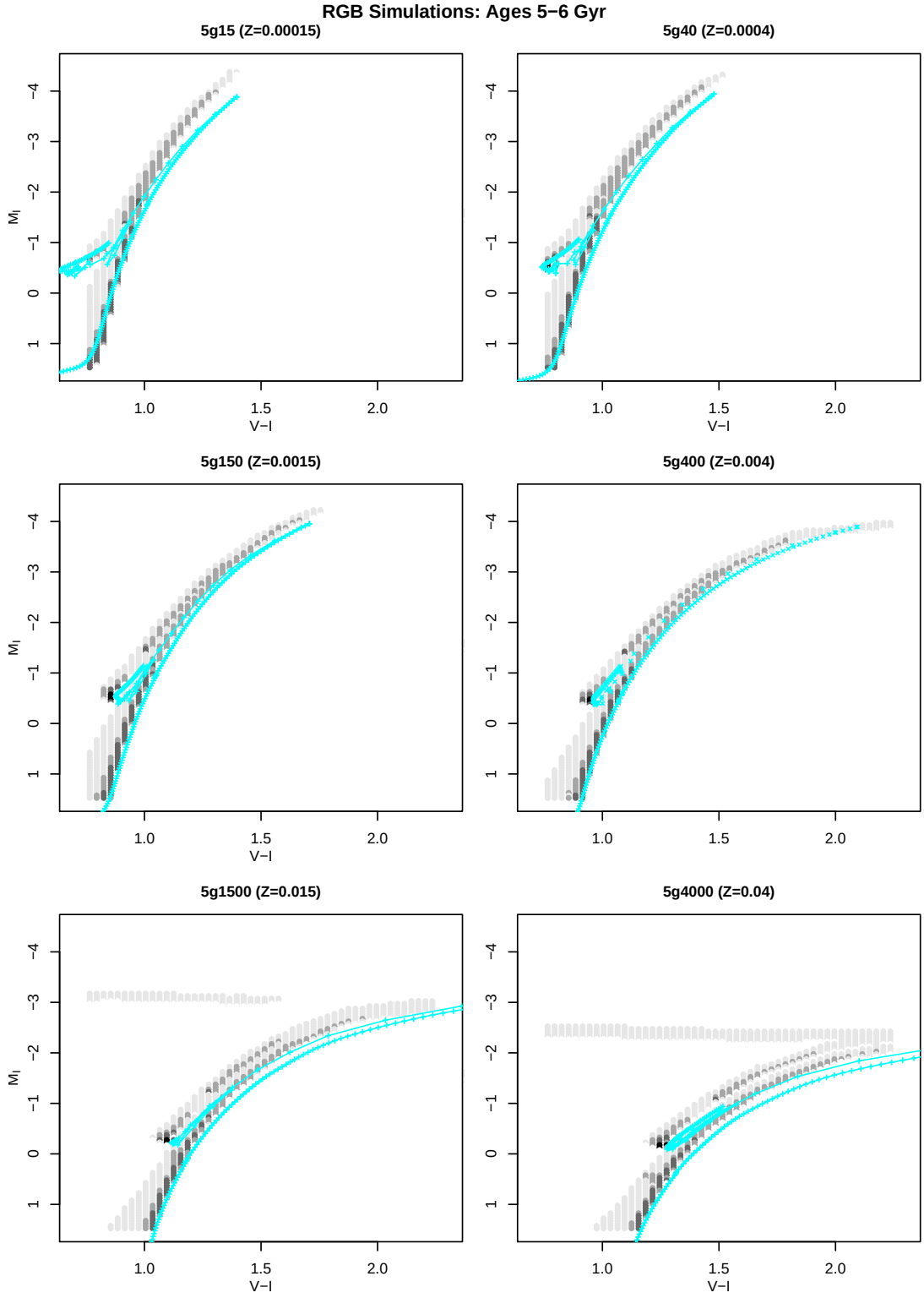
RGB Simulations: Ages 5−6 Gyr
5g15 (Z=0.00015)
5g40 (Z=0.0004)
5g150 (Z=0.0015)
5g400 (Z=0.004)
5g1500 (Z=0.015)
5g4000 (Z=0.04)
M_I
V−I
1.0
1.5
2.0
−4
−3
−2
−1
0
1

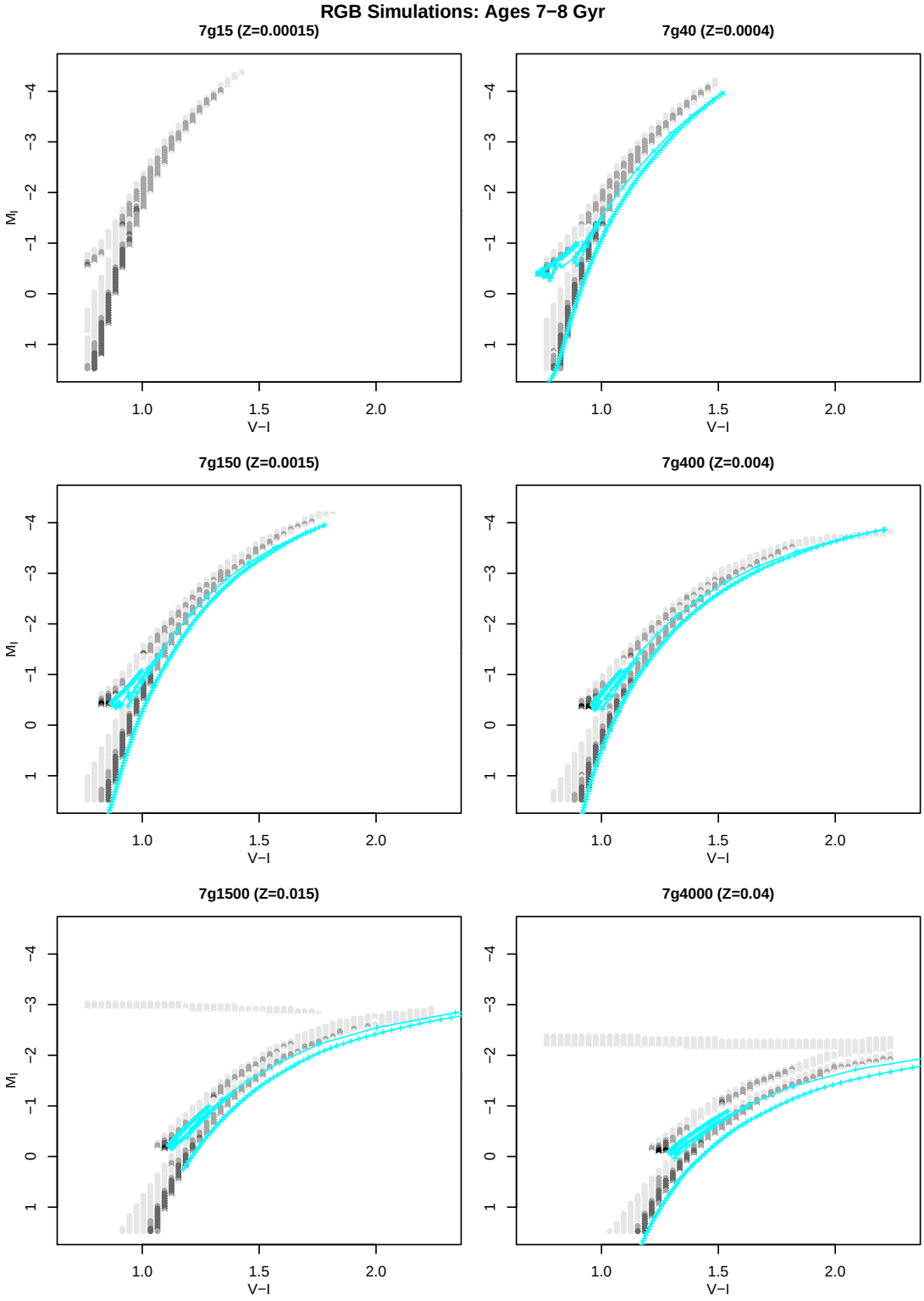
RGB Simulations: Ages 7−8 Gyr
7g15 (Z=0.00015)
7g40 (Z=0.0004)
7g150 (Z=0.0015)
7g400 (Z=0.004)
7g1500 (Z=0.015)
7g4000 (Z=0.04)
M_I
V−I
1.0
1.5
2.0
−4
−3
−2
−1
0
1

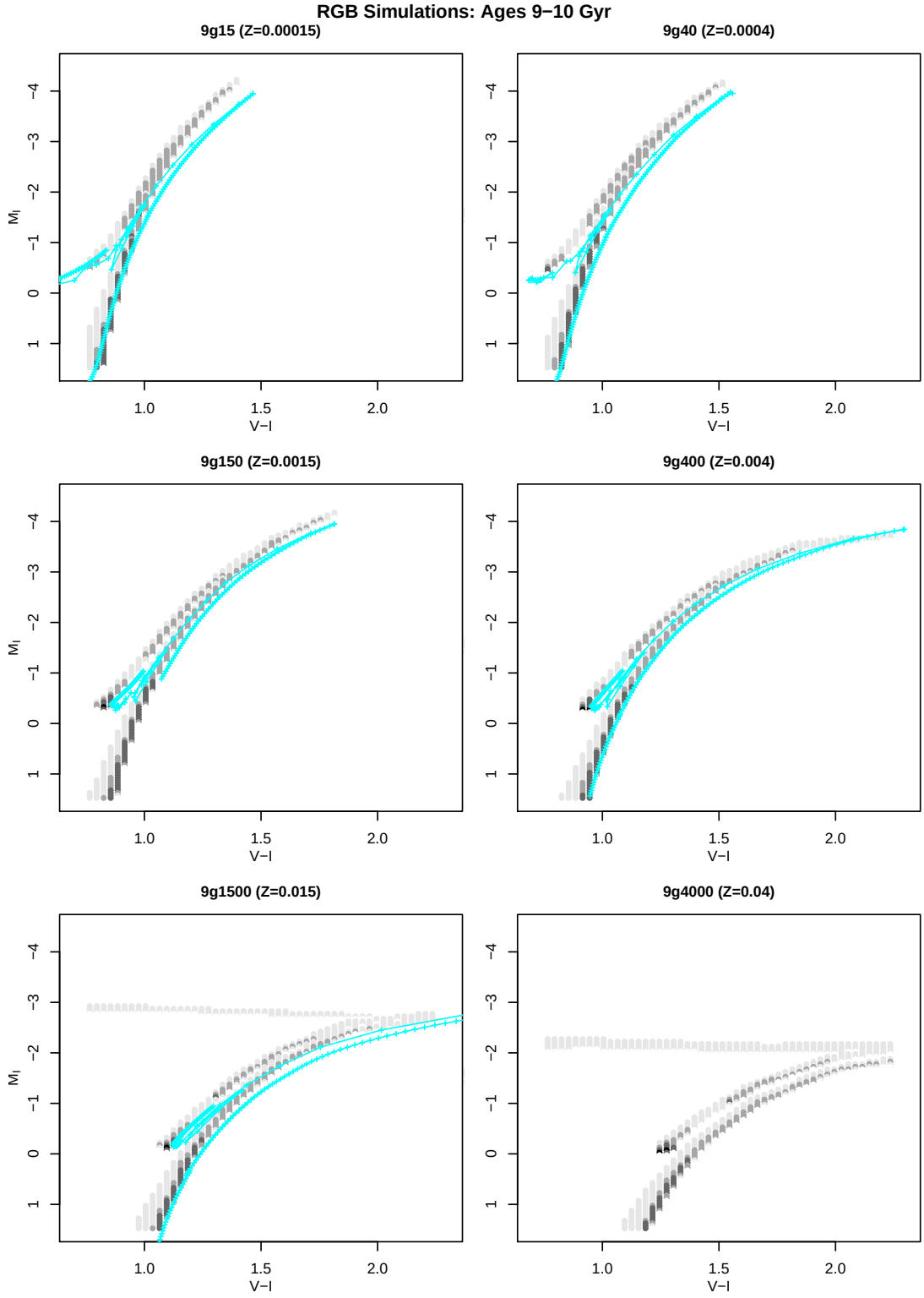
RGB Simulations: Ages 9−10 Gyr
9g15 (Z=0.00015)
9g40 (Z=0.0004)
9g150 (Z=0.0015)
9g400 (Z=0.004)
9g1500 (Z=0.015)
9g4000 (Z=0.04)
M_I
V−I
1.0
1.5
2.0
−4
−3
−2
−1
0
1

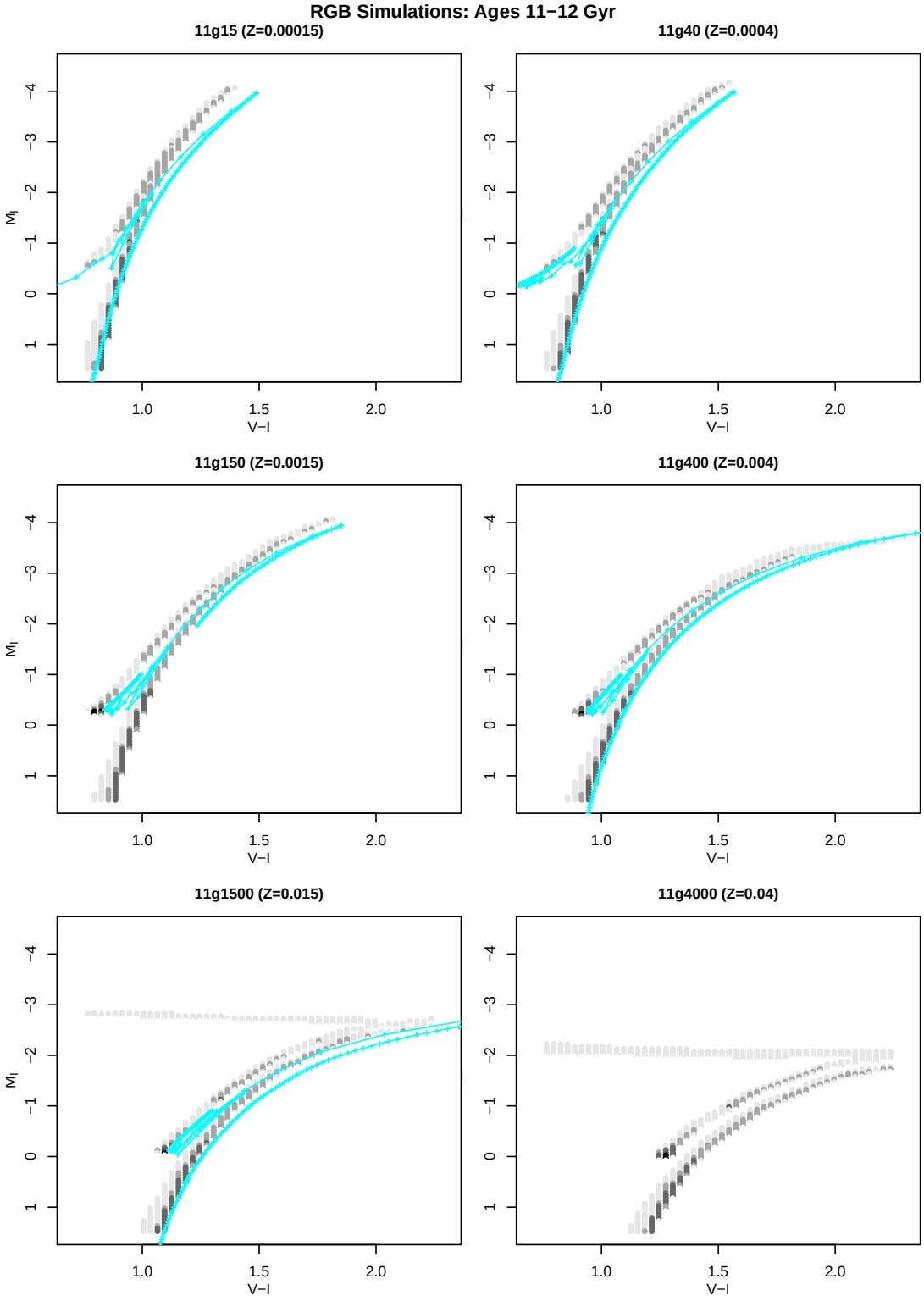
RGB Simulations: Ages 11−12 Gyr
11g15 (Z=0.00015)
11g40 (Z=0.0004)
11g150 (Z=0.0015)
11g400 (Z=0.004)
11g1500 (Z=0.015)
11g4000 (Z=0.04)
M_I
V−I
1.0
1.5
2.0
−4
−3
−2
−1
0
1

Appendix D

Red Giant Branch Tip Coordinates

Colour–magnitude coordinates of the TRGB (just after the initial HeF) derived from PARSEC isochrones and MIST evolutionary tracks, as described in Chapter 3. Due to the large difference between 1 and 2 Gyr values, these have been split into separate groups. These data are plotted in Figure 3.3.

	0.00015	**0.0004**
1 Gyr	(0.911,-1.692)±(0.015,0.025)	(0.940,-1.819)±(0.015,0.025)
2 Gyr	(1.191,-3.845)±(0.015,0.025)	(1.293,-3.949)±(0.015,0.025)
3–4 Gyr	(1.267,-3.977)±(0.029,0.031)	(1.389,-4.067)±(0.031,0.026)
5–6 Gyr	(1.314,-4.013)±(0.023,0.034)	(1.439,-4.075)±(0.025,0.029)
7–8 Gyr	(1.351,-4.046)±(0.021,0.030)	(1.477,-4.093)±(0.022,0.028)
9–10 Gyr	(1.375,-4.064)±(0.021,0.029)	(1.375,-4.101)±(0.023,0.027)
11–12 Gyr	(1.394,-4.075)±(0.019,0.027)	(1.528,-4.106)±(0.019,0.026)
	0.0015	**0.004**
1 Gyr	(1.036,-2.048)±(0.015,0.025)	(1.127,-2.031)±(0.015,0.025)
2 Gyr	(1.482,-3.970)±(0.015,0.025)	(1.717,-3.919)±(0.015,0.025)
3–4 Gyr	(1.612,-4.096)±(0.042,0.031)	(2.063,-4.022)±(0.096,0.049)
5–6 Gyr	(1.691,-4.075)±(0.030,0.027)	(2.291,-3.948)±(0.056,0.037)
7–8 Gyr	(1.748,-4.068)±(0.025,0.026)	(2.457,-3.901)±(0.045,0.033)
9–10 Gyr	(1.788,-4.064)±(0.024,0.026)	(2.573,-3.863)±(0.047,0.039)
11–12 Gyr	(1.817,-4.061)±(0.021,0.026)	(1.817,-3.814)±(0.036,0.035)
	0.015	**0.04**
1 Gyr	(1.334,-2.086)±(0.015,0.025)	(1.566,-1.994)±(0.015,0.025)
2 Gyr	(2.529,-3.567)±(0.015,0.025)	(2.953,-2.918)±(0.015,0.025)
3–4 Gyr	(3.56,-3.35)±(0.20,0.12)	(4.48,-2.595)±(0.21,0.088)
5–6 Gyr	(3.984,-3.081)±(0.074,0.069)	(4.991,-2.409)±(0.060,0.049)
7–8 Gyr	(4.211,-2.918)±(0.057,0.054)	(5.165,-2.313)±(0.053,0.043)
9–10 Gyr	(4.355,-2.821)±(0.049,0.048)	(5.301,-2.247)±(0.049,0.041)
11–12 Gyr	(4.466,-2.749)±(0.036,0.039)	(5.414,-2.200)±(0.037,0.031)

Table D.1: Colour–magnitude coordinates of the TRGB derived from PARSEC isochrones.

	0.00015	**0.0004**
1–1.5 Gyr	(1.059,-2.887)±(0.018,0.010)	(1.228,-3.576)±(0.041,0.023)
1.5–2 Gyr	(1.168,-3.376)±(0.040,0.022)	(1.294,-3.722)±(0.041,0.023)
3–4 Gyr	(1.294,-3.726)±(0.040,0.023)	(1.385,-3.842)±(0.039,0.022)
5–6 Gyr	(1.390,-3.867)±(0.038,0.022)	(1.474,-3.922)±(0.037,0.022)
7–8 Gyr	(1.437,-3.911)±(0.037,0.022)	(1.506,-3.942)±(0.037,0.021)
9–10 Gyr	(1.460,-3.927)±(0.038,0.022)	(1.543,-3.958)±(0.037,0.021)
11–12 Gyr	(1.482,-3.941)±(0.038,0.022)	(1.557,-3.963)±(0.037,0.022)
	0.0015	**0.004**
1–1.5 Gyr	(1.424,-3.840)±(0.038,0.022)	(1.539,-3.637)±(0.054,0.044)
1.5–2 Gyr	(1.442,-3.881)±(0.046,0.031)	(1.765,-3.928)±(0.027,0.020)
3–4 Gyr	(1.628,-3.935)±(0.033,0.021)	(1.958,-3.908)±(0.053,0.019)
5–6 Gyr	(1.699,-3.935)±(0.031,0.020)	(2.078,-3.874)±(0.050,0.019)
7–8 Gyr	(1.768,-3.932)±(0.030,0.020)	(2.191,-3.847)±(0.054,0.018)
9–10 Gyr	(1.805,-3.929)±(0.030,0.020)	(2.289,-3.822)±(0.057,0.017)
11–12 Gyr	(1.831,-3.905)±(0.060,0.041)	(2.366,-3.803)±(0.059,0.017)
	0.015	**0.04**
1–1.5 Gyr	(1.847,-3.033)±(0.016,0.012)	(2.398,-2.675)±(0.014,0.011)
1.5–2 Gyr	(2.632,-3.588)±(0.030,0.011)	(3.222,-2.866)±(0.026,0.001)
3–4 Gyr	(3.547,-3.418)±(0.009,0.006)	(4.461,-2.306)±(0.036,0.009)
5–6 Gyr	(3.890,-3.216)±(0.004,0.001)	(4.590,-2.064)±(0.032,0.009)
7–8 Gyr	(4.004,-3.125)±(0.003,0.002)	(4.645,-1.915)±(0.007,0.002)
9–10 Gyr	(4.157,-2.995)±(0.006,0.005)	*5.188,-1.779*
11–12 Gyr	(4.259,-2.903)±(0.015,0.007)	*5.412,-1.677*

Table D.2: Colour–magnitude coordinates of the TRGB derived from MIST evolution tracks. Mass steps of 0.01 $M_\odot$ were not sufficient to resolve evolution tracks for the oldest stars at Z=0.04 (shown in italics); the values given were interpolated.

Appendix E

Changes in Periodicity

Periods and period change rates ($\dot{P}$) derived using Lomb–Scargle analysis. Cases where both positive and negative rates of change occurred are marked with absolute symbols. The sources are RR Lyrae and BL Herculis Type II Cepheid variables in the Small Magellanic Cloud (SMC) from the OGLE catalogue. The sources all have the prefix OGLE-SMC-RRLYR- except for the last source (OGLE-SMC-T2CEP-27). For further details, see Chapter 4.

OGLE ID #	**Type**	**LSP P [d]**	**LSP $\dot{P}$ [$\times 10^{-9}$ d/d]**	**O–C $\dot{P}$ [$\times 10^{-9}$ d/d]**
0002	RRab	0.59479218	5.62 ± 0.57	
0006	RRab	0.54717844	9.16 ± 0.36	
0007	RRc	0.35453118	-4.02 ± 0.22	
0022	RRab	0.59277425	$\|14.2\| \pm 1.4$	
0023	RRab	0.58802124	-6.72 ± 0.78	
0033	RRab	0.60512794	13.28 ± 0.83	
0038	RRab	0.52308777	$\|57.3\| \pm 1.4$	
0045	RRab	0.51127950	34.0 ± 4.5	
0050	RRc	0.34858199	$\|3.29\| \pm 0.57$	
0056	RRab	0.60018325	-16.97 ± 0.72	
0073	RRd	0.38336018	-7.75 ± 0.21	
0076	RRab	0.66419015	-27.4 ± 2.3	
0086	RRab	0.58218350	15.2 ± 1.9	
0093	RRc	0.37413765	-6.47 ± 0.19	
0102	RRab	0.54425798	22.1 ± 3.9	
0114	RRab	0.63678352	-15.1 ± 1.6	
0120	RRab	0.61777829	8.73 ± 0.73	
0138	RRab	0.65111973	-10.11 ± 0.41	
0142	RRab	0.56216950	220 ± 16	
0148	RRc	0.32900074	-6.44 ± 0.32	
0260	RRab	0.62382724	9.41 ± 0.30	
0285	RRab	0.56372434	-6.49 ± 0.48	
0305	RRab	0.58198559	-13.74 ± 0.28	
0319	RRab	0.52272600	-13.87 ± 0.32	
0348	RRc	0.34983863	$\|27.54\| \pm 0.56$	
0387	RRab	0.63957600	-10.70 ± 0.62	
0392	RRab	0.63079106	6.42 ± 0.43	
0396	RRab	0.58293059	$\|109.1\| \pm 1.1$	$\sim \|110\|$
0411	RRd	0.37299397	2.152 ± 0.044	
0468	RRab	0.58726006	-7.21 ± 0.16	
0486	RRd	0.41089645	-3.61 ± 0.48	
0491	RRd	0.41914323	$\|13.20\| \pm 0.71$	
0498	RRab	0.56428786	-7.39 ± 0.28	
0533	RRab	0.48674863	-16.05 ± 0.51	
0534	RRab	0.59404980	37.91 ± 0.17	
0538	RRab	0.62667438	-7.30 ± 0.53	
0539	RRab	0.63553781	$\|5.51\| \pm 0.41$	
0548	RRd	0.36774018	$\|5.50\| \pm 0.29$	
0550	RRab	0.60829580	6.0 ± 1.3	
0551	RRc	0.34315503	$\|4.40\| \pm 0.21$	
0552	RRab	0.58387226	7.61 ± 0.80	
0562	RRab	0.58039072	$\|24.05\| \pm 0.39$	

OGLE ID #	**Type**	**LSP P [d]**	**LSP $\dot{P}$ [$\times 10^{-9}$ d/d]**	**O–C $\dot{P}$ [$\times 10^{-9}$ d/d]**
0573	RRab	0.60167210	$\|52.3\| \pm 1.5$	
0614	RRab	0.55523380	-4.555 ± 0.072	
0616	RRab	0.58421493	-6.00 ± 0.50	
0617	RRab	0.64832722	13.6 ± 1.8	
0632	RRab	0.55739575	-19.10 ± 0.32	
0666	RRab	0.61896950	5.47 ± 0.75	
0668	RRab	0.57897180	$\|9.14\| \pm 0.53$	
0670	RRab	0.53509547	9.2 ± 1.0	
0694	RRab	0.57270610	21.7 ± 1.0	
0698	RRab	0.58963585	1.601 ± 0.095	
0706	RRab	0.63135438	4.018 ± 0.082	
0714	RRab	0.61630621	$\|12.19\| \pm 0.86$	
0721	RRab	0.61874993	$\|31.6\| \pm 2.6$	
0728	RRab	0.58833310	$\|31.8\| \pm 1.4$	
0757	RRab	0.63173193	$\|16.0\| \pm 1.5$	
0769	RRab	0.56708551	$\|2.03\| \pm 0.21$	
0771	RRab	0.63106073	$\|23.0\| \pm 1.8$	
0776	RRab	0.56791277	$\|38.74\| \pm 0.59$	
0801	RRab	0.64209471		$\sim \|130\|$
0832	RRab	0.58719680	$\|17.87\| \pm 0.71$	
0834	RRab	0.60527201	$\|24.4\| \pm 1.4$	
0850	RRc	0.33608718	$\|29.4\| \pm 26$	
0894	RRc	0.32992724	-5.771 ± 0.079	
0921	RRab	0.55618375	$\|13.78\| \pm 0.35$	
0923	RRab	0.57929435	$\|51.6\| \pm 1.6$	
0965	RRab	0.53561472	$\|5.23\| \pm 0.36$	
0976	RRc	0.37218992	4.46 ± 0.18	
0978	RRc	0.34540109	-9.304 ± 0.051	
1008	RRab	0.64318923	19.53 ± 0.93	
1028	RRd	0.42122300	$\|24.4\| \pm 1.7$	
1042	RRab	0.61229936	7.32 ± 0.54	
1043	RRab	0.61946295	15.27 ± 0.21	
1049	RRab	0.61670003	-5.60 ± 0.31	
1065	RRab	0.56649932	9.874 ± 0.086	
1077	RRab	0.68708283	5.87 ± 0.12	
1089	RRc	0.39377699	-10.72 ± 0.36	
1108	RRab	0.46467746	14.18 ± 0.19	
1127	RRab	0.64551872	-5.573 ± 0.094	
1137	RRc	0.37327458	19.46 ± 0.22	
1156	RRc	0.36423468	8.69 ± 0.11	
1197	RRc	0.33242974	-2.635 ± 0.029	
1199	RRab	0.61144798	8.8 ± 1.1	

OGLE ID #	**Type**	**LSP P [d]**	**LSP $\dot{P}$ [$\times 10^{-9}$ d/d]**	**O–C $\dot{P}$ [$\times 10^{-9}$ d/d]**
1204	RRab	0.51693870	12.35 ± 0.24	
1208	RRab	0.51147007	-5.126 ± 0.057	
1212	RRab	0.59607247	35.2 ± 1.1	
1258	RRab	0.58124421		$\sim \lvert 9.5 \rvert$
1282	RRab	0.60742106	$\lvert 21.9 \rvert \pm 1.3$	
1288	RRd	0.36586433	-5.031 ± -0.085	
1299	RRc	0.34331909	3.300 ± 0.071	
1327	RRc	0.38271132	20.42 ± 0.25	
1353	RRab	0.61583658	13.25 ± 0.23	
1395	RRc	0.34915135	5.210 ± 0.035	
1400	RRab	0.63275493	$\lvert 42.08 \rvert \pm 0.93$	
1404	RRab	0.52176756	-7.63 ± 0.31	
1409	RRab	0.64246724	$\lvert 32.0 \rvert \pm 2.4$	
1423	RRab	0.53820024	8.45 ± 0.21	
1456	RRab	0.52884217	-69.28 ± 0.35	
1466	RRab	0.61400763	13.57 ± 0.31	
1476	RRab	0.43386253	-6.73 ± 0.26	
1477	RRab	0.65347441	$\lvert 69.4 \rvert \pm 1.7$	
1488	RRd	0.37659276	-7.08 ± 0.13	
1489	RRab	0.53677861	-10.44 ± 0.95	
1494	RRab	0.62417278	$\lvert 9.94 \rvert \pm 0.53$	
1496	RRab	0.52477129	$\lvert 18.58 \rvert \pm 0.35$	
1505	RRab	0.62787080	-68.09 ± 0.86	
1511	RRab	0.65866748	-17.6 ± 1.1	
1522	RRab	0.58774990	2.62 ± 0.34	
1525	RRd	0.36045311	-8.64 ± 0.26	
1530	RRab	0.60533232	-24.91 ± 0.33	
1566	RRab	0.56431605		$\sim \lvert 18 \rvert$
1570	RRab	0.61616341	-61.7 ± 1.2	$\sim \lvert 7.1 \rvert$
1576	RRab	0.53045997	-11.30 ± 0.78	
1592	RRab	0.59268173	$\lvert 14.72 \rvert \pm 0.34$	
1598	RRab	0.60569113	12.28 ± 0.30	
1605	RRd	0.38237663	3.273 ± 0.060	
1629	RRd	0.34324601	$\lvert 14.15 \rvert \pm 0.37$	
1644	RRab	0.56727405	-7.56 ± 0.46	
1670	RRab	0.65475476	$\lvert 8.77 \rvert \pm 0.60$	
1676	RRc	0.39705458	64.28 ± 0.16	
1681	RRab	0.60655408	-21.70 ± 0.69	
1689	RRc	0.36822413	4.353 ± 0.11	
1697	RRab	0.42390450	-11.47 ± 0.66	
1698	RRab	0.58073446	$\lvert 8.60 \rvert \pm 0.40$	
1700	RRab	0.51282283	$\lvert 11.45 \rvert \pm 0.30$	

OGLE ID #	**Type**	**LSP P [d]**	**LSP $\dot{P}$ [$\times 10^{-9}$ d/d]**	**O–C $\dot{P}$ [$\times 10^{-9}$ d/d]**
1711	RRc	0.34732791	$\|2.52\| \pm 0.16$	
1735	RRab	0.61899042	-24.79 ± 0.67	
1759	RRab	0.67943363	16.9 ± 1.2	
1769	RRab	0.55929261	-6.645 ± 0.084	
1770	RRab	0.59271245	17.12 ± 0.56	
1809	RRab	0.56048108	-1.05 ± 0.13	
1817	RRab	0.53454945	-9.82 ± 0.24	
1822	RRab	0.57389797	2.552 ± 0.061	
1847	RRab	0.62101965	32.61 ± 0.40	
1867	RRab	0.45383899	-2.54 ± 0.13	
1883	RRab	0.56815146	$-2.71pm0.13$	
1918	RRab	0.65835123	7.94 ± 0.36	
1922	RRab	0.59297137	$\|8.6\| \pm 1.5$	
1925	RRab	0.55794071	$\|25.8\| \pm 1.3$	
1942	RRab	0.61687152	-7.19 ± 0.38	
1947	RRab	0.59380198	$\|32.8\| \pm 1.8$	
1953	RRab	0.61248614	$\|55.8\| \pm 2.7$	
1964	RRab	0.62937641	$\|11.97\| \pm 0.64$	
1974	RRab	0.60101082	$\|29.7\| \pm 1.0$	
1982	RRab	0.52159724	-19.8 ± 0.67	
1993	RRab	0.57830918	11.7 ± 0.14	
2021	RRab	0.63500369	$\|99.0\| \pm 3.3$	
2031	RRab	0.60736456	$\|22.1\| \pm 1.5$	
2049	RRab	0.58953998	$\|92.0\| \pm 2.0$	
2056	RRab	0.55952927	38.3 ± 1.4	
2073	RRc	0.41004964	-34.84 ± 0.89	
2076	RRab	0.59147134	$\|45.0\| \pm 1.3$	
2084	RRab	0.57470975	10.33 ± 0.026	
2128	RRab	0.57973187	-18.77 ± 0.41	
2129	RRab	0.60429533	$\|20.8\| \pm 1.6$	
2146	RRab	0.60954233	$\|85.1\| \pm 3.1$	
2159	RRab	0.66034337	9.12 ± 0.79	
2169	RRab	0.70741222	9.9 ± 1.1	
2175	RRab	0.59032147	65.9 ± 1.5	
2191	RRab	0.55556741	-66.40 ± 0.31	
2204	RRab	0.65093941	-11.9 ± 1.1	
2252	RRab	0.60653267	$\|21.7\| \pm 3.1$	
2254	RRab	0.58753248	$\|13.8\| \pm 1.7$	
2286	RRab	0.55014596		$\sim \|5.2\|$
2299	RRab	0.60075288	$\|100.0\| \pm 2.5$	
2303	RRab	0.62842727	$\|10.9\| \pm 2.2$	
2316	RRab	0.59575406	-7.23 ± 0.6	

OGLE ID #	**Type**	**LSP** P **[d]**	**LSP** $\dot{P}$ **[$\times 10^{-9}$ d/d]**	**O–C** $\dot{P}$ **[$\times 10^{-9}$ d/d]**
2318	RRab	0.51820013	$\|21.3\| \pm 1.9$	
2322	RRab	0.58975537	-7.5 ± 1.24	
2326	RRab	0.61754908	$\|15.2\| \pm 2.0$	
2346	RRab	0.74457741	-45.68 ± 0.43	
2363	RRc	0.41904472		$\sim \|300\|$
2368	RRc	0.38304836		$\sim \|16\|$
2424	RRab	0.59387000	-10.03 ± 0.37	
2433	RRab	0.64234141	-17.70 ± 0.39	
2438	RRc	0.38638785	$\|27.95\| \pm 0.77$	
2445	RRab	0.57840782	45.74 ± 0.87	
2458	RRab	0.59703236	-10.01 ± 0.57	
2459	RRab	0.65107418	-32.1 ± 3.1	
2471	RRc	0.41063241	11.20 ± 0.33	
27	BLHer	1.54172371	$\|78.8\| \pm 7.5$	

References

Alongi, M., Bertelli, G., Bressan, A., & Chiosi, C. 1991, A&A, 244, 95

Aparicio, A., Bertelli, G., Chiosi, C., & Garcia-Pelayo, J. M. 1990, A&A, 240, 262

Arnett, W. D., Bahcall, J. N., Kirshner, R. P., & Woosley, S. E. 1989, ARA&A, 27, 629

Asplund, M., Grevesse, N., Sauval, A. J., & Scott, P. 2009, ARA&A, 47, 481

Babu, P., & Stoica, P. 2010, Digital Signal Processing, 20, 359

Bailey, S. I. 1902, Annals of Harvard College Observatory, 38, 1

Barning, F. J. M. 1963, Bulletin of the Astronomical Institutes of the Netherlands, 17, 22

Battich, T., Bertolami, M. M. M., Córsico, A. H., & Althaus, L. G. 2018, A&A, 614, A136

Beck, P. G., Bedding, T. R., Mosser, B., et al. 2011, Science, 332, 205

Bedding, T. R., Mosser, B., Huber, D., et al. 2011, Nat., 471, 608

Berdnikov, L. N. 1992, Soviet Astronomy Letters, 18, 207

Berdnikov, L. N., Pastukhova, E. N., Gorynya, N. A., Zharova, A. V., & Turner, D. G. 2007, PASP, 119, 82

Bethe, H. A., & Critchfield, C. L. 1938, Physical Review, 54, 248

Bildsten, L., Paxton, B., Moore, K., & Macias, P. J. 2012, ApJL, 744, L6

Blažko, S. 1907, Astronomische Nachrichten, 175, 325

Böhm-Vitense, E. 1958, Zeitschrift für Astrophysik, 46, 108

Bono, G., Caputo, F., Cassisi, S., Incerpi, R., & Marconi, M. 1997, ApJ, 483, 811

Bono, G., Caputo, F., & Di Criscienzo, M. 2007, A&A, 476, 779

Böttcher, M., & Dermer, C. D. 2010, ApJ, 711, 445

Boussinesq, J. 1903, Théorie analytique de la chaleur (Gauthier-Villars)

Bowers, R., & Deeming, T. 1984, Nat., 309, 477

Bressan, A., Bertelli, G., & Chiosi, C. 1986, Mem. Societa Astronomica Italiana, 57, 411

Bressan, A., Girardi, L., Marigo, P., Rosenfield, P., & Tang, J. 2015, in Astrophysics and Space Science Proceedings, Vol. 39, Asteroseismology of Stellar Populations in the Milky Way, ed. A. Miglio, P. Eggenberger, L. Girardi, & J. Montalbán, 25

Bressan, A., Marigo, P., Girardi, L., Nanni, A., & Rubele, S. 2013, in European Physical Journal Web of Conferences, Vol. 43, European Physical Journal Web of Conferences, 3001

Bressan, A., Marigo, P., Girardi, L., et al. 2012, MNRAS, 427, 127

Bressan, A. G., Chiosi, C., & Bertelli, G. 1981, A&A, 102, 25

Bretthorst, G. L. 1988, Bayesian spectrum analysis and parameter estimation, Lecture notes in statistics (Springer-Verlag)

Bretthorst, G. L. 2001, in American Institute of Physics Conference Series, Vol. 568, Bayesian Inference and Maximum Entropy Methods in Science and Engineering, ed. A. Mohammad-Djafari, 241–245

Broersen, P. M., de Waele, S., & Bos, R. 2000, in 10th International Symposium on Application of Laser Techniques to Fluid Mechanics, Lisbon

Brown, T. M., & Gilliland, R. L. 1994, ARA&A, 32, 37

Brown, T. M., Sweigart, A. V., Lanz, T., Landsman, W. B., & Hubeny, I. 2001, ApJ, 562, 368

Brown, T. M., Tumlinson, J., Geha, M., et al. 2014, ApJ, 796, 91

Caffau, E., Ludwig, H.-G., Steffen, M., Freytag, B., & Bonifacio, P. 2011, Sol. Phys., 268, 255

Carrera, R., Gallart, C., Hardy, E., Aparicio, A., & Zinn, R. 2008, AJ, 135, 836

Cassisi, S., Marín-Franch, A., Salaris, M., et al. 2011, A&A, 527, A59

Cassisi, S., Salaris, M., & Irwin, A. W. 2003, ApJ, 588, 862

Castellani, V., Giannone, P., & Renzini, A. 1971, Astrophys. and Space Sci., 10, 340

Catelan, M. 2009, Astrophys. and Space Sci., 320, 261

Catelan, M. 2013, in European Physical Journal Web of Conferences, Vol. 43, European Physical Journal Web of Conferences, 01001

Catelan, M., & Smith, H. A. 2015, Pulsating Stars (Wiley-VCH)

Chabrier, G. 2001, ApJ, 554, 1274

—. 2003, PASP, 115, 763

Chadid, M., Wade, G. A., Shorlin, S. L. S., & Landstreet, J. D. 2004, A&A, 413, 1087

Chen, B.-Q., Jiang, B.-W., & Yang, M. 2013, Research in Astronomy and Astrophysics, 13, 290

Chen, Y., Bressan, A., Girardi, L., et al. 2015, MNRAS, 452, 1068

Choi, J., Dotter, A., Conroy, C., et al. 2016, ApJ, 823, 102

Choudhury, S., Subramaniam, A., Cole, A. A., & Sohn, Y.-J. 2018, MNRAS, 475, 4279

Christensen-Dalsgaard, J. 2004, Sol. Phys., 220, 137

Christensen-Dalsgaard, J., Monteiro, M. J. P. F. G., Rempel, M., & Thompson, M. J. 2011, MNRAS, 414, 1158

Clayton, D. D. 1968, Principles of stellar evolution and nucleosynthesis (McGraw-Hill)

Clement, C. M., & Shelton, I. 1997, AJ, 113, 1711

Clement, C. M., Muzzin, A., Dufton, Q., et al. 2001, AJ, 122, 2587

Cole, A. A., Grocholski, A. J., Geisler, D., et al. 2009, in IAU Symposium, Vol. 256, The Magellanic System: Stars, Gas, and Galaxies, ed. J. T. Van Loon & J. M. Oliveira, 263–268

Cole, A. A., Tolstoy, E., Gallagher, III, J. S., & Smecker-Hane, T. A. 2005, AJ, 129, 1465

Cole, A. A., Weisz, D. R., Dolphin, A. E., et al. 2014, ApJ, 795, 54

Cox, J. P. 1955, ApJ, 122, 286

—. 1963, ApJ, 138, 487

Cox, J. P., Cox, A. N., Olsen, K. H., King, D. S., & Eilers, D. D. 1966, ApJ, 144, 1038

Cox, J. P., & Giuli, R. T. 1968, Principles of stellar structure (Gordon and Breach)

Cumming, A., Marcy, G. W., & Butler, R. P. 1999, ApJ, 526, 890

Cyburt, R. H., Amthor, A. M., Ferguson, R., et al. 2010, ApJS, 189, 240

Da Costa, G. S., & Armandroff, T. E. 1990, AJ, 100, 162

de Jong, R. S., Bellido-Tirado, O., Chiappini, C., et al. 2012, in Proceedings of the SPIE, Vol. 8446, Ground-based and Airborne Instrumentation for Astronomy IV, 84460T

De Ridder, J., Barban, C., Baudin, F., et al. 2009, Nat., 459, 398

De Silva, G. M., Freeman, K. C., Bland-Hawthorn, J., et al. 2015, MNRAS, 449, 2604

Dearborn, D. S. P., Lattanzio, J. C., & Eggleton, P. P. 2006, ApJ, 639, 405

Demarque, P., & Mengel, J. G. 1971, ApJ, 164, 317

Derekas, A., Kiss, L. L., Udalski, A., Bedding, T. R., & Szatmáry, K. 2004, MNRAS, 354, 821

Despain, K. H. 1981, ApJ, 251, 639

Deupree, R. G. 1996, ApJ, 471, 377

Di Cecco, A., Bono, G., Stetson, P. B., et al. 2010, ApJ, 712, 527

Dobbie, P. D., Cole, A. A., Subramaniam, A., & Keller, S. 2014, MNRAS, 442, 1680

Dolphin, A. E. 2016, ApJ, 825, 153

Dorman, B., Rood, R. T., & O'Connell, R. W. 1993, ApJ, 419, 596

Dotter, A. 2016, ApJS, 222, 8

Dziembowski, W. A., Gough, D. O., Houdek, G., & Sienkiewicz, R. 2001, MNRAS, 328, 601

Edelson, R. A., & Krolik, J. H. 1988, ApJ, 333, 646

Erickson, M., Engle, S., Guinan, E., & Wells, M. 2018, in American Astronomical Society Meeting Abstracts, Vol. 231, American Astronomical Society Meeting Abstracts #231, 146.15

Fan, J.-H., Liu, Y., Qian, B.-C., et al. 2010, Research in Astronomy and Astrophysics, 10, 1100

Ferguson, J. W., Alexander, D. R., Allard, F., et al. 2005, ApJ, 623, 585

Ferraz-Mello, S. 1981, AJ, 86, 619

Fowler, W. A. 1986, The Synthesis of the Chemical Elements Carbon and Oxygen

Gallart, C., Zoccali, M., & Aparicio, A. 2005, ARA&A, 43, 387

Gautschy, A., & Saio, H. 1996, ARA&A, 34, 551

Gavrilchenko, T., Klein, C. R., Bloom, J. S., & Richards, J. W. 2014, MNRAS, 441, 715

Gilliland, R. L., & Baliunas, S. L. 1987, ApJ, 314, 766

Gingold, R. A., & Faulkner, D. J. 1974, ApJ, 188, 145

Graczyk, D., Pietrzyński, G., Thompson, I. B., et al. 2014, ApJ, 780, 59

Graham, M. J., Drake, A. J., Djorgovski, S. G., et al. 2013, MNRAS, 434, 3423

Gray, D. F. 2005, The Observation and Analysis of Stellar Photospheres 3rd Edition (Cambridge University Press)

Gregory, P. C. 2001, in American Institute of Physics Conference Series, Vol. 568, Bayesian Inference and Maximum Entropy Methods in Science and Engineering, ed. A. Mohammad-Djafari, 557–568

Hansen, C. J., Kawaler, S. D., & Trimble, V. 2004, Stellar interiors : physical principles, structure, and evolution, 2nd edn.

Harteveld, W. K., Mudde, R. F., & Van den Akker, H. E. A. 2005, Chemical Engineering Science, 60, 6160 , 7th International Conference on Gas-Liquid and Gas-Liquid-Solid Reactor Engineering

Hayashi, C., Hōshi, R., & Sugimoto, D. 1962, Progress of Theoretical Physics Supplement, 22, 1

Heber, U. 2016, PASP, 128, 082001

Hekker, S. 2010, Astronomische Nachrichten, 331, 1004

Hekker, S., Gilliland, R. L., Elsworth, Y., et al. 2011, MNRAS, 414, 2594

Herwig, F. 2000, A&A, 360, 952

Ho, N., Geha, M., Tollerud, E. J., et al. 2015, ApJ, 798, 77

Hoyle, F., & Schwarzschild, M. 1955, ApJS, 2, 1

Hoyt, T. J., Freedman, W. L., Madore, B. F., et al. 2018, ApJ, 858, 12

Huber, D., Bedding, T. R., Stello, D., et al. 2010, ApJ, 723, 1607

Iglesias, C. A., & Rogers, F. J. 1996, ApJ, 464, 943

Irwin, A. W., Campbell, B., Morbey, C. L., Walker, G. A. H., & Yang, S. 1989, PASP, 101, 147

Jaynes, E., & Bretthorst, G. 2003, Probability Theory: The Logic of Science (Cambridge University Press)

Jaynes, E. T. 1987, in Maximum-Entropy and Bayesian Spectral Analysis and Estimation Problems, ed. C. R. Smith & G. J. Erickson (Springer Netherlands), 1–37

Jurcsik, J., & Kovacs, G. 1996, A&A, 312, 111

Kalirai, J. S., Bergeron, P., Hansen, B. M. S., et al. 2007, ApJ, 671, 748

Kalirai, J. S., Saul Davis, D., Richer, H. B., et al. 2009, ApJ, 705, 408

Kippenhahn, R., Weigert, A., & Weiss, A. 2012, Stellar Structure and Evolution (Springer-Verlag)

Kirby, E. N., Cohen, J. G., Guhathakurta, P., et al. 2013, ApJ, 779, 102

Kirby, E. N., Cohen, J. G., Smith, G. H., et al. 2011a, ApJ

Kirby, E. N., Lanfranchi, G. A., Simon, J. D., Cohen, J. G., & Guhathakurta, P. 2011b, ApJ

Kirby, E. N., Martin, C. L., & Finlator, K. 2011c, ApJL

Kirby, E. N., Rizzi, L., Held, E. V., et al. 2017, ApJ, 834, 9

Kiss, L. L., & Bedding, T. R. 2003, MNRAS, 343, L79

Koopmann, R. A., Lee, Y.-W., Demarque, P., & Howard, J. M. 1994, ApJ, 423, 380

Kovács, G. 1998, in Astronomical Society of the Pacific Conference Series, Vol. 135, A Half Century of Stellar Pulsation Interpretation, ed. P. A. Bradley & J. A. Guzik, 52

Kovács, G. 2005, A&A, 438, 227

Kroupa, P. 2001, MNRAS, 322, 231

Kroupa, P., Tout, C. A., & Gilmore, G. 1993, MNRAS, 262, 545

Kunder, A., & Chaboyer, B. 2009, AJ, 138, 1284

Kunder, A., Walker, A., Stetson, P. B., et al. 2011, AJ, 141, 15

Lee, Y.-W. 1991, ApJ, 367, 524

Lomb, N. R. 1976, Astrophys. and Space Sci., 39, 447

Luo, A.-L., Zhao, Y.-H., Zhao, G., et al. 2015, Research in Astronomy and Astrophysics, 15, 1095

Manning, E. M., & Cole, A. A. 2017, MNRAS, 471, 4194

Marigo, P., & Aringer, B. 2009, A&A, 508, 1539

Marigo, P., Bressan, A., Nanni, A., Girardi, L., & Pumo, M. L. 2013, MNRAS, 434, 488

Marigo, P., Girardi, L., Bressan, A., et al. 2017, ApJ, 835, 77

Matsunaga, N., Feast, M. W., & Soszyński, I. 2011, MNRAS, 413, 223

Mayo, W. T. 1978, in Proceedings of the Dynamic Flow Conference 1978 on Dynamic Measurements in Unsteady Flows, ed. B. W. Hansen (Springer Netherlands), 851–868

McQuinn, K. B. W., Skillman, E. D., Dalcanton, J. J., et al. 2011, ApJ, 740, 48

Mestel, L. 1952, MNRAS, 112, 583

Meynet, G., Maeder, A., Schaller, G., Schaerer, D., & Charbonnel, C. 1994, A&AS, 103, 97

Michail, M., Engle, S. G., & Guinan, E. F. 2018, Research Notes of the AAS, 2, 117

Miller Bertolami, M. M., Córsico, A. H., & Althaus, L. G. 2011, ApJL, 741, L3

Miller Bertolami, M. M., Córsico, A. H., Zhang, X., Althaus, L. G., & Jeffery, C. S. 2013, in European Physical Journal Web of Conferences, Vol. 43, European Physical Journal Web of Conferences, 04004

Mocák, M., Campbell, S. W., Müller, E., & Kifonidis, K. 2010, A&A, 520, A114

Mocák, M., Müller, E., Weiss, A., & Kifonidis, K. 2008, A&A, 490, 265

—. 2009, A&A, 501, 659

Montalbán, J., Kupka, F., D'Antona, F., & Schmidt, W. 2001, A&A, 370, 982

Morgan, S. M., Wahl, J. N., & Wieckhorst, R. M. 2007, MNRAS, 374, 1421

Mosser, B., Barban, C., Montalbán, J., et al. 2011, A&A, 532, A86

Mudelsee, M. 2013, Climate Time Series Analysis: Classical Statistical and Bootstrap Methods (Springer, Cham)

Naslim, N., Jeffery, C. S., Ahmad, A., Behara, N. T., & Şahìn, T. 2010, MNRAS, 409, 582

Nieppola, E., Hovatta, T., Tornikoski, M., et al. 2009, AJ, 137, 5022

Park, J.-H., & Lee, Y.-W. 1997, ApJ, 476, 28

Pasetto, S., Chiosi, C., Cropper, M., & Grebel, E. K. 2014, MNRAS, 445, 3592

Paxton, B., Bildsten, L., Dotter, A., et al. 2011, ApJS, 192, 3

Paxton, B., Cantiello, M., Arras, P., et al. 2013, ApJS, 208, 4

Paxton, B., Marchant, P., Schwab, J., et al. 2015, ApJS, 220, 15

Peimbert, M., Sarmiento, A., & Colín, P. 1994, Revista Mexicana de Astronomia y Astrofisica, 28, 181

Percy, J. R., & Hale, J. 1998, PASP, 110, 1428

Percy, J. R., & Hoss, J. X. 2000, Journal of the American Association of Variable Star Observers (JAAVSO), 29, 14

Pietrzyński, G., Thompson, I. B., Gieren, W., et al. 2012, Nat., 484, 75

Piotto, G., Bedin, L. R., Anderson, J., et al. 2007, ApJL, 661, L53

Poleski, R. 2008, Acta Astron., 58, 313

Press, W. H., Teukolsky, S. A., Vetterling, W. T., & Flannery, B. P. 2007, Numerical Recipes 3rd Edition: The Art of Scientific Computing (Cambridge University Press)

Rabidoux, K., Smith, H. A., Pritzl, B. J., et al. 2010, AJ, 139, 2300

Randall, S. K., Bagnulo, S., Ziegerer, E., Geier, S., & Fontaine, G. 2015, A&A, 576, A65

Reimers, D. 1975, Memoires of the Societe Royale des Sciences de Liege, 8, 369

Reitzel, D. B., & Guhathakurta, P. 2002, AJ, 124, 234

Renzini, A. 1984, in IAU Symposium, Vol. 105, Observational Tests of the Stellar Evolution Theory, ed. A. Maeder & A. Renzini, 21

Renzini, A., & Buzzoni, A. 1986, in Astrophysics and Space Science Library, Vol. 122, Spectral Evolution of Galaxies, ed. C. Chiosi & A. Renzini, 195–231

Renzini, A., Greggio, L., Ritossa, C., & Ferrario, L. 1992, ApJ, 400, 280

Richer, J., Michaud, G., & Turcotte, S. 2000, ApJ, 529, 338

Ritossa, C. 1996, MNRAS, 281, 970

Ritter, A. 1879, Annalen der Physik und Chemie

Roberts, D. H., Lehar, J., & Dreher, J. W. 1987, AJ, 93, 968

Rood, R. T. 1973, ApJ, 184, 815

Rosenfield, P., Marigo, P., Girardi, L., et al. 2016, ApJ, 822, 73

Ross, T. L., Holtzman, J., Saha, A., & Anthony-Twarog, B. J. 2015, AJ, 149, 198

Rosseland, S. 1949, The pulsation theory of variable stars.

Salaris, M., & Cassisi, S. 2005, Evolution of Stars and Stellar Populations (Wiley-VCH.)

Salaris, M., Cassisi, S., & Weiss, A. 2002, PASP, 114, 375

Salpeter, E. E. 1955, ApJ, 121, 161

Sandage, A. 2004, AJ, 128, 858

Sandage, A. R., & Schwarzschild, M. 1952, ApJ, 116, 463

Scargle, J. D. 1982, ApJ, 263, 835

—. 1989, ApJ, 343, 874

Schimmel, M. 2001, Biological Rhythm Research, 32, 341

Schulz, M., & Stattegger, K. 1997, Computers & Geosciences, 23, 929

Schuster, A. 1898, Terrestrial Magnetism, 3, 13

Schwarzschild, K. 1906, Nachrichten von der Königlichen Gesellschaft der Wissenschaften zu Göttingen. Math.-phys. Klasse, 195, 41

Schwarzschild, M., & Härm, R. 1962, ApJ, 136, 158

—. 1965, ApJ, 142, 855

—. 1970, ApJ, 160, 341

Serenelli, A., & Weiss, A. 2005, A&A, 442, 1041

Serenelli, A., Weiss, A., Cassisi, S., Salaris, M., & Pietrinferni, A. 2017, A&A, 606, A33

Shen, K. J., & Bildsten, L. 2009, ApJ, 699, 1365

Silva Aguirre, V., Catelan, M., Weiss, A., & Valcarce, A. A. R. 2008, A&A, 489, 1201

—. 2010, Astrophys. and Space Sci., 328, 123

Simon, N. R., & Lee, A. S. 1981, ApJ, 248, 291

Sirorattanakul, K., Engle, S., Pepper, J., et al. 2017, AJ, 154, 217

Smith, H. A. 1995, Science, 270, 1236

—. 2013, ArXiv e-prints, arXiv:1310.0533

Smith, H. A., Catelan, M., & Kuehn, C. 2011, in RR Lyrae Stars, Metal-Poor Stars, and the Galaxy, ed. A. McWilliam, Vol. 5, 17

Soszyński, I., Udalski, A., Szymański, M. K., et al. 2010a, Acta Astron., 60, 165

—. 2010b, Acta Astron., 60, 91

—. 2008, Acta Astron., 58, 293

—. 2009, Acta Astron., 59, 1

Soszyński, I., Dziembowski, W. A., Udalski, A., et al. 2011a, Acta Astron., 61, 1

Soszyński, I., Udalski, A., Szymański, M. K., et al. 2011b, Acta Astron., 61, 217

Soszyński, I., Udalski, A., Pietrukowicz, P., et al. 2013, Acta Astron., 63, 37

Soszyński, I., Udalski, A., Szymański, M. K., et al. 2016, Acta Astron., 66, 131

Stellingwerf, R. F. 1978, ApJ, 224, 953

Stoica, P., Li, J., & He, H. 2009, IEEE Transactions on Signal Processing, 57, 843

Stothers, R. B. 2006, ApJ, 652, 643

Sugimoto, D., & Fujimoto, M. Y. 2000, ApJ, 538, 837

Suntzeff, N. B., Mateo, M., Terndrup, D. M., et al. 1993, ApJ, 418, 208

Sweigart, A. V. 1994, ApJ, 426, 612

Sweigart, A. V., & Gross, P. G. 1978, ApJS, 36, 405

Sweigart, A. V., & Renzini, A. 1979, A&A, 71, 66

Swingler, D. N. 1989, AJ, 97, 280

Tang, J., Bressan, A., Rosenfield, P., et al. 2014, MNRAS, 445, 4287

Tegmark, M. 1997, ApJL, 480, L87

Templeton, M. R., & Henden, A. A. 2007, AJ, 134, 1999

Thomas, H.-C. 1967, Zeitschrift für Astrophysik, 67, 420

Thomson, J.-J. 1906, Conduction of Electricity through Gases (Cambridge Univ. Press)

Tinsley, B. M. 1976, ApJ, 208, 797

—. 1980, Fundamentals of Cosmic Physics, 5, 287

Tolstoy, E., Venn, K. A., Shetrone, M., et al. 2003, AJ, 125, 707

Tolstoy, E., Irwin, M. J., Helmi, A., et al. 2004, ApJL, 617, L119

Trager, S. C., Worthey, G., Faber, S. M., & Dressler, A. 2005, MNRAS, 362, 2

Turcotte, S., Richer, J., Michaud, G., Iglesias, C. A., & Rogers, F. J. 1998, ApJ, 504, 539

Turner, D. G. 1998, Journal of the American Association of Variable Star Observers (JAAVSO), 26, 101

Udalski, A., Szymanski, M. K., Soszynski, I., & Poleski, R. 2008a, Acta Astron., 58, 69

—. 2008b, Acta Astron., 58, 69

Uttenthaler, S., Greimel, R., & Templeton, M. 2016, Astronomische Nachrichten, 337, 293

van den Bergh, S. 1962, AJ, 67, 486

Van der Swaelmen, M., Hill, V., Primas, F., & Cole, A. A. 2013, A&A, 560, A44

Van Der Walt, S., Colbert, S. C., & Varoquaux, G. 2011, ArXiv e-prints, arXiv:1102.1523

VandenBerg, D. A., Bergbusch, P. A., Dotter, A., et al. 2012, ApJ, 755, 15

VanderPlas, J. 2016, gatspy: General tools for Astronomical Time Series in Python, Astrophysics Source Code Library, ascl:1610.007

VanderPlas, J., Connolly, A., Ivezic, Z., & Gray, A. 2012, in Proceedings of the Conference on Intelligent Data Understanding, Proceedings of the Conference on Intelligent Data Understanding, 47–54

VanderPlas, J. T. 2018, The Astrophysical Journal Supplement Series, 236, 16

VanderPlas, J. T., & Ivezić, Ž. 2015, ApJ, 812, 18

Vassiliadis, E., & Wood, P. R. 1993, ApJ, 413, 641

Weiss, A., & Schlattl, H. 2008, Astrophys. and Space Sci., 316, 99

Woosley, S. E., Pinto, P. A., & Ensman, L. 1988, ApJ, 324, 466

Worthey, G. 1994, ApJS, 95, 107

Zechmeister, M., & Kürster, M. 2009, A&A, 496, 577

Zhang, B.-K., Dai, B.-Z., Zhang, L., & Cao, Z. 2010, Research in Astronomy and Astrophysics, 10, 653